SIGNAL PROCESSING AND BEAMFORMING TECHNIQUES FOR CELL FREE MM-WAVE MASSIVE MIMO SYSTEMS

A THESIS SUBMITTED TO
THE GRADUATE SCHOOL OF NATURAL AND APPLIED SCIENCES
OF
MIDDLE EAST TECHNICAL UNIVERSITY

BY

METEHAN KARATAŞ

IN PARTIAL FULFILLMENT OF THE REQUIREMENTS
FOR
THE DEGREE OF MASTER OF SCIENCE
IN
ELECTRICAL AND ELECTRONICS ENGINEERING

JUNE 2023

Approval of the thesis:

SIGNAL PROCESSING AND BEAMFORMING TECHNIQUES FOR CELL FREE MM-WAVE MASSIVE MIMO SYSTEMS

submitted by **METEHAN KARATAŞ** in partial fulfillment of the requirements for the degree of **Master of Science in Electrical and Electronics Engineering Department, Middle East Technical University** by,

Prof. Dr. Halil Kalıpçılar
Dean, Graduate School of **Natural and Applied Sciences** _____

Prof. Dr. İlkay Ulusoy
Head of Department, **Electrical and Electronics Engineering** _____

Assist. Prof. Dr. Gökhan Güvensen
Supervisor, **Electrical and Electronics Engineering, METU** _____

Examining Committee Members:

Prof. Dr. Ali Özgür Yılmaz
Electrical and Electronics Engineering, METU _____

Assist. Prof. Dr. Gökhan Muzaffer Güvensen
Electrical and Electronics Engineering, METU _____

Prof. Dr. Cenk Toker
Electrical and Electronics Engineering, Hacettepe University _____

Assoc. Prof. Dr. Ayşe Melda Yüksel Turgut
Electrical and Electronics Engineering, METU _____

Assist. Prof. Dr. Özlem Tuğfe Demir
Electrical and Electronics Engineering, TOBB ETU _____

Date:20.06.2023

I hereby declare that all information in this document has been obtained and presented in accordance with academic rules and ethical conduct. I also declare that, as required by these rules and conduct, I have fully cited and referenced all material and results that are not original to this work.

Name, Surname: Metehan Karataş

Signature :

ABSTRACT

SIGNAL PROCESSING AND BEAMFORMING TECHNIQUES FOR CELL FREE MM-WAVE MASSIVE MIMO SYSTEMS

Karataş, Metehan
M.S., Department of Electrical and Electronics Engineering
Supervisor: Assist. Prof. Dr. Gökhan Güvensen

June 2023, 90 pages

This thesis presents a hybrid beamforming uplink receiver detector for massive MIMO (mMIMO) cell-free (CF) networks operating in millimeter-wave (mmWave) frequencies. CF networks aim to provide uniform service by jointly serving user equipments (UEs) through multiple access points (APs) connected to a central processing unit (CPU). However, serving all UEs with all APs is impractical and computationally complex. The user-centric (UC) variant was introduced to address this, where each UE is served by a subset of APs based on channel conditions. Additionally, the shift to mmWave frequencies offers increased network capacity by leveraging wider bandwidth and larger antenna arrays. Hybrid beamformers, consisting of analog and digital stages, were proposed to reduce the number of radio frequency (RF) chains. The proposed analog beamformer (AB) in this work is the modified eigen beamformer (MEB). MEB promotes a trend of fairness among served UEs compared to well-known eigen beamformer (EB). The digital stage introduces two detectors, namely the cell-free iterative detector (CFI-D) and the user-centric iterative subset detector (UCIS-D), both employing single carrier frequency domain equalization (SC-FDE) modulation. CFI-D is an unscalable CF implementation of the iterative block-

decision feedback equalization (IB-DFE) structure, while UCIS-D offers a scalable UC alternative. UCIS-D incorporates a parallel interference cancellation (PIC) stage before IB-DFE, selectively processing interferers based on their relative strength. The weakest interferers are ignored, while the strongest are processed by IB-DFE, considering residual interference from PIC. Both detectors utilize soft decisions and employ frequency domain decision feedback (FDDF). The performance of these detectors is evaluated using the achievable information rate (AIR) and bit-error-rate (BER). Simulation results demonstrate the proposed receiver's ability to handle ultra-high loads in terms of BER and AIR.

Keywords: cell-free, user-centric, hybrid-beamformer, mmWave, massive MIMO

ÖZ

HÜCRESEL OLMAYAN MİLİMETRİK DALGA MASİF MIMO SİSTEMLER İÇİN SİNYAL İŞLEME VE HÜZMELEME

Karataş, Metehan
Yüksek Lisans, Elektrik ve Elektronik Mühendisliği Bölümü
Tez Yöneticisi: Dr. Öğr. Üyesi. Gökhan Güvensen

Haziran 2023 , 90 sayfa

Bu tez, milimetre dalga (mmWave) frekanslarında çalışan masif MIMO (mMIMO) hücresiz (CF) ağlar için hibrit hüzmeleme yukarı bağlantı alıcı dedektörü sunmaktadır. CF ağları, bir merkezi işlem birimine (CPU) bağlı çoklu erişim noktaları (AP'ler) aracılığıyla kullanıcı ekipmanlarına (UE'ler) ortaklaşa hizmet vererek homojen bir hizmet kalitesi sağlamayı amaçlar. Ancak, tüm UE'lere tüm AP'lerle hizmet vermek pratik değildir ve hesaplama açısından karmaşıktır. CF ağların, bu sorunlarını çözmek için, her UE'ye kanal koşullarına bağlı olarak AP'lerin bir alt kümesi tarafından hizmet verildiği kullanıcı odaklı (UC) varyantları geliştirilmiştir. Ek olarak, mmWave frekanslarına geçiş, daha geniş bant genişliği ve daha büyük anten dizilerinden yararlanarak daha fazla ağ kapasitesi sunar. Radyo frekansı (RF) zincirlerinin sayısını azaltmak için ise analog ve sayısal aşamalardan oluşan hibrit hüzmeleme teknikleri önerilmiştir. Bu çalışmada önerilen analog hüzmeleme (AB) metodu, modifiye öz hüzmeleme (MEB) metodudur. MEB, iyi bilinen öz hüzmeleme (EB) metoduna kıyasla hizmet verilen UE'ler arasında bir eşitlik eğilimini teşvik eder. Sayısal aşama, her ikisi de tek taşıyıcı frekans alanı eşitleme (SC-FDE) modülasyonu kullanan hüc-

resiz yinelemeli dedektör (CFI-D) ve kullanıcı odaklı yinelemeli altküme dedektörü (UCIS-D) olmak üzere iki dedektör sunar. CFI-D, yinelemeli blok karar geri besleme eşitleme (IB-DFE) yapısının ölçeklenemez bir CF uygulamasıdır, UCIS-D ise ölçeklenebilir bir UC alternatifi sunar. UCIS-D, IB-DFE'den önce bir paralel girişim sönümleme (PIC) aşaması içerir ve girişim kaynaklarını göreceli güçlerine göre gruplayarak işler. En zayıf girişim kaynakları göz ardı edilirken en güçlüleri, PIC'den kalan girişim dikkate alınarak IB-DFE tarafından işlenir. Her iki detektör de yumuşak kararlar kullanır ve frekans alanı karar geri bildirimi (FDDF) kullanır. Bu dedektörlerin performansı, ulaşılabilir bilgi oranı (AIR) ve bit hata oranı (BER) kullanılarak değerlendirilir. Simülasyon sonuçları, önerilen alıcının BER ve AIR açısından ultra yüksek yükleri kaldırabilme becerisini göstermektedir.

Anahtar Kelimeler: hücresiz ağ, kullanıcı odaklı, hibrit hüzmeleme, milimetre dalga, masif MIMO

to my beloved family

ACKNOWLEDGMENTS

First, I would like to express my greatest appreciation to my supervisor Dr. Gökhan Muzaffer Güvensen. He has been a great mentor, a friend and everything in between as I needed through my higher education.

Next I would like to thank TÜRK TELEKOM, for all their support within the framework of 5G and Beyond Joint Graduate Support Program coordinated by Information and Communication Technologies Authority. Within TÜRK TELEKOM, I would like to thank my manager Selami Çiftçi specifically, who has been very understanding and supportive during my time in TÜRK TELEKOM.

As a personal note, I want to thank to my close friends Osman Furkan Kar, Anıl Başol, Gökhan Çağlayan Karaova, Burak Aslanmirza, Özge Mete Aslanmirza, Deniz Atılgan, Taha Bayaz, Serhan Karadeniz and especially my sister Sena Karataş. Their support and encouragement have been immensely invaluable.

I would also like to give my biggest thanks to my parents. Their care and support is what made it possible for me to move forward and achieve anything in my life.

Finally, I would like to thank to Asya Bülbül. I am very grateful for her boundless understanding, care and support.

TABLE OF CONTENTS

LIST OF TABLES

TABLES

LIST OF FIGURES

FIGURES

LIST OF ABBREVIATIONS

AB	Analog Beamformer
ADC	Analog to Digital Conversion
AIR	Achievable Information Rate
AoA	Angle of Arrival
AP	Access Point
ASD	Angular Standard Deviation
BER	Bir Error Rate
CCM	Channel Covariance Matrix
CCP	Computational Complexity
CDF	Cumulative Distribution Function
CF	Cell-Free
CFI-D	Cell-Free Iterative Detector
CM	Covariance Matrix
CPU	Central Processing Unit
CSI	Channel State Information
DFT	Discrete Fourier Transform
DRL	Deep Reinforcement Learning
EB	Eigen Beamformer
ECM	Error Correction Mechanism
ETD	Effective Time Domain
FDDF	Frequency Domain Decision Feedback
GEB	Generalized Eigen Beamformer
IB-DFE	Iterative Block-Decision Feedback Equalization
MA	Multiply and Accumulate

MEB	Modified Eigen Beamformer
MF	Matched Filter
mMIMO	Massive Multiple Input Multiple Output
MMSE	Minimum-Mean-Squared-Error
mmWave	Millimeter Wave
MPC	Multipath-Component
MRC	Maximum Ratio Combiner
MSE	Mean-Squared-Error
NW	Network Wide
NW-MMSE	Network Wide-Minimum Mean Squared Error
OFDM	Orthogonal Frequency Division Multiplexing
PIC	Parallel Interference Cancellation
RF	Radio Frequency
SC-FDE	Single Carrier Frequency Domain Equalization
SE	Spectral Efficiency
SER	Symbol Error Rate
SIC	Successive Interference Cancellation
SINR	Signal to Interference Plus Noise Ratio
UC	User Centric
UCIS-D	User-Centric Iterative Subset Detector
UE	User Equipment
ULA	Uniform Linear Array
ZF	Zero-Forcing
ZMCSCG	Zero-Mean Circulant Symmetric Complex Gaussian

CHAPTER 1

INTRODUCTION

1.1 Motivation and Problem Definition

The demand for higher capacity within wireless networks is everlasting. The number of network users constantly increases over time, and the data rates users need increase along with it. To this end, network densification ensued [1], leading to greater inter-cell interference. To combat this issue, the method of cell-free (CF) massive multiple input multiple output (mMIMO) networks, where there are no cell boundaries, got popular [2]. In conventional cellular networks, the access points (APs) are assigned to predetermined areas. Every user equipment (UE) in an area is served only by the AP assigned to that area. In CF mMIMO networks, all the access points (APs) are connected to a central processing unit (CPU), providing service jointly to all UEs. It has been shown that in terms of uniformity of service and inter-cell interference, CF mMIMO networks offer a considerable improvement over conventional cellular networks [3]. Actually, similar concepts to CF networks were proposed under the names of cloud radio access networks and coordinated multi-point networks [4]. Some related literature uses these names, such as [22] and [40]. However, the specifications can change from source to source, leading to no definitive boundary between different names [4].

There are two implementation methods for the CF mMIMO networks. The first one is centralized implementation, where APs only act as relays. They forward their received signals directly (or only the digital baseband signal) to the CPU , and analog-to-digital (ADC) conversion and all the baseband processing is done in the CPU. The second is the distributed implementation, where each AP performs its own ADC

conversion and constructs a local estimate of the transmitted symbols by baseband operations. Then APs forward only these local estimates, and the CPU combines them for the final detection-decoding operations. There are advantages and disadvantages of both implementations [4]. This work focuses on centralized implementation.

CF mMIMO networks did indeed offer enhanced quality of service and uniformity of service [5]. However, the notion of all APs serving all UEs was not feasible in practice due to the computational complexity (CCP) required. To this end, a new user-centric (UC) approach (UC mMIMO) was introduced [6], [7]. In UC mMIMO networks, only a portion of APs (the ones with the best channels) would serve a given UE to reduce the CCP [8] and to decrease the fronthaul signaling load. Since in large networks, only a handful of APs have good channels to a given UE, and this approach offered good performance while being computationally feasible [4].

Changing the network structure was one of many methods to accommodate the higher capacity demand. Another method was to shift into the millimeter wave (mmWave) bands due to the abundance of available spectrum and the high congestion present in the sub-6 GHz frequencies [9]. Since the mmWave bands have short wavelength values compared to sub-6 GHz frequencies, a greater number of antenna elements can be fitted in mMIMO antenna arrays of the same size as an added benefit.

Earlier research on CF mMIMO focused on sub-6 GHz bands [5]. However, CF and UC mMIMO systems at mmWave frequencies got a lot of attention for the last several years [10], [11], and the research is still underway. Due to the large number of antennas present, practical analog/digital hybrid beamforming structures became a popular option for mmWave CF/UC mMIMO networks [12]- [15]. In hybrid beamformers, there is an analog radio frequency (RF) stage composed of phase shifters and attenuators (optional) before the ADC conversion. This stage reduces the dimension of the received/transmitted signal in the digital domain, allowing the system to operate with a lower number of RF chains.

Most current work on CF/UC mMIMO systems works with a narrowband single tap channel or an orthogonal frequency division multiplexing (OFDM) type modulation. In this work, single carrier frequency domain equalization (SC-FDE) is utilized. Many studies encourage the use of SC-FDE over OFDM in mmWave chan-

nels [16]- [18]. SC-FDE structures offer better performance in terms of quantization [19], peak-to-average power ratio [20], and robustness against carrier-frequency offset [20]. Since UEs generally have a lower computational capacity than APs, SC-FDE becomes a good alternative in the uplink.

This thesis introduces uplink receiver architectures for CF and UC mMIMO networks operating in mmWave frequencies. The receiver features a hybrid beamformer and employs SC-FDE modulation. Proposed methods are presented for the hybrid beamformer's analog and digital components. To apply the UC concept in practice, the notion of "Subset Grouping" is introduced. Subset Grouping has two stages. The first stage is choosing the set of APs that will serve a UE for every UE. The second stage is choosing the set of UEs whose channels will be estimated by an AP for every AP. Note that an AP will estimate the channel of a UE for one of two reasons. Either the AP will serve that UE, or it will use that UEs information for interference cancellation methods.

The analog beamformer (AB) section uses the slowly varying parameters of the system, namely the channel covariance matrices (CCMs) of the channels between UEs and APs. Every AP employs its own AB, and since only slowly changing parameters are used, the same AB can be used for many transmission blocks. There are such ABs popular in the literature, such as the eigen beamformer (EB) [12], and the Discrete Fourier Transform (DFT) beamformer [49]. The AB proposed by this work is a modified version of the EB called Modified Eigen Beamformer (MEB). MEB exploits the structure of the CCMs to illuminate the angles corresponding to the angle of arrival (AoA) of the signal paths coming from the served UEs. However, every UE is treated equally regardless of signal strength, promoting a trend of fairness. It is shown that this AB is suited for CF applications since the main attraction of the CF structures is to support a uniform service. The digital portion of the hybrid beamformer utilizes the iterative block decision feedback equalization (IB-DFE) method. The digital decoder, therefore, has an iterative and non-linear format working in the frequency domain. The IB-DFE method uses the soft decisions from the previous iteration to create a feedback path, aiming to minimize the mean-squared error (MSE) at every frequency bin at every iteration. First, a network-wide (NW) IB-DFE detector named "Cell-Free Iterative Detector (CFI-D)" is derived where every AP serves every UE.

Since an NW IB-DFE operation is computationally very costly, a novel digital detector is proposed as a UC alternative referred to as the "User-Centric Iterative Subset Detector". It is abbreviated as "UCIS-D". UCIS-D introduces a parallel interference cancellation (PIC) stage before the IB-DFE operation. Then, the residual interference from the PIC operation is considered in the following IB-DFE operation. The two proposed methods are then compared with each other along with the methods popular in the literature using the bit-error-rate (BER) and achievable information rate (AIR) metrics. AIR metric represents a lower bound on the mismatch decoding capacity, which is useful to measure the performance of the system under finite constellations.

1.2 Literature Review

The CF/UC mMIMO structure has gotten a lot of attention over the last several years. It has been studied extensively from different aspects for the sub-6 GHz bands [2]-[8], [22], [27] and [29]- [33]. The papers [2]- [5] show the advantages of CF mMIMO over small cells and the uniform service of CF structure, along with providing achievable rates with spectral efficiency. The scalability of a system refers to the computational cost increase per UE in the system when more UEs are introduced to the network. The papers [6] and [7] show that scalable UC implementations over CF implementations do not cause performance degradation SE-wise. UC implementations are even superior to CF implementations in some cases. In [8] and [4], the Subset MMSE method where the mentioned UE grouping and its MMSE implementation is explored. In [8], it is shown that, with the Subset MMSE method, a small portion of APs are enough to achieve the CF performance SINR-wise. In [4], the SE bounds for different combiners/precoders (such as MRC, partial ZF, MMSE, and subset MMSE) are derived for both centralized and distributed configurations.

In [22], a linear interference cancellation combiner is proposed to uplink UC mMIMO systems. Following a PIC operation, the combiner performs a matched filtering (MF) operation. The method is shown to be computationally less costly than Subset MMSE in [8] while achieving comparable SINR performance. In [27], a symbol error rate (SER) bound is derived, and near-optimal detectors are designed based on successive interference cancellation (SIC) and error correction mechanism (ECM) concepts for

the uplink of CF mMIMO systems. Also, an MF detector using ECM is proposed, which is less computationally complex than SIC-MMSE with higher SER. Power allocation and energy efficiency are explored in [28], [33]. Lastly, an uplink max-min SINR fairness-driven algorithm is given in [34]. The algorithm solves the receive filter (kind of a combiner) by solving a generalized eigenvalue problem, and user power allocation is solved with geometric programming. The algorithm alternates between the two solutions achieving a global optimum.

CF/UC mMIMO performance in mmWave frequencies is also a very popular topic for the last several years [11]- [15], [23], [25], [26] and [34]- [43]. When CF/UC mMIMO systems are explored in mmWave frequencies, a hybrid beamforming structure is almost always considered due to the impracticality of fully digital implementation.

In [11], a clustered channel model is expanded to include the correlation of closely located UEs and a simple 0-1 analog beamformer is used along with a partial ZF digital beamformer. Both UC and CF approaches are considered, and it is shown that the UC approach performs better due to allocating resources to more “efficient" APs.

In [12], CF mMIMO systems at mmWave frequencies are investigated under limited fronthaul constraints. A hybrid beamformer is used. The analog beamformer uses eigenvectors (quantized due to fronthaul constraints) of the CCMs, while the digital stage uses a ZF precoder.

In [13], two hybrid beamformers are compared, namely the decentralized (channel state information (CSI) of APs not available at the CPU) and the semi-centralized hybrid beamformers. It is shown that even with lower complexity and no CSI, the decentralized approach can achieve the performance of the semi-centralized one. Also, a novel adaptive RF chain selection algorithm is proposed for energy efficiency, and it is shown that the same performance of standard hybrid beamformers can be achieved without activating all the RF chains in the APs. In [14], an alternating minimization algorithm is used at each AP in a distributed operation, achieving an optimal analog combiner. The method uses a few fixed phase shifters aiming to maximize energy efficiency.

In [15], the weighted sum rate is maximized with a hybrid beamformer for a CF mMIMO downlink using a computationally efficient block coordinate descent algorithm while considering AP transmit power and constant modulus analog beamformer constraints.

In [23], a distributed CF mMIMO uplink is considered. A cyclic scheme is proposed where local hybrid beamformers produce an estimate, and the CPU combining these estimates is alternated to minimize MSE.

In [25], a two-stage uplink training structure is used for UE-AP association and hybrid beamformer design. The APs locally associate with UEs and implement their analog beamformers, while the CPU handles all the digital baseband processing. Digital stage and fronthaul compression is optimized according to the training results, the end goals being maximizing the weighted sum rate and max-min fairness.

The work in [26] introduces a method for power allocation in CF mMIMO mmWave networks, [36] proposes an interference-aware beam alignment algorithm for UEs with fully digital AP receivers. The work in [35] presents a hybrid beamformer where the analog stage only uses the angle of departure information, minimizing the MSE between transmit and receive signals using the Frobenius norm as a metric. The digital part is obtained with a standard linear MSE equalizer. The work in [37] presents a clustering-based pilot assignment for UC mMIMO mmWave networks.

There are similar works expanding on hybrid beamformer literature focused on CF/UC mMIMO networks, focusing on fronthaul constraints [39], [40], low CCP downlink [41] and uplink [42].

Even though it is not the interest of this paper, machine learning methods are also started to be used specifically for CF mMIMO networks. Using deep reinforcement learning (DRL), [43] dynamically partitions the network into subsystems and optimizes analog beam-steering operation. Lastly, [47] uses DRL to create an AP selection algorithm for CF mMIMO networks.

Table 1.1: Proposed Work (PW) vs. Related Literature

CF/UC mMIMO uplink	PW	[8] , [22]	[13]	[23]	[24] , [27]	[12] , [25]	[26]	[28]
Multi-Antenna APs	✓	✗	✓	✓	✓	✓	✓	✓
Hybrid/Fully Digital	✓/✗	✗/✓	✓/✗	✓/✗	✗/✓	✓/✗	✓/✗	✗/✓
Wideband (Multi-tap) Channel	✓	✗	✗	✓	✗	✗	✗	✓
SC-FDE/OFDM	✓/✗	✗/✗	✗/✗	✗/✓	✗/✗	✗/✗	✗/✗	✗/✓
UC-Scalable	✓	✓	✗	✗	✗	✗	✓	✓
Centralized/Distributed	✓/✗	✓/✗	✓/✓	✗/✓	✓/✗	✓/✗	✗/✓	✗/✓
Perfect/Imperfect CSI	✗/✓	✗/✓	✗/✓	✓/✗	✗/✓	✗/✓	✗/✓	✗/✓
Linear/Nonlinear Detector	✗/✓	✓/✗	✓/✗	✓/✗	✗/✓	✓/✗	✓/✗	✓/✗
High MIMO Load ($\geq$%100)	✓	✗	✗	✗	✗	✗	✗	✗

1.3 Contributions and Novelties

In spite of the expansion of the literature on CF/UC mMIMO networks operating at mmWave frequencies, there remains to be a gap in coverage of some perspectives. Previous works on hybrid beamformers have focused mainly on novel analog beamforming techniques [12]- [14] specifically tailored for distributed antenna configurations. However, digital beamforming methods still typically rely on standard methods for combiners, such as minimum-mean-squared-error (MMSE), zero-forcing (ZF), and maximum ratio combiner (MRC). Another barren subject in this field is non-linear interference cancellation methods which rely on iterative structures using some form of feedback. This is expected since using non-linear methods in CF networks makes it difficult, if not impossible, to write closed-form expressions for metrics like spectral efficiency (SE) and signal-to-interference plus noise ratio (SINR).

Due to the nature of linear combining methods, they cannot reliably support a high number of UEs compared to the total number of RF chains in the network [4], [8]. This thesis demonstrates that non-linear interference cancellation techniques can enable the servicing of a number of UEs that exceed the total number of RF chains in the network in UC mMIMO networks.

Another issue with current literature is that it primarily follows narrowband channel models [4], while broadband systems are becoming increasingly common [44]. Thus, it is crucial to prioritize frequency-selective channel models as well. Additionally, most research on frequency-selective channels assumes an OFDM modulation scheme, such as in [45]. To the best of the authors' knowledge, no prior work has considered a wide-band single carrier configuration for CF/UC mMIMO networks.

A comparison of the proposed work against the related literature can be seen in Table 1.1. The main contributions of this thesis are given below.

- A novel AB for UC mMIMO systems that depends on the slowly changing parameters. Every AP employs its own AB using a modified version of the known EB [12] called the MEB. MEB does not use large-scale gains for the AB matrix calculations, and it only includes the angle of arrival (AoA) information and the structure of the CCMs of the served UEs. This design choice promotes a notion of "fairness" by ensuring that the beamforming matrix does not disproportionately favor UEs with stronger channels. In scenarios where the large-scale gains are considered in an AP's AB, UEs with stronger channels tend to dominate the beamforming matrix, potentially neglecting UEs with weaker channels and compromising service uniformity. Given that uniform service is a crucial characteristic and a key advantage of the CF architecture, MEB intuitively emerges as a well-suited AB method for CF/UC mMIMO networks.

- A novel uplink receiver architecture called CFI-D in the digital domain for CF mMIMO networks with SC-FDE structure is derived. CFI-D is non-linear (iterative), and it is able to operate under extremely high loads. In CFI-D, all the APs serve all the UEs, and the IB-DFE operation encompasses all UEs.

- A novel uplink receiver architecture called UCIS-D in the digital domain for

UC mMIMO networks. Even though CFI-D has great performance, it is not scalable. UCIS-D offers a scalable UC alternative to CFI-D. In UCIS-D, every UE has its own detector with two stages. UCIS-D also operates in the frequency domain utilizing soft decision feedback. For a given UE, all the other (interfering) UEs are divided into three groups according to their relative "interference power". The strongest interferers are canceled in the second stage of the receiver. The weaker interferers are canceled in the first stage of the receiver. Lastly, the weakest interferers are ignored since they are most likely below the noise level, and it is not feasible to spend precious computation resources suppressing them (omitting the weakest interferers is actually common practice in the literature for UC networks [4]). The sizes of these groups are system parameters, and how they are chosen affects the CCP. The first stage of the receiver performs a PIC operation. Following the PIC operation, the second stage employs an IB-DFE operation. The IB-DFE operation is modified to consider and suppress the channel estimation errors and the residual interference from the PIC operation. The algorithm for UE-AP groupings and the UE selection procedure for PIC and IB-DFE operations are also given.

- Due to the non-linear natures of UCIS-D and CFI-D, it is not possible to write close-form SE or SINR expressions for a given UE. However, an SINR expression that depends on the soft decisions from the previous iteration is derived in this work. The AIR metric is introduced and derived for the given network also. AIR corresponds to a lower bound on the mismatch decoding capacity for a given UE when dealing with finite constellations. The AIR metric also reveals the performance of possible coding schemes.

Since closed-form SE and SINR expressions can not be written, Monte Carlo simulations are used to test the performance of the proposed methods. All the simulations are done in the MATLAB environment. BER and AIR metrics are used to evaluate the digital combiners, while SINR CDF curves are used to compare the AB methods.

Simulation results firstly show that MEB is superior to the EB and DFT ABs regarding BER and SINR performance. Secondly, the results show that UCIS-D outperforms Subset MMSE and MMSE combiners by a large margin regarding BER and AIR

performance. This result shows that computationally costly interference cancellation methods can be effectively used in a scalable manner, even in large UC mMIMO networks. This is due to the macro-diversity provided by the distributed network topology. In scenarios where a small number of APs serve a UE, only a select few UEs with the strongest channels to those APs will cause significant interference. To exploit this, UCIS-D employs computationally expensive interference cancellation methods (IB-DFE) to process the most harmful interferers while utilizing less computationally intensive methods (PIC) for mild interferers. Any remaining UEs with weak signals are ignored as they are likely below the noise level and not worth the computational resources, as mentioned before. Simulation results show that this approach outperforms both MMSE and Subset MMSE [8] detectors while remaining scalable.

1.4 The Outline of the Thesis

Chapter 2 introduces the system and network model along with the channel model. Chapter 3 explains the analog stage of the hybrid beamformer. The calculations of the AB matrices, the proposed AB method, and the beam patterns of several AB techniques are illustrated. Chapter 4 delves into the digital stage of the hybrid beamformer. The CF implementation of the IB-DFE structure is introduced for the proposed CFI-D. Then, the main contribution of the thesis, the UC-implemented UCIS-D, is explained. UE-AP association algorithm, a grouping of the interfering UEs, and the PIC-aided IB-DFE UC structure are presented. Chapter 5 presents the performance metrics that are used for the detectors, such as AIR and BER. The calculation of soft decisions, which the iterative detectors rely on to perform interference cancellation via frequency domain decision feedback, is also given in this chapter. Chapter 6 explains the simulation setups and demonstrates the simulation results to show the performance of proposed detectors. Finally, Chapter 7 draws the conclusions, and the future work planned around this thesis is listed.

CHAPTER 2

CELL-FREE NETWORK AND SYSTEM MODEL

2.1 Introduction

In this chapter, the network that is being considered is introduced. How the APs and UEs are distributed in the network is given. Mathematical representations of the signals considered and the used channel model are explained. The structure of the SC-FDE transmission scheme is introduced.

2.1.1 Notation and Nomenclature

The following notations are used throughout all the parts of the thesis. Unless otherwise stated, they always hold true.

Scalars are denoted by lowercase (e.g., x), column vectors by lowercase bold (e.g., $\mathbf{x}$), and matrices by uppercase bold (e.g., $\mathbf{X}$) letters. $|x|$ and $x*$ are the magnitude and complex conjugate of scalar x respectively. $\mathbf{X}^T$, $\mathbf{X}^H$, $\mathbf{X}^{-1}$ and $\mathrm{Tr}(\mathbf{X})$ represents the transpose, Hermitian, inverse and trace of matrix $\mathbf{X}$, respectively. $\lceil . \rfloor$ rounds to the closest and greater integer. $Q(.)$ is the Q-function. $[\mathbf{X}]_{ij}$ is the entry of matrix $\mathbf{X}$ at i^{th} row and j^{th} column. $\mathbf{X}(i,:)$ and $\mathbf{X}(:,j)$ are used to extract i^{th} row and j^{th} column of matrix $\mathbf{X}$, respectively. $\mathbb{E}\{.\}$ is the expectation operator. $\|\mathbf{x}\|$ denotes the Euclidean norm of vector $\mathbf{x}$. The operators diag$\{.\}$ and blkdiag$\{.\}$ are used to construct diagonal and block diagonal matrices. $\mathbf{I}_D$ is the identity matrix with size $D \times D$ and $\mathbf{0}_{D\times D}$ is a zero matrix with size $D \times D$. $\mathrm{vec}(\mathbf{X})$ is the vectorization of matrix $\mathbf{X}$. The expression $\sim \mathcal{N}_{\mathbb{C}}(\mathbf{x}, \mathbf{R})$ is a complex Gaussian random vector with mean $\mathbf{x}$ and covariance $\mathbf{R}$. The Kronecker product and Kronecker delta function are

denoted by $\bigotimes$ and δ_{ij}. Covariance matrix (CM) of $\mathbf{x}$ is denoted by $\mathbf{R}_{\mathbf{x}} = \mathbb{E}\{\mathbf{x}\mathbf{x}^H\}$. The cross-variance matrix between vectors $\mathbf{x}$ and $\mathbf{y}$ are denoted by $\mathbf{R}_{\mathbf{xy}} = \mathbb{E}\{\mathbf{x}\mathbf{y}^H\}$. $U[a, b]$ is a uniform random variable distributed between a and b. Operator $\measuredangle$ extracts the phase of a complex variable in radians. Also a modulo b is written as $(a)_b$

There are a lot of mathematical entities defined in the following chapters. To make it easier to follow the flow of the thesis, a nomenclature table containing some of the mathematical entities defined is given in Table 2.1 and Table 2.2.

2.1.2 System Model

2.1.2.1 Network Topology

Uplink transmission of a CF network is considered. The network is assumed to exist in a square area with an area of $500m \times 500m$. The network is assumed to have wrap-around topology [5] to mimic an environment with no edges and interference coming from all directions. This means that the upper border of the network area is connected to the lower border, and the left border is connected to the right border [4]. This allows the creation of a simulation where every UE is at the center of the network. The shortest possible path is considered while calculating the distance and the angle between an AP and a UE. There are K single antenna UEs uniformly and randomly located in the network. There are N APs, and they are located in a uniform grid layout. The layout is illustrated in Figure 2.1.

The APs are assumed to be connected to a CPU with an ideal fronthaul link with no quantization errors, infinite capacity, and zero transmission delay. Every AP employs a uniform linear array (ULA) with M antennas. The AB employed by the APs reduces the incoming signal dimension from M to D using phase shifters and attenuators. This means that there are D RF chains for every AP. The ABs and their properties will be explained in detail in Chapter 3. The antenna spacing for every ULA is half-wavelength. The array manifold vector $\mathbf{u}(\phi)$, of a ULA with half-wavelength spacing and M antennas is given in (2.1) for a given AoA ϕ [53].

$$\mathbf{u}(\phi) = [1 \; e^{j\pi \sin(\phi)} \; \ldots \; e^{j\pi \sin(\phi)(M-1)}]^T \in \mathbb{C}^M. \tag{2.1}$$

Table 2.1: Nomenclature table for the mathematical entities used.

Variable	Explanation
α_{kn}^{l} and $\mathbf{h}_{kn}^{l,\text{time}}$	Large-scale channel gain and unity power fast fading channel
$\mathbf{R}_{kn}^{l}$ and $\mathfrak{R}_{kn}^{l}$	Rayleigh and total CCMs of the channel
$\mathbf{A}_n$	Analog beamformer matrix of AP n
$\mathbf{y}_{nt}^{\text{time}}$ and $\tilde{\mathbf{y}}_{nt}$	Received signal by AP n in time domain and ETD
$\tilde{\mathbf{y}}_t$ and $\mathbf{y}_f$	Received signal by all APs in ETD and frequency domain
$\mathbf{H}_{n}^{l,\text{time}}$	Concatenated channel matrix of AP n at the l^{th} MPC in time
$\mathbf{h}_{kn}^{l,\text{time}}$ and $\tilde{\mathbf{h}}_{kn}^{l}$	Channel between UE k and AP n in time domain and ETD
$\tilde{\mathbf{H}}_{n}^{l}$ and $\tilde{\mathbf{H}}^{l}$	Concatenated channel matrix in ETD for AP n and all APs
$\mathbf{H}^{f}$	Concatenated channel matrix in the frequency domain for all APs
$\hat{\mathbf{H}}^{f}$ and $\mathbf{E}^{f}$	MMSE estimate and estimation error of $\mathbf{H}^{f}$
$\tilde{\mathbf{x}}_t$ and $\mathbf{x}_f$	Transmitted symbols in time domain and frequency domain
$\mathbf{h}_{kn}^{f}$	Normalized channel between UE k and AP n at frequency f
$\hat{\mathbf{h}}_{kn}^{f}$ and $\mathbf{e}_{kn}^{f}$	MMSE estimate of $\mathbf{h}_{kn}^{f}$ and its estimation error
$\mathbf{W}_{f}^{(i)}$ and $\mathbf{C}_{f}^{(i)}$	CFI-D feedforward and feedback filters
$\hat{\mathbf{x}}_{f}^{(i)}$ and $\hat{\tilde{\mathbf{x}}}_{t}^{(i)}$	Estimation of transmitted symbols $\mathbf{x}_f$ and $\tilde{\mathbf{x}}_t$ by detectors
$\mathbf{P}_{1}^{(i)}$ and $\mathbf{P}_{2}^{(i)}$	Reliability matrices for containing all UEs
$\bar{\mathbf{x}}_{f}^{(i-1)}$	Soft decisions from the previous iteration from all UEs
$\rho_{k}^{(i)}$ and $\beta_{k}^{(i)}$	Entries of $\mathbf{P}_{1}^{(i)}$ and $\mathbf{P}_{2}^{(i)}$ belonging to UE k
$\mathcal{N}_k$	Set of APs that serve UE k
$\mathcal{K}_n$	Set of UEs that get their channels estimated by AP n
$\mathcal{K}_{n}^{\mathfrak{s}}$	Set of UEs that AP n serves
$\mathcal{M}_k$	UEs that are in the $\mathcal{K}_n$ set of at least one of the APs in $\mathcal{N}_k$
$\mathbf{y}_{kf}$ and $\mathbf{y}_{kf}^{(i)}$	Row decimated received signal for UE k before and after PIC
$\mathbf{H}_{k}^{f}$	Row decimated version of $\mathbf{H}^{f}$
$\hat{\mathbf{H}}_{k}^{f}$ and $\mathbf{E}_{k}^{f}$	Column sparsified MMSE estimate and estimation error of $\mathbf{H}_{k}^{f}$
$\mathcal{S}_k$ and $\mathcal{S}'_k$	Set of UEs that are strong and weak interferers for UE k
$\hat{\mathbf{H}}_{k}^{f,\mathfrak{s}}$ and $\hat{\mathbf{H}}_{k}^{f,\mathfrak{s}'}$	Partition of $\hat{\mathbf{H}}_{k}^{f}$ containing columns corresponding to $\mathcal{S}_k$ and $\mathcal{S}'_k$
$\bar{\mathbf{x}}_{f,\mathfrak{s}}^{k,(i-1)}$, $\bar{\mathbf{x}}_{f,s'}^{k,(i-1)}$	Soft decisions belonging to UEs in $\mathcal{S}_k$, $\mathcal{S}'_k$

Table 2.2: Table 2.1 (continued).

Variable	Explanation
$\hat{x}_{kf}^{(i)}$ and $\hat{\tilde{x}}_{kt}^{(i)}$	Estimation of x_{kf} and $\tilde{x}_{kt}$ in time and frequency by filters
$\mathbf{R}_{\mathfrak{e}}^{k}$	CCM of the channel estimation error terms for UCIS-D
$\mathbf{R}_{\mathfrak{s}'}^{k,(i)}$	CCM of the terms from residual interference from PIC
$\mathbf{w}_{kf}^{(i)}$ and $\mathbf{c}_{kf}^{(i)}$	UCIS-D feedforward and feedback filters
$\mathbf{P}_{1,\mathfrak{s}}^{k,(i)}$ and $\mathbf{P}_{2,\mathfrak{s}}^{k,(i)}$	Reliability matrices with entries from UEs in $\mathcal{S}_k$
$\mathbf{P}_{1,\mathfrak{s}'}^{k,(i)}$ and $\mathbf{P}_{2,\mathfrak{s}'}^{k,(i)}$	Reliability matrices with entries from UEs in $\mathcal{S}_k'$
$\mu_k^{(i)}$ and $\eta_k^{(i)}$	Complex amplitude and residual interference of $\hat{\tilde{x}}_{kt}^{(i)}$

Note that the ULAs only consider the azimuth AoA. For simplicity, the elevation AoAs are ignored in this thesis. Since ULAs have only one dimension, it would not have been possible to beamform in two dimensions anyway.

2.1.2.2 Channel Model

As mentioned in Chapter 1, the network operates in mmWave frequencies. The channels between UEs and APs are assumed to be wide-band and modeled as tap-delay-line channels with scarce and multiple taps [48]. Representing the power, the channel between UE k and AP n has the large-scale gain α_{kn}, incorporating the transmit power and the path-loss terms. Shadowing effects are ignored for simplicity in this work. Note that α_{kn} is a large-scale parameter that varies slowly, meaning it is constant through many transmission blocks. Every channel consists of multiple multipath-components (MPCs). The number of MPCs is at most L for every channel. Note that, due to the scarce nature of mmWave channels, only a few of the L MPCs are assumed to be active [48]. The l'th MPC of the channel from UE k to AP n has two elements which are α_{kn}^{l} and $\mathbf{h}_{kn}^{l,\text{time}}$. The α_{kn}^{l} value represents the l^{th} MPC's power within the channel satisfying $\alpha_{kn} = \sum_{l=0}^{L-1} \alpha_{kn}^{l}$.

The terms α_{kn} and α_{kn}^{l} are calculated using a modified version of the mmWave model given in [52]. The α_{kn} value in dB is written as

$$\alpha_{kn}[\text{dB}] = \text{P}_x - 61.4 - 10\omega \log_{10}(d_{kn}) \tag{2.2}$$

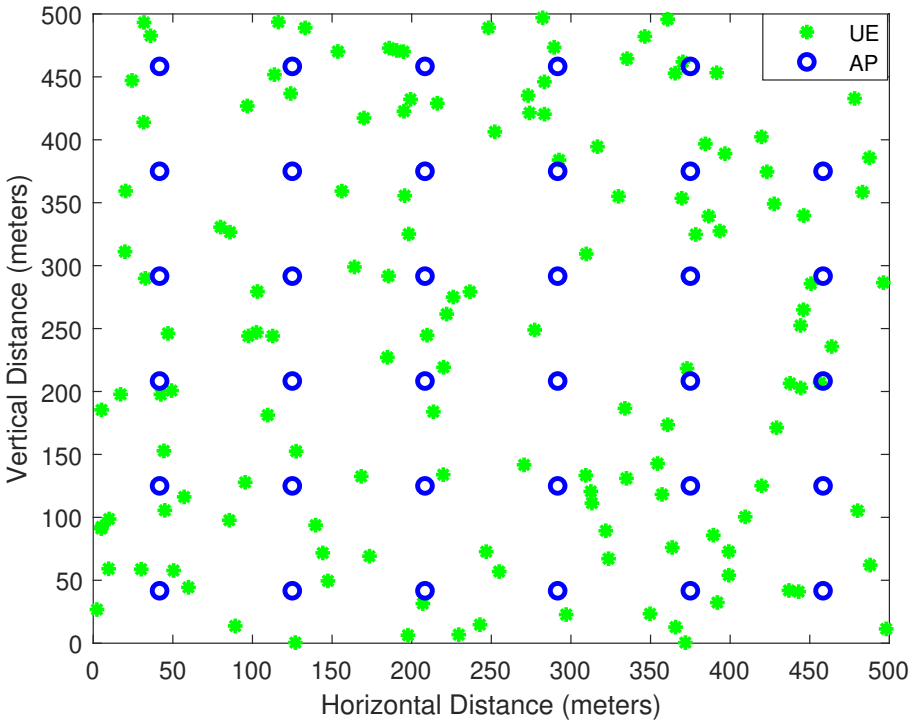

Figure 2.1: An example of the grid layout with $L = 36$ and $K = 144$.

where P_x is the UE uplink transmit power in dBm and d_{kn} is the distance between UE k and AP n in meters. The parameter ω is the path loss exponent. Note that there are works that tackle the power control problem within cell-free networks, such as [26], [28], [29], and [33]. However, the transmit power of all UEs is assumed to be equal in this thesis. While not optimal, this "heuristic" method is shown to be acceptable, performance-wise, in CF network literature [4]. Then for each active MPC l, we define the term $\bar{\gamma}_{kn}^{l}$ and it can be written [52] as $\bar{\gamma}_{kn}^{l} = U_{knl}^{1.8} 10^{-0.1 Z_k}$ provided that $U_{knl} \sim U[0,1]$ and $Z_k \sim \mathcal{N}(0, 4^2)$. To get the α_{kn}^{l} values, we normalize the $\bar{\gamma}_{kn}^{l}$ terms linearly to sum up to one to get γ_{kn}^{l} term leading to $\gamma_{kn}^{l} = \bar{\gamma}_{kn}^{l} / (\sum_{l'=0}^{L-1} \bar{\gamma}_{kn}^{l'})$. Note that γ_{kn}^{l} represents the portion of the power of the given MPC within the total channel power after the normalization operation satisfying $\alpha_{kn}^{l} = \alpha_{kn} \gamma_{kn}^{l}$.

Representing the random small-scale fading and the phased array structure at the AP n, $\mathbf{h}_{kn}^{l,\text{time}} \in \mathbb{C}^M$ is the fast fading portion of the channel, and it is taken as a Rician distribution written as

$$\mathbf{h}_{kn}^{l,\text{time}} \sim \mathcal{N}_{\mathbb{C}} \left(\kappa_{kn}^{l} \mathbf{u}(\phi_{kn}^{l}),\, \mathbf{R}_{kn}^{l} \right) \tag{2.3}$$

where ϕ_{kn}^{l} is the azimuth AoA of the considered MPC, $\kappa_{kn}^{l}\mathbf{u}(\phi_{kn}^{l})$ is the mean component, and $\mathbf{R}_{kn}^{l} \in \mathbb{C}^{M\times M}$ is the spatial correlation matrix for the Rayleigh part of the channel. The term κ_{kn}^{l} is the complex amplitude of the given channel's mean(constant) part. While $\left|\kappa_{kn}^{l}\right|$ depends on the K-Factor of the Rician channel, phase of κ_{kn}^{l} is assumed to be $\measuredangle\kappa_{kn}^{l} \sim U[0, 2\pi]$. Channels are assumed to be mutually uncorrelated among MPCs, APs, and UEs, which is expressed as

$$\mathbb{E}\{\mathbf{h}_{kn}^{l,\text{time}}(\mathbf{h}_{k'n'}^{l',\text{time}})^{H}\} = \left(\left|\kappa_{kn}^{l}\right|^{2}\mathbf{u}(\phi_{kn}^{l})(\mathbf{u}(\phi_{kn}^{l}))^{H} + \mathbf{R}_{kn}^{l}\right)\ \delta_{kk'}\delta_{nn'}\delta_{ll'}. \tag{2.4}$$

This assumption is intuitive since channels between different APs and a UE are unrelated, and different scatterers cause the different MPCs of a channel between a UE and an AP. It is feasible to model them as uncorrelated entities. Although there is an approach where closely located UEs have correlated channels to a given AP in mmWave networks [26], this thesis also assumes uncorrelated channels for this case since it is not the focus of the proposed work. Also, the CM of the term $\mathbf{h}_{kn}^{l,\text{time}}$ is written as

$$\mathfrak{R}_{kn}^{l} = \mathbb{E}\{\mathbf{h}_{kn}^{l,\text{time}}(\mathbf{h}_{kn}^{l,\text{time}})^{H}\}. \tag{2.5}$$

Spatial correlation matrix $\mathbf{R}_{kn}^{l}$ is calculated using the local scattering model from [5, Sec. 2.5]. Since only the azimuth AoAs are considered, the calculations are simpler for this work. The elements of $\mathbf{R}_{kn}^{l}$ can be computed as

$$[\mathbf{R}_{kn}^{l}]_{ab} = \zeta_{kn}^{l}\int\int e^{j\pi(a-b)sin(\bar{\phi})}f(\bar{\phi})d\bar{\phi} \tag{2.6}$$

where ζ_{kn}^{l} is related to the K-Factor of the Rician distribution and $f(\bar{\varphi})$ is a Gaussian distribution. For the AoA ϕ_{kn}^{l}, which acts as the mean of this distribution for the considered MPC. Then the Gaussian distribution for the l^{th} MPC of the channel between UE k and AP n can be written as

$$f(\bar{\phi}) = \frac{1}{\sqrt{2\pi}\sigma_{\phi}}e^{-\frac{(\bar{\phi}-\phi_{kn}^{l})^{2}}{2\sigma_{\phi}^{2}}} \tag{2.7}$$

where σ_{ϕ} is the angular standard deviation (ASD). Note that the normalization is done in a way that makes every entry of $\mathbf{h}_{kn}^{l,\text{time}}$ is expected to have unity power. This means that $\text{Tr}(\mathfrak{R}_{kn}^{l}) = M$. Also note that, $\text{Tr}(\mathbf{R}_{kn}^{l}) = M\zeta_{kn}^{l}$. Then $\left|\kappa_{kn}^{l}\right|^{2} + \zeta_{kn}^{l} = 1$. The Rician K-Factor for the MPC l can then be written as $\left|\kappa_{kn}^{l}\right|^{2}/\zeta_{kn}^{l}$. The instantaneous channel vectors ($\mathbf{h}_{kn}^{l,\text{time}}$) are assumed to be constant over one transmission block, while the CCMs ($\mathfrak{R}_{kn}^{l}$ and $\mathbf{R}_{kn}^{l}$) are assumed to be constant over several transmission blocks.

2.1.3 SC-FDE Transmission

The uplink transmission employs an SC-FDE structure. The received signal $\mathbf{y}_{nt}^{\text{time}} \in \mathbb{C}^M$ at AP n in time index t can be written as

$$\mathbf{y}_{nt}^{\text{time}} = \sum_{l=0}^{L-1} \mathbf{H}_n^{l,\text{time}} \tilde{\mathbf{x}}_{(t-l)_T} + \mathbf{n}_{nt}^{\text{time}} \tag{2.8}$$

for $t = 0, 1, \ldots, T-1$. Also, $\mathbf{H}_n^{l,\text{time}} \in \mathbb{C}^{M \times K}$ is the concatenated channel matrix of AP n at the l^{th} MPC. It is written as $\mathbf{H}_n^{l,\text{time}} \triangleq [\sqrt{\alpha_{1n}^l}\mathbf{h}_{1n}^{l,\text{time}} \ \sqrt{\alpha_{2n}^l}\mathbf{h}_{2n}^{l,\text{time}} \ \ldots \ \sqrt{\alpha_{Kn}^l}\mathbf{h}_{Kn}^{l,\text{time}}]$. T is the transmission block length.

UE k transmits the Z-QAM symbol $\tilde{x}_{kt} \in \mathbb{C}$ at time t and the overall UE transmit symbol vector at time t is defined as $\tilde{\mathbf{x}}_t \triangleq [\tilde{x}_{1t}, \tilde{x}_{2t} \ldots, \tilde{x}_{Kt}]^T \in \mathbb{C}^K$. A cyclic prefix with a length larger than L is used to obtain circulant channel matrices while preventing inter-block interference. The UE symbols are assumed to be of average unit power and uncorrelated between UEs and different times, i.e., satisfying the relation $\mathbb{E}\{\tilde{x}_{kt}(\tilde{x}_{k't'})^*\} = \delta_{kk'}\delta_{tt'}$, which leads to $\mathbb{E}\{\tilde{\mathbf{x}}_t(\tilde{\mathbf{x}}_{t'})^H\} = \mathbf{I}_K\delta_{tt'}$. The $\mathbf{n}_{nt}^{\text{time}} \in \mathbb{C}^M$ vector is the zero-mean circulant symmetric complex Gaussian (ZMCSCG) noise at the AP n at time t with $\mathbb{E}\{\mathbf{n}_{nt}^{\text{time}}(\mathbf{n}_{nt}^{\text{time}})^H\} = \mathbf{I}_M N_0$.

Although there are methods in the literature about estimating CCM properties in mMIMO [54] and for hybrid beamforming networks [55], the CMs given in (2.4) are assumed to be perfectly known by the detectors in this thesis for simplicity. However, the instantaneous channels are not known, and they still need to be estimated. Channel estimation is performed in the frequency domain, which is delved into in Chapter 4, and its details will be given there.

CHAPTER 3

ANALOG STAGE

3.1 Introduction

In Chapter 2, the network and system structures were introduced. The channel model was also given in detail. The time domain representations of the channel vectors, received, and transmitted signals were defined. In this section, the next step is taken, which is the AB stage.

As mentioned in Chapter 1, CF/UC mMIMO hybrid-beamforming structures have been studied in recent years [11]- [15], [23], [25], [26] and [34]- [43]. There are a lot of novel AB structures proposed both for centralized and distributed CF networks.

Since APs have very large antenna arrays due to working in the mmWave frequencies, some kind of reduction in the dimension of the received signals before the ADC operation is essential. This way, the number of RF chains (the components that affect the cost of implementation greatly) can be reduced. The main contribution of this thesis focuses on the digital part of the hybrid structure. However, the cited works above show that the AB stage can greatly impact performance. Therefore, an AB suited to its digital counterpart is also proposed. Some common AB methods are also introduced in this section, namely the DFT beamformer, EB, and Generalized EB (GEB). The AB proposed in this work (MEB) is also defined, and the beam-patterns of the different methods are compared.

3.2 Analog Beamforming

ABs reduce the dimension of the received signal from M to D at a single AP while exploiting the slowly varying properties of the channels. As mentioned, ABs are calculated once and used for many transmission blocks; therefore, slowly varying entities should be used to calculate them. Every AP employs its own independent AB.

ABs act on the time domain signals directly, and the ADC operation is done after. Therefore, the entities after the AB stage are referred to as the "effective time domain (ETD)" entities. ETD received signal at AP n is written as $\tilde{\mathbf{y}}_{nt} \in \mathbb{C}^D$ at time index t and it can be written as

$$\tilde{\mathbf{y}}_{nt} = (\mathbf{A}_n)^H \mathbf{y}_{nt}^{\text{time}}. \tag{3.1}$$

where $\mathbf{A}_n \in \mathbb{C}^{M \times D}$ is the analog beamformer matrix for the AP n. Notice that no time index is given (same AB is used for several transmission blocks) or type of AB is specified for matrix $\mathbf{A}_n$. Lastly, orthonormal AB matrices are desired which means $(\mathbf{A}_n)^H \mathbf{A}_n = \mathbf{I}_D$. This property ensures that the AB operation does not amplify the received noise components.

3.3 Analog Beamforming Techniques

3.3.1 Eigen Beamformer

The first AB that will be explored is the EB, where an example of it can be seen in [12]. First, the auxiliary $\mathbf{R}_s^n$ matrix for AP n is defined as

$$\mathbf{R}_s^n = \sum_{k \in \mathcal{K}_n^{\mathfrak{s}}} \sum_{l=0}^{L-1} \alpha_{kn}^l \mathfrak{R}_{kn}^l \in \mathbb{C}^{M \times M} \tag{3.2}$$

which can be inferred from (2.5) and $\mathcal{K}_n^{\mathfrak{s}}$ is the set of UEs that AP n serves. The meaning of an AP serving a UE will be explained in Chapter 4. Then we can write another auxiliary matrix as

$$\bar{\mathbf{A}}_n = [\mathbf{a}_1^n, \mathbf{a}_2^n, \ldots, \mathbf{a}_D^n] \tag{3.3}$$

where $\mathbf{a}_i^n$ is the eigenvector corresponding to i^{th} most dominant eigenvalue of $\mathbf{R}_s^n$. Then, to get orthonormalized analog beamformers, we use the QR decomposition of the $\bar{\mathbf{A}}_n$ matrix, which can be written as $\bar{\mathbf{A}}_n = \mathbf{A}_n\bar{\mathbf{R}}$ resulting in the EB matrix for AP n. The EB method specifications and how this selection of columns maximizes the mutual information between the received signals and the transmitted symbols can be seen in [49] if the interfering groups in [49] are taken as zero.

Note that EB illuminates all the MPCs of all the UEs served, considering their respective powers. The stronger MPCs and the UEs owning said MPCs get better illumination. Lastly, in [12], EB is not applied directly in the manner that is given above. Only the phases of the eigenvectors are used to obey a constant modulus constraint, which allows implementing the AB with only phase shifters. Such a constraint is not imposed in this work.

3.3.2 Generalized Eigen Beamformer

GEB is an improved version of the EB. While EB only illuminates the UEs being served, GEB also suppresses the UEs considered to be interferers [49]. Another auxiliary matrix called $\mathbf{R}_{s'}^n$ is defined as

$$\mathbf{R}_{s'}^n = \sum_{k \in \mathcal{K}_n^{\mathfrak{s}'}} \sum_{l=0}^{L-1} \alpha_{kn}^l \mathfrak{R}_{kn}^l \in \mathbb{C}^{M \times M} \tag{3.4}$$

where $\mathcal{K}_n^{\mathfrak{s}'}$ is the complement of $\mathcal{K}_n^{\mathfrak{s}}$, expressed as $\mathcal{K}_n^{\mathfrak{s}'} = \{1, 2, \ldots, K\} - \mathcal{K}_n^{\mathfrak{s}}$. Then we write the generalized eigenvalue problem expressed as

$$\mathbf{R}_s^n \mathbf{a}_i^n = \lambda_i \mathbf{R}_{s'}^n \mathbf{a}_i^n, \quad i = 1, 2, \ldots, M \tag{3.5}$$

where $\mathbf{a}_i^n$ is the same as before and λ_i is the corresponding eigenvalue. The rest of the calculation is the same as the EB counterpart. The equation (3.3) holds the same, and the QR decomposition method again is used to derive $\mathbf{A}_n$.

GEB introduces nulls corresponding to the AoAs of the MPCs of the interfering UEs in the beampattern. Typically, GEB outperforms EB in mMIMO systems, as mentioned in [49]. However, thorough testing revealed that this superiority does not hold true for CF/UC mMIMO systems. In traditional mMIMO systems, it is feasible to

assign angular sections and group UEs based on the AoAs of their MPCs. Consequently, the AB operation can easily illuminate a specific group while suppressing others. Nevertheless, this approach is not viable in CF/UC mMIMO systems due to the absence of a single dominant AP serving all UEs. Instead, several weaker APs are distributed. There is no practical grouping approach that can exploit the synergy between illumination and nulling. The testing has shown that, within the context of this thesis, attempting to nullify the interferers actually harms the UEs with weaker channels since the AoAs of interfering and served UEs can be intertwined.

3.3.3 Modified Eigen Beamformer

MEB is the proposed AB in this thesis. Notice that in (3.2), the matrix $\mathbf{R}_s^n$ is dominated by the UEs with the highest α_{kn} values. This means that the signal spaces of the UEs with strong channels to a given AP will be illuminated much more than the weaker UEs. This creates an issue for CF/UC networks since the main premise of such networks is providing uniform service. This issue can be alleviated by making the following adjustment and rewriting the matrix as

$$\mathbf{R}_s^n = \sum_{k \in \mathcal{K}_n^s} \sum_{l=0}^{L-1} \gamma_{kn}^l \mathfrak{R}_{kn}^l \in \mathbb{C}^{M \times M}. \tag{3.6}$$

If this matrix is used to construct the EB, a trend of fairness is promoted, and a more uniform service can be achieved. Even though every UE is treated equally, the relative powers of the MPCs are still taken into account, and the stronger MPCs of a UE are still illuminated more compared to the other MPCs of the same UE.

3.3.4 DFT Beamformer

The DFT beamformer is a widely used AB in the literature [50], [51]. It is very simple to implement, and it offers respectable performance. The DFT beamformer uses the normalized DFT matrix defined as $\mathbf{G} \in \mathbb{C}^{M \times M}$. The entry of $\mathbf{G}$ corresponding to a^{th} row and b^{th} column is written as

$$[\mathbf{G}]_{ab} = \frac{1}{\sqrt{M}} e^{-j\frac{2\pi}{M}(a-1)(b-1)}, \quad \text{for} \quad a, b = 1, 2, \ldots, M. \tag{3.7}$$

Notice that every column of the normalized DFT matrix corresponds to a discrete angle when the array manifold vector in (2.1) is considered. When an AoA of an MPC is decided to be illuminated, the column with the closest angle to the chosen AoA is added to the AB. D columns must be chosen to construct a complete AB. In this work, the DFT beamformer for AP n is constructed as follows:

- Choose the AoAs of the strongest MPCs (highest α_{kn}^{l} for every UE k) of the D UEs with the highest α_{kn} values.
- If there are less than D such UEs, start choosing the second strongest MPC of every UE one by one, then the third MPCs, and so on.
- If still less than D columns are chosen when all the MPCs of all served UEs are selected, choose the closest columns to the columns chosen in the first step.

3.4 Beam-Pattern Comparison

A good way to compare different ABs is to look into their beam-patterns. The beam-pattern can show the power that can be achieved at any angle ϕ with a given AB, and it can be written for AB $\mathbf{A}_n$ as [49] given below

$$B(\phi) = \frac{1}{M}(\mathbf{u}(\phi))^H \mathbf{A}_n \Big((\mathbf{A}_n)^H \mathbf{A}_n \Big)^{-1} (\mathbf{A}_n)^H \mathbf{u}(\phi). \tag{3.8}$$

The first scalar term in (3.8) is there to normalize the array manifold vector power. Figure 3.1 shows all four AB methods' beam-patterns in a mock-up network. Using a small example network allows us to demonstrate the crucial properties of all AB methods and why MEB suits the current application. There are only $N = 4$ APs and $K = 16$ UEs. Each AP has $M = 64$ antennas and $D = 4$ RF chains. This means that the $\mathbf{A}_n$ matrix has 64 rows and 4 columns. Though they are not important to what this plot aims to show, the rest of the network parameters are the same as in the simulation results given in Chapter 6. One of the APs which serve five UEs in this mock-up network is chosen. The AoAs of the served UEs and the interfering UEs are indicated with vertical lines of different colors. Each UE has multiple MPCs with different power values. There are several important observations to be made in this plot. Initially, it is evident that the DFT beamformer exhibits satisfactory power

delivery to the strongest MPCs of all UEs, except for UE 2. This limitation arises from the fact that the DFT beamformer can only allocate a fixed number of beams, denoted by the number of RF chains D. Consequently, if the AP serves more than D UEs, the weaker UEs are deprived of a dedicated beam. Analyzing the MEB pattern, we observe prominent peaks at approximately $-37°$, $-16°$, $3°$, and $27°$. These peaks can be inferred as the AoAs corresponding to the strongest MPCs of all the served UEs. Notably, the peak at $-37°$ exhibits greater width compared to the others due to the close proximity of the mentioned MPCs from UE 1 and UE 2. Therefore, this beam effectively serves both UEs. When scrutinizing the EB pattern at $-16°$ and $3°$, no discernible peaks are observed. This lack of peaks can be attributed to the higher power levels of the MPCs from UE 1 and UE 3 in comparison to those of UE 4 and UE 5. This observation aligns with the peaks at $-6°$ and $6°$, indicating that the secondary MPCs of UE 1 and UE 3 dominate over the primary MPCs of UE 4 and UE 5. This imbalance results in the unfair performance of the EB, suppressing the signals of already weak UEs while favoring the signals of stronger UEs. The plots for the EB and GEB exhibit significant similarity, except in the vicinity of $-37°$. In order to accommodate UE 1 and UE 2, the EB and MEB patterns display a peak in that region. However, since GEB aims to nullify interfering signals, the entire region is suppressed, consequently eliminating the signals from UE 1 and UE 2. This issue illustrates the problem with GEB within this framework: when interfering signals possess similar AoAs to the intended signals, nullification prevents the illumination of these intended signals, particularly if they originate from UEs with weaker channels. Digital beamforming techniques possess greater efficacy compared to analog beamforming techniques. Even if the interfering signal is illuminated during the analog stage, digital processing methods can still recover the signals from weak intended UEs. However, if the digital stage nullifies these weak UEs, it may not be possible to recover them in the digital domain. The network depicted in Figure 3.1 is relatively small in scale. With a significantly larger network ($N, K > 100$), a substantial overlap between intended and interfering UEs would occur, further reducing the feasibility of GEB. This plot effectively demonstrates why MEB suits the provided framework and highlights the fundamental issues with alternative methods. These problems are exacerbated as the network scales up.

3.5 Effective Time Domain Entities

As mentioned, the signals after the AB stage are referred to as the ETD entities. Before switching to the frequency domain, these will be defined and arranged.

The ETD received signal at AP n after the AB is written in (3.1). ETD channel vectors and noise vectors are defined as

$$\tilde{\mathbf{h}}_{kn}^{l} \triangleq (\mathbf{A}_n)^H \mathbf{h}_{kn}^{l,\text{time}} \in \mathbb{C}^D, \tag{3.9}$$

$$\tilde{\mathbf{n}}_{nt} \triangleq (\mathbf{A}_n)^H \mathbf{n}_{nt}^{\text{time}} \in \mathbb{C}^D \tag{3.10}$$

for $n = 1, 2, \ldots, N$, for $k = 1, 2, \ldots, K$, for $t = 0, 1, \ldots, T-1$ and also for $l = 0, 1, \ldots, L-1$. Until now, all operations have been done on a single AP scale. However, in the digital stage, the information from all (or a group of) APs will be jointly used. We define some concatenated matrices and vectors for ease of algebra and readability.

$$\tilde{\mathbf{H}}_{n}^{l} \triangleq (\mathbf{A}_n)^H \mathbf{H}_{n}^{l,\text{time}} = \left[\sqrt{\alpha_{1n}^{l}} \tilde{\mathbf{h}}_{1n}^{l} \;\; \sqrt{\alpha_{2n}^{l}} \tilde{\mathbf{h}}_{2n}^{l} \;\; \ldots \;\; \sqrt{\alpha_{Kn}^{l}} \tilde{\mathbf{h}}_{Kn}^{l} \right] \in \mathbb{C}^{D \times K}, \tag{3.11}$$

$$\tilde{\mathbf{H}}^{l} \triangleq [(\tilde{\mathbf{H}}_{1}^{l})^T \;\; (\tilde{\mathbf{H}}_{2}^{l})^T \;\; \ldots \;\; (\tilde{\mathbf{H}}_{N}^{l})^T]^T \in \mathbb{C}^{DN \times K}, \tag{3.12}$$

$$\tilde{\mathbf{y}}_t \triangleq [\tilde{\mathbf{y}}_{1t}^T \;\; \tilde{\mathbf{y}}_{2t}^T \;\; \ldots \;\; \tilde{\mathbf{y}}_{Nt}^T]^T \in \mathbb{C}^{DN \times 1}, \tag{3.13}$$

$$\tilde{\mathbf{n}}_t \triangleq [\tilde{\mathbf{n}}_{1t}^T \;\; \tilde{\mathbf{n}}_{2t}^T \;\; \ldots \;\; \tilde{\mathbf{n}}_{Nt}^T]^T \in \mathbb{C}^{DN \times 1} \tag{3.14}$$

for $n = 1, 2, \ldots, N$, for $t = 0, 1, \ldots, T-1$ and for $l = 0, 1, \ldots, L-1$. Matrices $\tilde{\mathbf{H}}_{n}^{l}$ and $\tilde{\mathbf{H}}^{l}$ correspond to ETD representations of the concatenated channel matrices and overall concatenated channel matrix. Vector $\tilde{\mathbf{y}}_t$ is the overall ETD received signal, and vector $\tilde{\mathbf{n}}_t$ is the overall ETD noise vector.

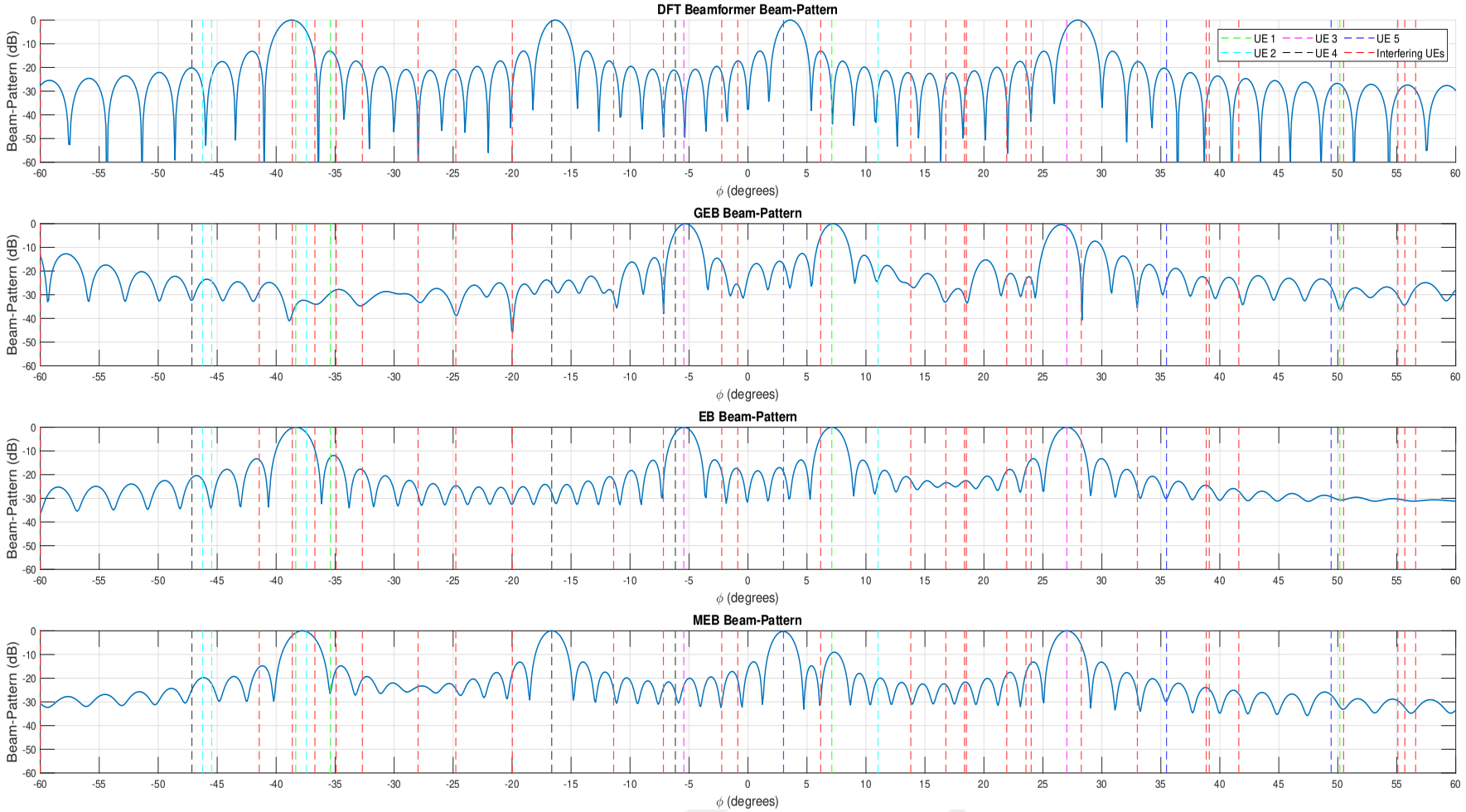

Figure 3.1: Beam-patterns of DFT Beamformer, GEB, EB, and MEB with $N = 4$ APs, $K = 16$ UEs in a network with an area of 500×500.

CHAPTER 4

DIGITAL STAGE

4.1 Introduction

This chapter contains the main contribution of this thesis. First, the switch from the time domain to the frequency domain is presented. Then the IB-DFE structure is driven for the NW operating CFI-D is derived. Then the UC operating UCIS-D is introduced. The processes of UE-AP groupings are explained. Newly introduced PIC operation and how it is integrated are given. IB-DFE operation is modified to suit the UC structure containing the residual properties from the PIC operation prior. Finally, the complete UCIS-D is derived as a scalable alternative to UCIS-D.

4.2 Frequency Domain Representation

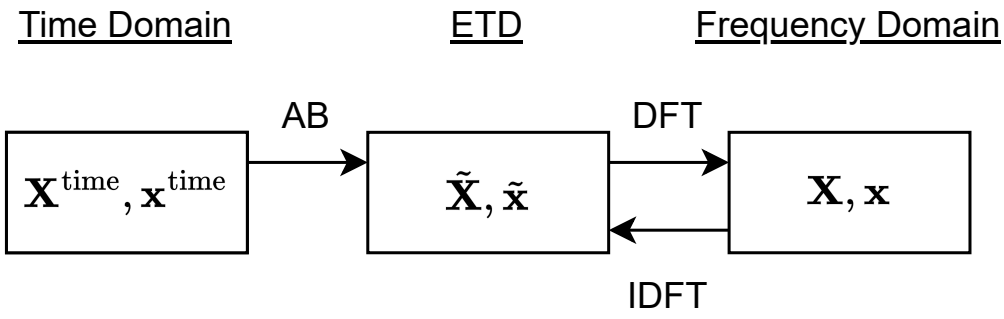

Figure 4.1: Relationship between different domains of representation.

There are three domains of representation mentioned up to now for some entities: the time domain, ETD, and the frequency domain. Figure 4.1 shows the convention

between these representations to avoid any confusion. The scalars, vectors, and matrices (only vector and the matrix cases are shown in Figure 4.1) denoted with the same letter can have up to three different representations. If there is an upper notation "time", this means the time domain representation. If there is a $\sim$ above the symbol, this corresponds to ETD after the AB operation. If no such indicators exist, then the symbol corresponds to the frequency domain representation. Note that this is not true for all symbols; it only holds true for the symbols sharing the same letter. For example, $\mathbf{A}_n$ matrix is not a frequency domain entity. Since no other matrix is denoted with the letter $\mathbf{A}$, it is compatible with the convention.

Using the ETD entities from Chapter 3, the following relation can be written to define the overall received signal in ETD.

$$\tilde{\mathbf{y}}_t = \sum_{l=0}^{L-1} \tilde{\mathbf{H}}^l \tilde{\mathbf{x}}_{(t-l)_T} + \tilde{\mathbf{n}}_t, \text{ for } t = 0, 1, \ldots, T-1. \tag{4.1}$$

All the DFT and normalized DFT (and IDFT and normalized IDFT) operations are T point in this work. The relation in (4.1) can be switched to the frequency domain as

$$\mathbf{y}_f = \mathbf{H}^f \mathbf{x}_f + \mathbf{n}_f \text{ for } f = 0, 1, \ldots, T-1. \tag{4.2}$$

DFT of the overall concatenated channel matrix is $\mathbf{H}^f = \sum_{l=0}^{L-1} \tilde{\mathbf{H}}^l e^{-j\frac{2\pi}{T}fl}$. Note that, in (4.2); $\mathbf{y}_f$, $\mathbf{x}_f$ and $\mathbf{n}_f$ are normalized DFTs of vector sequences $\tilde{\mathbf{y}}_t$, $\tilde{\mathbf{x}}_t$ and $\tilde{\mathbf{n}}_t$. Also $\mathbf{x}_f = [x_{1f}, x_{2f}, \ldots, x_{Kf}]^T$. Normalized DFT of any vector sequence $\{\tilde{\mathbf{z}}_t\}_{t=0}^{T-1}$ is denoted as $\mathbf{z}_f$ and it can be written as

$$\mathbf{z}_f = \frac{1}{\sqrt{T}} \sum_{t=0}^{T-1} \tilde{\mathbf{z}}_t e^{-j\frac{2\pi}{T}tf}. \tag{4.3}$$

The channel estimation is done in the frequency domain, as mentioned before. Reversing back from the concatenated representations to individuals ones in the frequency domain, the channel vector between UE k and AP n at f^{th} frequency bin can be written as $\sqrt{\alpha_{kn}}\mathbf{h}_{kn}^f$ where $\mathbf{h}_{kn}^f \in \mathbb{C}^{D\times 1}$ is the normalized(unity power) channel meaning $\text{Tr}(\mathbf{R}_{\mathbf{h}_{kn}^f}) = D$. Since the detector knows the large-scale gain terms, this normalized channel is the entity that is being estimated during the channel estimation. Also, note that

$$\mathbf{H}^f(:,k) = [\sqrt{\alpha_{k1}}(\mathbf{h}_{k1}^f)^T \sqrt{\alpha_{k2}}(\mathbf{h}_{k2}^f)^T \ \ldots \ \sqrt{\alpha_{kN}}(\mathbf{h}_{kN}^f)^T]^T. \tag{4.4}$$

Then, the following relations are written

$$\mathbf{h}_{kn}^{f} = \hat{\mathbf{h}}_{kn}^{f} + \mathbf{e}_{kn}^{f} \tag{4.5}$$

$$\mathbf{R}_{\hat{\mathbf{h}}_{kn}^{f}\mathbf{e}_{kn}^{f}} = \mathbf{0}_{D\times D} \tag{4.6}$$

where $\hat{\mathbf{h}}_{kn}^{f}$ is the MMSE estimation of $\mathbf{h}_{kn}^{f}$ and $\mathbf{e}_{kn}^{f}$ is the estimation error. Equation (4.6) results from estimation and error vectors being orthogonal to each other due to the nature of the MMSE estimation. Channel estimation is done with a pilot scheme. The details of channel estimation and pilot signaling processes are given in Appendix A. The CMs of the entities in (4.5) can be written as

$$\mathbf{R}_{\mathbf{h}_{kn}^{f}} = \mathbf{R}_{\mathbf{h}_{kn}} = \sum_{l=0}^{L-1} \gamma_{kn}^{l} (\mathbf{A}_n)^H \mathfrak{R}_{kn}^{l} \mathbf{A}_n \quad \forall f \tag{4.7}$$

$$\mathbf{R}_{\mathbf{e}_{kn}^{f}} = \mathbf{R}_{\mathbf{e}_{kn}} = [\mathbf{R}_{\mathbf{h}_{kn}}^{-1} + \alpha_{kn} \frac{E_T}{N_0} \mathbf{I}_D]^{-1} \quad \forall f \tag{4.8}$$

$$\mathbf{R}_{\hat{\mathbf{h}}_{kn}^{f}} = \mathbf{R}_{\hat{\mathbf{h}}_{kn}} = \mathbf{R}_{\mathbf{h}_{kn}} - \mathbf{R}_{\mathbf{e}_{kn}} \quad \forall f \tag{4.9}$$

where one should note that these matrices are not dependent on the frequency bin, f [49] and E_T is the pilot sequence power (Appendix A). Derivations of the equations in (4.7)-(4.9) are given in Appendix A.

4.3 Iterative SC-FDE Detectors

4.3.1 Cell-Free Iterative Detector

CFI-D is the first detector that will be introduced. CFI-D is a benchmark detector that operates at an NW level. This means that every AP serves every UE. While decoding UE k, the feedback from all the other UEs and the received signals from all the APs are utilized. While offering great performance, this approach is not feasible due to the computational cost it would require. However, it is valuable as a benchmark detector and building a mathematical foundation for the UCIS-D that will follow. CFI-D is the CF implementation of the SC-FDE IB-DFE framework. The block diagram of the overall operation can be seen in Figure 4.2. Actually, in Figure 4.2, the operation of UCIS-D is given. But it can also help understand the outline of the operation done by the CFI-D as well.

The IB-DFE structure in this paper is similar to [16], in which there is a co-located mMIMO structure. CFI-D also decodes the transmitted symbols using frequency domain decision feedback (FDDF) [16]. The feedforward and feedback filters at f^{th} frequency bin and i^{th} iteration are denoted by $\mathbf{W}_f^{(i)} \in \mathbb{C}^{DN\times K}$ and $\mathbf{C}_f^{(i)} \in \mathbb{C}^{K\times K}$ respectively. The digital filtering and the DFE output at i^{th} iteration can be written as

$$\hat{\mathbf{x}}_f^{(i)} = [\mathbf{W}_f^{(i)}]^H \mathbf{y}_f - [\mathbf{C}_f^{(i)}]^H \bar{\mathbf{x}}_f^{(i-1)}, \tag{4.10}$$

$$\hat{\bar{\mathbf{x}}}_t^{(i)} = \frac{1}{\sqrt{T}} \sum_{f=0}^{T-1} \hat{\mathbf{x}}_f^{(i)} e^{j\frac{2\pi}{T}ft} \tag{4.11}$$

by using (4.2) and the soft decisions, in the frequency domain, of the previous iteration denoted by $\bar{\mathbf{x}}_f^{(i-1)} \triangleq [\bar{x}_{1f}^{(i-1)}, \bar{x}_{2f}^{(i-1)}, \ldots, \bar{x}_{Kf}^{(i-1)}]^T$ for $t, f = 0, 1, \ldots, T-1$. Calculations of the soft decisions are given in Chapter 5.3. The time domain estimates in (4.11) which are denoted by $\hat{\bar{\mathbf{x}}}_t^{(i)} = [\hat{\bar{x}}_{1t}^{(i)}, \hat{\bar{x}}_{2t}^{(i)} \ldots, \hat{\bar{x}}_{Kt}^{(i)}]^T$, are used to demodulate the transmitted symbols, where $\hat{\bar{x}}_{kt}^{(i)}$ is the estimate of the symbol transmitted by UE k at time t denoted by $\tilde{x}_{kt}$ at i^{th} iteration. Also, estimation of the transmitted symbols in the frequency domain at i^{th} iteration is denoted by $\hat{\mathbf{x}}_f^{(i)} \triangleq [x_{1f}^{(i)}, x_{2f}^{(i)}, \ldots, x_{Kf}^{(i)}]^T$. The feedback filters should obey the following constraint for every UE k to prevent self-cancellation issues.

$$\sum_{f=0}^{T-1} \mathbf{C}_f^{(i)}(k,k) = 0 \tag{4.12}$$

The filters are found via the MMSE criterion. The total MSE for the estimation in (4.10) at i^{th} iteration is given as

$$\mathrm{MSE}_i \triangleq \mathbb{E}\left\{ \sum_{f=0}^{T-1} \|\hat{\mathbf{x}}_f^{(i)} - \mathbf{x}_f\|^2 \right\}. \tag{4.13}$$

The MMSE criterion results in T parallel equations, one for every frequency bin. Before deriving the feedforward and feedback filters, we define two matrices denoted by $\mathbf{P}_1^{(i)}$ and $\mathbf{P}_2^{(i)}$ called reliability matrices [16]. Reliability matrices are independent of the time-frequency index, block diagonal, and they are updated at every iteration. Matrix $\mathbf{P}_1^{(i)}$ represents the correlation between the soft decisions and the transmitted symbols, and $\mathbf{P}_2^{(i)}$ represents the correlation between soft decisions. The properties

of reliability matrices are as follows:

$$\mathbf{P}_1^{(i)} = \mathbb{E}\{\tilde{\mathbf{x}}_t(\tilde{\bar{\mathbf{x}}}_t^{(i-1)})^H\}, \quad \mathbf{P}_2^{(i)} = \mathbb{E}\{\tilde{\bar{\mathbf{x}}}_t^{(i-1)}(\tilde{\bar{\mathbf{x}}}_t^{(i-1)})^H\} \tag{4.14}$$

$$\mathbb{E}\{\tilde{\mathbf{x}}_t(\tilde{\bar{\mathbf{x}}}_{t'}^{(i-1)})^H\} = \mathbf{0}_{K\times K}, \quad \mathbb{E}\{\tilde{\bar{\mathbf{x}}}_{t'}^{(i-1)}(\tilde{\bar{\mathbf{x}}}_t^{(i-1)})^H\} = \mathbf{0}_{K\times K}, \forall \quad t \neq t' \tag{4.15}$$

$$\mathbb{E}\{\tilde{x}_{kt}(\tilde{\bar{x}}_{k't}^{(i)})^*\} = \rho_k^{(i)}\delta_{kk'}, \quad \mathbb{E}\{\tilde{\bar{x}}_{kt}^{(i)}(\tilde{\bar{x}}_{k't}^{(i)})^*\} = \beta_k^{(i)}\delta_{kk'} \tag{4.16}$$

$$\mathbf{P}_1^{(i)} = \text{diag}[\rho_1^{(i)}, \ldots, \rho_K^{(i)}], \quad \mathbf{P}_2^{(i)} = \text{diag}[\beta_1^{(i)}, \ldots, \beta_K^{(i)}]. \tag{4.17}$$

Notice that the expectations are independent of the time index and $\tilde{\bar{\mathbf{x}}}_t^{(i-1)}$ is the normalized IDFT of $\bar{\mathbf{x}}_f^{(i-1)}$. Also note that, $\tilde{\bar{\mathbf{x}}}_t^{(i)} = [\tilde{\bar{x}}_{1t}^{(i)}, \tilde{\bar{x}}_{2t}^{(i)}, \ldots, \tilde{\bar{x}}_{Kt}^{(i)}]^T$ which represents the soft decisions in time domain (or ETD). Also note that, due to the properties of normalized DFT and the uncorrelated symbols between UEs, the reliability matrix relations also hold in the frequency domain. This results in $\mathbf{P}_1^{(i)} = \mathbb{E}\{\mathbf{x}_f(\bar{\mathbf{x}}_f^{(i-1)})^H\}$ and $\mathbf{P}_2^{(i)} = \mathbb{E}\{\bar{\mathbf{x}}_f^{(i-1)}(\bar{\mathbf{x}}_f^{(i-1)})^H\}$. As mentioned before, reliability matrices will be calculated in Chapter 5.3.

Calculation of the feedforward and feedback filters also requires the CM of the received signal $\mathbf{y}_f$. Since the detector does not know the exact channels, the channel estimates are used along with the channel estimation CMs given in (4.7)-(4.9). Then the received signal CM can be written as

$$\mathbf{R}_{\mathbf{y}_f} = \hat{\mathbf{H}}^f(\hat{\mathbf{H}}^f)^H + \mathbf{R}_{\mathbf{E}^f} + N_0\mathbf{I}_{DN} \in \mathbb{C}^{DN\times DN} \tag{4.18}$$

$$\mathbf{H}^f = \hat{\mathbf{H}}^f + \mathbf{E}^f, \quad \mathbf{R}_{\mathbf{E}^f} = \mathbb{E}\{\mathbf{E}^f(\mathbf{E}^f)^H\}, \quad \mathbb{E}\{\mathbf{E}^f\} = \mathbf{0}_{DN\times K} \tag{4.19}$$

where $\hat{\mathbf{H}}^f$ and $\mathbf{E}^f$ are estimation and estimation error of $\mathbf{H}^f$. Relation (4.18) can be inferred from (4.2), (4.19) and the uncorrelation between different channels, channel estimates, and their estimation errors and the independence of the noise entities and finally the relation $\mathbb{E}\{\mathbf{x}_f(\mathbf{x}_f)^H\} = \mathbf{I}_K$ which can be inferred from applying Parseval's relation between $\mathbf{x}_f$ and $\tilde{\mathbf{x}}_t$. Also, $\mathbf{R}_{\mathbf{E}^f}$ is the CM of the channel estimation error; it has a block diagonal structure since the channel estimation errors are uncorrelated between channels to different APs. Then we can write $\mathbf{R}_{\mathbf{E}^f}$ as

$$\mathbf{R}_{\mathbf{E}^f} = \text{blkdiag}\left\{\sum_k \alpha_{k1}\mathbf{R}_{\mathbf{e}_{k1}}, \sum_k \alpha_{k2}\mathbf{R}_{\mathbf{e}_{k2}}, \ldots, \sum_k \alpha_{kN}\mathbf{R}_{\mathbf{e}_{kN}}\right\}. \tag{4.20}$$

Every block in the relation (4.20) represents the CMs of all channel estimation errors to the particular AP. They are summed, and there are no cross-terms since channels belonging to different UEs have uncorrelated channel estimation errors.

Now filters $\mathbf{W}_f^{(i)}$ and $\mathbf{C}_f^{(i)}$ can be derived according to the criterion in (4.13). Lagrangian multipliers method is used with the constraint given in (4.12). The Lagrangian cost function and the Lagrangian coefficients at the i^{th} iteration can be written as

$$J^{(i)} = \mathrm{MSE}_i + \sum_{f=0}^{T-1}\left(\sum_{k=1}^{K}[\mathbf{C}_f^{(i)}(k,k)]^*\Gamma_k^{(i)}\right) \tag{4.21}$$

$$\mathbf{\Gamma}^{(i)} = \mathrm{diag}(\Gamma_1^{(i)}, \Gamma_2^{(i)}, \ldots, \Gamma_K^{(i)}). \tag{4.22}$$

The details of the solution of the Lagrangian multipliers method are given in Appendix B, and the optimal filters are then found to be

$$\mathbf{W}_f^{(i)} = (\mathbf{R}_{\mathbf{y}_f})^{-1}\hat{\mathbf{H}}^f[\mathbf{I}_K + \mathbf{P}_1^{(i)}\mathbf{C}_f^{(i)}], \tag{4.23}$$

$$\mathbf{C}_f^{(i)} = \mathbf{A}_f^{(i)}[\mathbf{D}_f^{(i)} - \mathbf{\Gamma}^{(i)}] \tag{4.24}$$

for $f = 0, 1, \ldots, T-1$ both. Auxiliary matrices $\mathbf{A}_f^{(i)}$ and $\mathbf{D}_f^{(i)}$ are defined and derived at the end of Appendix B along with the Lagrangian coefficients. Finally, the Lagrangian coefficients can be written as

$$\Gamma_k^{(i)} = \frac{\sum_{f=0}^{T-1}\mathbf{A}_f^{(i)}(k,:)\mathbf{D}_f^{(i)}(:,k)}{\mathbf{A}_f^{(i)}(k,k)}, \text{ for } k = 1, \ldots, K. \tag{4.25}$$

Note that the first iteration performed with filters $\mathbf{W}_f^{(1)} = (\mathbf{R}_{\mathbf{y}_f})^{-1}\hat{\mathbf{H}}^f$ and $\mathbf{C}_f^{(1)} = \mathbf{0}_{K\times K}$ is the linear MMSE (LMMSE) filtering, which will be referred as network-wide MMSE (NW-MMSE). The NW-MMSE is important since it is a staple of literature in CF network-related research [4], [7], [8].

4.3.2 User-Centric Iterative Subset Detector

In this section, the main contribution of the thesis, which is the UCIS-D, will be explained. In the CFI-D, every AP serves every UE. While this is a good method performance-wise, the CCP with this method rises in an unbounded manner when the network gets larger. CCP of a method can be thought of as the number of complex multiply-and-accumulate (MA) operations needed to perform it. To evaluate a method CCP-wise, a metric called "scalability" is introduced similar to [4] and [7]. For a detector to be scalable, the *CCP per UE* must remain finite as the number of

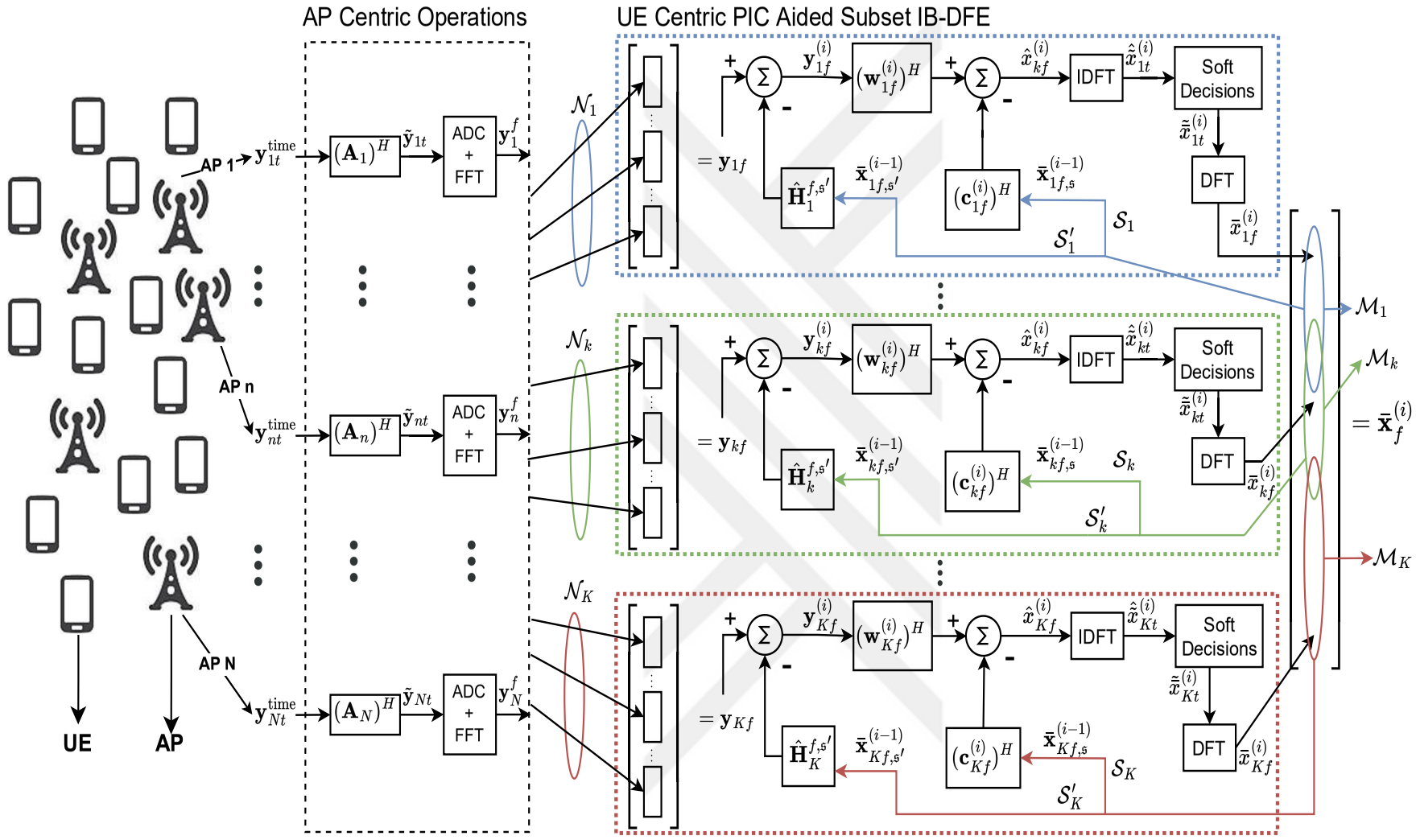

Figure 4.2: Block diagram of the overall operation done by the UCIS-D.

UEs and/or the number of APs in the network goes to infinity within a transmission block [4]. This does not mean that the network should be able to serve an infinite number of UEs with finite CCP; rather, it means that the CCP of decoding a UE in a large network should be bounded to a finite value. By definition, the CFI-D given in the previous section is inherently unscalable due to matrix inversions in (4.23) and (B.12). This section aims to introduce the motive behind the proposed alternative detectors, not to provide a deep CCP analysis. A complete CCP analysis will be given in Chapter 5.5 instead. As a final remark before moving to the details of UCIS-D, the implementations of CFI-D and UCIS-D differ in a major way. In CFI-D, the filters operate on all UEs simultaneously with the same matrices. In UCIS-D, every UE is decoded separately in a UC fashion, i.e., each UE has its own detector. Though, these detectors use information from each other while conducting interference cancellation operations. The overall operation done by the UCIS-D can be seen as a block diagram in Figure 4.2.

4.3.2.1 Subset Grouping

To enable a UC approach in UCIS-D, every UE has an assigned group of APs that serve them similarly to [8]. The set of APs that serve the UE k is denoted with $\mathcal{N}_k$ with cardinality $\bar{\mathcal{N}}$. Semi-reciprocally, the set of UEs whose channels are estimated in the digital domain by the AP n is the set $\mathcal{K}_n$ with cardinality $\bar{\mathcal{K}}$. The UEs in the set $\mathcal{K}_n$ are the UEs either AP n serves or the UEs who are strong interferers to the AP n whose channels are estimated in the digital domain by AP n for interference cancellation purposes. The cardinality $\bar{\mathcal{N}}$ is a system parameter. The cardinality $\bar{\mathcal{K}}$ depends on the $\bar{\mathcal{N}}$ value which is given as $\bar{\mathcal{K}} = \lceil \varrho \bar{\mathcal{N}} K/L \rceil$. The value ϱ is also a system parameter with the condition $\varrho \geq 1$. Note that if $\varrho = 1$ is chosen, all APs only estimate the channels of the UEs they serve. Subset grouping should be done based on large-scale coefficients and not the fast-fading channels. This way, the same grouping can be used for many transmission blocks, and the detector does not have to calculate the sets at every block similar to [8]. Every UE is served by the same number of APs, and every AP estimates the channels of the same number of UEs in the digital domain.

The calculation and construction of the sets $\mathcal{N}_k$ and $\mathcal{K}_n$ are given in Algorithm (1). For the first stage, one-by-one APs are assigned to the UEs they will serve. This is done by comparing α_{kn} values. For UE k, the APs with the largest α_{kn} values are added to the set $\mathcal{N}_k$. For every AP n that is assigned to $\mathcal{N}_k$, UE k is also assigned to $\mathcal{K}_n$ since APs have to estimate the channels of UEs they serve. After all the $\mathcal{N}_k$ sets are calculated, all the $\mathcal{K}_n$ sets may not be filled (this is true when $\varrho > 1$). For the second stage, the remaining slots in the $\mathcal{K}_n$ sets are then assigned with the same method as in the first step. Note that the assignments done in the second stage are used for interference cancellation purposes since APs do not serve the UEs that are assigned in this second stage. The set $\mathcal{K}_n^{\mathfrak{s}}$ used in (3.2) for the EB can now be explicitly defined as $\mathcal{K}_n^{\mathfrak{s}} = \{k | n \in \mathcal{N}_k\}$.

Algorithm 1 AP and UE Grouping for UCIS-D

Initialization: For a given setup choose the parameters $\bar{\mathcal{N}}$ and ϱ. Set $\bar{\mathcal{K}} = \lceil \varrho \bar{\mathcal{N}} K/N \rceil$.
$i = 1$, $k = 1$, $\mathcal{N}_k = \emptyset$ for all k, $\mathcal{K}_n = \emptyset$ for all n
while $i \leq \bar{\mathcal{N}}$ **do**
    while $k \leq K$ **do**
        $n = \{n | \alpha_{kn} > \alpha_{kn'} \; \forall \, n' \neq n$ with $n, n' \notin \mathcal{N}_k$ and $|\mathcal{K}_n|, |\mathcal{K}_{n'}| \neq \bar{\mathcal{K}}\}$
        $\mathcal{N}_k = \mathcal{N}_k \bigcup \{n\}$
        $\mathcal{K}_n = \mathcal{K}_n \bigcup \{k\}$
        $k = k + 1$
    end while
    $i = i + 1$
end while
$n = 1$
while $n \leq N$ **do**
    while $|\mathcal{K}_n| < \bar{\mathcal{K}}$ **do**
        $k = \{k | \alpha_{kn} > \alpha_{k'n} \; \forall \, k' \neq k$ with $k, k' \notin \mathcal{K}_n \}$
        $\mathcal{K}_n = \mathcal{K}_n \bigcup \{k\}$
    end while
    $n = n + 1$
end while

It is expected that, while UCIS-D decodes UE k if the network gets large, there is a high probability that some of the UEs' channels will not be estimated by any of the APs that serve UE k. For this purpose we define the set $\mathcal{M}_k$ for every UE k as

$$\mathcal{M}_k \triangleq \bigcup_{n \in \mathcal{N}_k} \mathcal{K}_n. \tag{4.26}$$

The set $\mathcal{M}_k$ defines the set of UEs that are at least in one of the $\mathcal{K}_n$ sets of one of the APs that serve UE k. Note that UE k itself is in the set $\mathcal{M}_k$ as well. Also set $\mathcal{M}'_k$ is defined as relative complement of $\mathcal{M}_k$, defined as $\mathcal{M}'_k = \{1, 2, \ldots, K\} \setminus \mathcal{M}_k$.

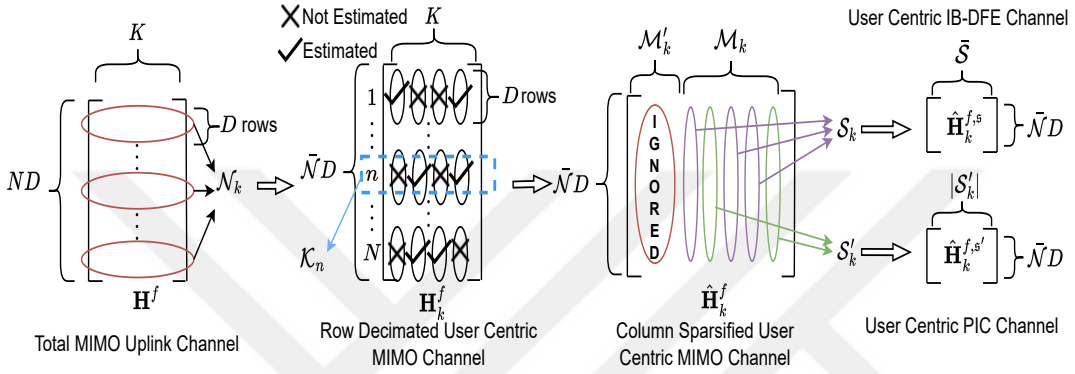

Figure 4.3: Visualization of row decimation and column sparsification processes done on the channel matrices. Followed by partitioning of the channel matrix according to $\mathcal{S}_k$ and $\mathcal{S}'_k$ sets.

4.3.2.2 Row Decimation

Since every UE has its own decoder, we need to define UC mathematical entities to outline the UCIS-D operations. The received signal $\mathbf{y}_f$ has ND rows; only $\bar{N}D$ rows are from the APs that serve the UE k. Curbing to only these rows, which will be referred to as "row decimation" similar to [8], the received signal vector for the k^{th} UE is defined as $\mathbf{y}_f^k \in \mathbb{C}^{\bar{N}D}$ and the received noise vector for UE k becomes $\mathbf{n}_f^k \in \mathbb{C}^{\bar{N}D}$. The channel matrix $\mathbf{H}^f$ with the same convention is written as $\mathbf{H}_k^f \in \mathbb{C}^{\bar{N}D \times K}$. The k_1^{th} column of $\mathbf{H}_k^f$ has a total of $\bar{N}D$ rows. Sequentially, every D rows of $\mathbf{H}_k^f$ corresponds to the channel between UE k_1 and a different AP from the set $\mathcal{N}_k$. Then, the row decimated version of (4.2) can be written as,

$$\mathbf{y}_{kf} = \mathbf{H}_k^f \mathbf{x}_f + \mathbf{n}_f^k. \tag{4.27}$$

for every UE k. From this point forward, all the operations are assumed to be done on a fixed UE k. Know that they are done for all UEs separately. The row decimation process on the channel matrix can be seen in the second stage of Figure 4.3.

4.3.2.3 Column Sparsification

At this point, the "column sparsification" process is introduced. In UCIS-D, not all the channels inside $\mathbf{H}_k^f$ are estimated according to Algorithm 1. The partial (column sparsified) estimation of $\mathbf{H}_k^f$ is written as $\hat{\mathbf{H}}_k^f$, and the estimation error is given as $\mathbf{E}_k^f$. Column sparsification is the process of setting the entries in $\hat{\mathbf{H}}_k^f$ and $\mathbf{E}_k^f$ corresponding to the un-estimated channels to zero. Note that columns of $\hat{\mathbf{H}}_k^f$ belonging to UEs in the set $\mathcal{M}_k'$ are completely zero. Also, some UEs will be inside the set $\mathcal{M}_k$, but they will not be in the $\mathcal{K}_n$ set of every AP n that is in the set $\mathcal{N}_k$. This is why in the matrix $\hat{\mathbf{H}}_k^f$, some columns will have both non-zero and zero rows, depending on the AP those rows correspond to and whether that AP estimates the channel of the corresponding UE. The visualization of the column sparsification processes can be seen in the third step of Figure 4.3.

4.3.2.4 Grouping the Interfering UEs

The row decimation, depending on $\bar{\mathcal{N}}$ and ϱ, greatly reduces the CCP of calculation of the feedforward filter in (4.23) compared to CFI-D. This is mainly due to the reduction of the size of the matrix in (4.18) that will be inverted. The CCP of calculation of the feedback filter in (4.24) is also reduced. Instead of inverting a $K \times K$ matrix, now a $|\mathcal{M}_k| \times |\mathcal{M}_k|$ matrix can be inverted for every UE k. While this option, in theory, is scalable as long as $|\mathcal{M}_k| < K$, there are also a few problems with this approach as well. Note that $|\mathcal{M}_k|$ is generally different for every UE. This means that the CCP of decoding every UE can change drastically depending on the network arrangement. This is not something that is desired; it is generally better to have a similar and consistent CCP for decoding every UE. This also helps with the analysis when there are new UEs being introduced to the network or old UEs leaving the network. Also, if $|\mathcal{M}_k|$ gets large for only one UE k, it can create a bottleneck in the decoding oper-

ation. To combat this issue, an alternative step to CFI-D is introduced. A PIC stage is introduced before performing the computationally costly IB DFE stage. Some of the interfering UEs will be processed with PIC, while the remaining UEs will be processed with the stronger IB-DFE.

The PIC operation is just a simple subtraction, and no matrix inversions are needed for it. After the PIC operation, the IB-DFE operation afterward must also consider the residual interference coming from the PIC operation as well. This will be given in more detail further into this Chapter.

Before going forward with these ideas, a selection of UEs must be made to choose which UEs will be processed with PIC and which UEs will be processed with IB-DFE.

First, we define two sets of UEs for every UE k, which will be called $\mathcal{S}_k$ and $\mathcal{S}'_k$. Note that $\mathcal{S}_k \cup \mathcal{S}'_k = \mathcal{M}_k \ \forall k$ and $\mathcal{S}_k \cap \mathcal{S}'_k = \emptyset \ \forall k$. While decoding the UE k, the UEs in the set $\mathcal{S}_k$ are processed with IB-DFE, and the UEs in the set $\mathcal{S}'_k$ are processed with PIC. The cardinality of the set $\mathcal{S}_k$ written as $\bar{\mathcal{S}}$, directly affects the CCP since the feedback filter will contain a matrix inverse of size $\bar{\mathcal{S}} \times \bar{\mathcal{S}}$. The cardinality $\bar{\mathcal{S}}$ is the same for all UEs. However, the cardinality of the set $\mathcal{S}'_k$ is not the same for all UEs, and it affects the PIC operation. Since $\bar{\mathcal{S}}$, $\bar{\mathcal{N}}$, and D are known, the matrix inversion sizes are completely controlled. Also, the $\mathcal{S}'_k$ set is only used for a one-step subtraction; it has much less impact on the CCP compared to matrix inversions. Therefore, not knowing the cardinality of $\mathcal{S}'_k$ is not as crucial.

The set $\mathcal{S}_k$ is determined by the relative interference power of other UEs to UE k. The metric of relative interference power of UE k_2 onto UE k_1 is defined as $P_{k_2}^{k_1}$, it can be written as

$$P_{k_2}^{k_1} \triangleq \sum_{f=0}^{T-1} \frac{|(\hat{\mathbf{H}}_{k_1}^{f}(:,k_1))^H \hat{\mathbf{H}}_{k_1}^{f}(:,k_2)|^2}{\|\hat{\mathbf{H}}_{k_1}^{f}(:,k_1)\|^2} \tag{4.28}$$

for a given realization. Using this metric allows us to choose the interferers that are mostly "aligned" with the signal space of the intended UE. Then the set $\mathcal{S}_{k_1}$ for UE k_1 is composed of UE k_1 itself and UEs with the highest relative interference power to UE k_1 according to (4.28). Remaining UEs within $\mathcal{M}_{k_1}$ constitute the set $\mathcal{S}'_{k_1}$. This way, the stronger interferers are processed with the more effective IB-DFE method,

while the weaker interferers are processed with the weaker PIC method. Since the matrix inversion will have the size $\bar{\mathcal{S}} \times \bar{\mathcal{S}}$, the dominant term of the CCP of the calculation of the feedback filter (in (4.24)) will be the same for all UEs.

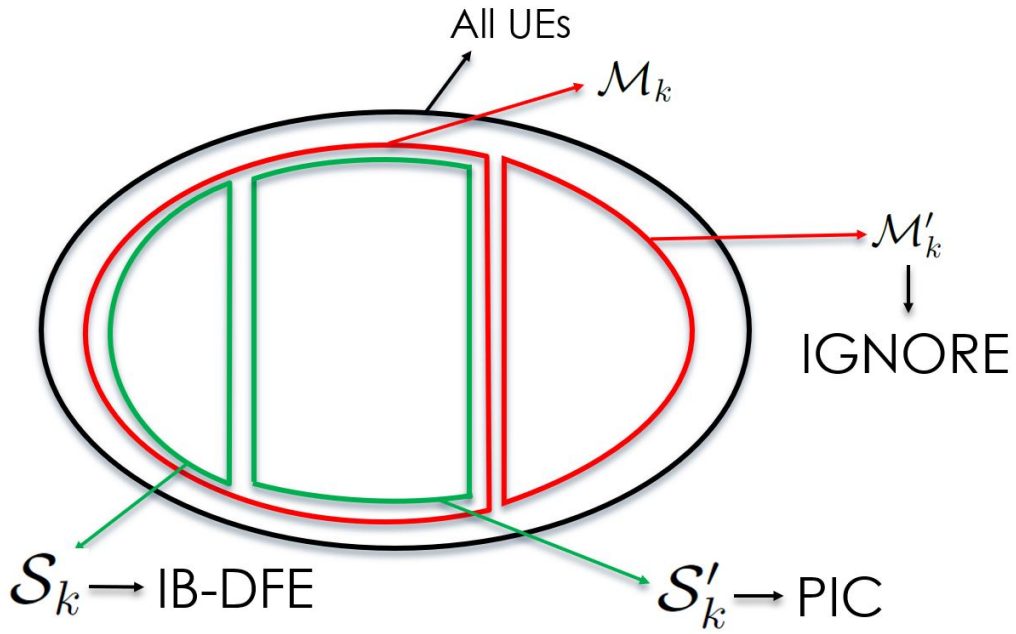

Figure 4.4: Visualization of the UE grouping sets $\mathcal{M}_k$, $\mathcal{M}'_k$, $\mathcal{S}_k$ and $\mathcal{S}'_k$.

To offer a better understanding of the interfering UE grouping, Figure 4.4 presents a visualization for the sets $\mathcal{M}_k$, $\mathcal{M}'_k$, $\mathcal{S}_k$ and $\mathcal{S}'_k$ and how they are related to one another.

To factor in $\mathcal{S}_k$ and $\mathcal{S}'_k$ sets into the operations, the matrix $\hat{\mathbf{H}}_k^f$ is partitioned into two matrices which are $\hat{\mathbf{H}}_k^{f,\mathfrak{s}} \in \mathbb{C}^{\mathcal{N}D \times \bar{\mathcal{S}}}$ and $\hat{\mathbf{H}}_k^{f,\mathfrak{s}'} \in \mathbb{C}^{\mathcal{N}D \times |\mathcal{S}'_k|}$. The partition is made such that matrix $\hat{\mathbf{H}}_k^{f,\mathfrak{s}}$ gets the columns of $\hat{\mathbf{H}}_k^f$ matrix corresponding to UEs in the set $\mathcal{S}_k$, $\hat{\mathbf{H}}_k^{f,\mathfrak{s}'}$ gets the columns corresponding to the UEs in the set $\mathcal{S}'_k$. A similar division is made for partitioning $\mathbf{E}_k^f$ into $\mathbf{E}_k^{f,\mathfrak{s}}$ and $\mathbf{E}_k^{f,\mathfrak{s}'}$ as well. The columns belonging to UEs in the set $\mathcal{M}'_k$ are ignored as they are the weakest interferers to UE k. The partitioning of these matrices can be seen more clearly in the visualization presented in the fourth and final step of Figure 4.3.

4.3.2.5 PIC aided IB-DFE

As mentioned before, the UCIS-D starts with a PIC operation. The PIC for UE k is done on the received signal $\mathbf{y}_{kf}$ directly on every frequency bin. It is done again using the soft decisions from the previous iteration, and for the i^{th} iteration, it is written as

$$\mathbf{y}_{kf}^{(i)} = \mathbf{y}_{kf} - \hat{\mathbf{H}}_k^{f,\mathfrak{s}'} \bar{\mathbf{x}}_{f,s'}^{k,(i-1)} \text{ for } f = 0, 1, \ldots, T-1 \tag{4.29}$$

where $\mathbf{y}_{kf}^{(i)}$ is the received signal after the PIC for UE k at the f^{th} frequency bin and $\bar{\mathbf{x}}_{f,\mathfrak{s}'}^{k,(i-1)}$ is the soft decisions belonging to the UEs in the set $\mathcal{S}_k'$. Note that a similar IB-DFE operation to the one in (4.10) and (4.11) can now be carried in a UC fashion as

$$\hat{x}_{kf}^{(i)} = (\mathbf{w}_{kf}^{(i)})^H \mathbf{y}_{kf}^{(i)} - (\mathbf{c}_{kf}^{(i)})^H \bar{\mathbf{x}}_{f,\mathfrak{s}}^{k,(i-1)} \tag{4.30}$$

$$\hat{\hat{x}}_{kt}^{(i)} = \frac{1}{\sqrt{T}} \sum_{f=0}^{T-1} \hat{x}_{kf}^{(i)} e^{j\frac{2\pi}{T}ft} \tag{4.31}$$

for $f = 0, 1, \ldots, T-1$. The vector $\bar{\mathbf{x}}_{f,\mathfrak{s}}^{k,(i-1)}$ is the soft decisions from the previous iteration belonging to the UEs in the set $\mathcal{S}_k$. The $\mathbf{w}_{kf}^{(i)} \in \mathbb{C}^{\mathcal{N}D}$ is the feedforward filter for UE k at frequency bin f and iteration i. Similarly, $\mathbf{c}_{kf}^{(i)} \in \mathbb{C}^{\bar{\mathcal{S}}}$ is the feedback filter. Note that the sizes of feedforward and feedback filters are decreased to accommodate the lower number of UEs that are processed compared to CFI-D.

There will be residual interference from the PIC operation, and the following IB-DFE operation must account for it to work properly. Namely, the CM analogous to the one in (4.18) changes after the PIC operation. To reduce the overall CCP, the residual interference is incorporated not with the instantaneous channels but with the CMs. This allows for a common residual interference term to be written, which leads to avoiding $|\mathcal{S}_k'|$ size matrix multiplications at every iteration for every frequency bin. Since $|\mathcal{S}_k'|$ is not known precisely and can get large, this reduction is impactful.

Using (4.29), covariance of $\mathbf{y}_{kf}^{(i)}$ can be given as

$$\mathbf{R}_{\mathbf{y}_{kf}^{(i)}} = \hat{\mathbf{H}}_k^{f,\mathfrak{s}} (\hat{\mathbf{H}}_k^{f,\mathfrak{s}})^H + N_0 \mathbf{I}_{DN} + \mathbf{R}_{\mathfrak{e}}^k + \mathbf{R}_{\mathfrak{s}'}^{k,(i)}. \tag{4.32}$$

The matrix $\mathbf{R}_{\mathfrak{e}}^k$ is a block diagonal matrix that is added due to channel estimation errors. The matrix $\mathbf{R}_{\mathfrak{s}'}^{k,(i)}$ is also a block diagonal matrix which is added due to the

residual interference from the PIC operation in (4.29). The calculation of the matrices $\mathbf{R}_{\mathfrak{c}}^{k}$ and $\mathbf{R}_{\mathfrak{s}'}^{k,(i)}$ and the derivation of (4.32) are given in Appendix C.

Now the filters can be calculated in a very similar to CFI-D. The MSE criterion for UE k in UCIS-D becomes

$$\mathrm{MSE}_i \triangleq \mathbb{E}\left\{\sum_{f=0}^{T-1} \|\hat{x}_{kf}^{(i)} - x_{kf}\|^2\right\}. \tag{4.33}$$

Also, for UCIS-D, the constraint in (4.12) becomes

$$\sum_{f=0}^{T-1} \mathbf{c}_{kf}^{(i)}(k) = 0. \tag{4.34}$$

Due to now being only one constraint, there is only one Lagrangian coefficient as well. Then the Lagrangian cost function for UCIS-D filters can be written as

$$J^{(i)} = \mathrm{MSE}_i + \sum_{f=0}^{T-1}\left((\mathbf{c}_{kf}^{(i)}(k))^{*}\bar{\Gamma}_{k}^{(i)}\right) \tag{4.35}$$

where $\bar{\Gamma}_{k}^{(i)}$ is the Lagrangian coefficient. The solution of the Lagrangian multipliers method for UCIS-D is given in Appendix D. The optimal filters then are found to be

$$\mathbf{w}_{kf}^{(i)} = \mathbf{R}_{\mathbf{y}_{kf}^{(i)}}^{-1}[\hat{\mathbf{H}}_{k}^{f,\mathfrak{s}}\mathbf{P}_{1,\mathfrak{s}}^{k,(i)}\mathbf{c}_{kf}^{(i)} + \hat{\mathbf{H}}_{k}^{f,\mathfrak{s}}(:,k_{\mathcal{S}})], \tag{4.36}$$

$$\mathbf{c}_{kf}^{(i)} = \mathbf{A}_{f}^{k,(i)}[\mathbf{d}_{f}^{k,(i)} - \bar{\mathbf{\Gamma}}_{k}^{(i)}]. \tag{4.37}$$

for $f = 0, 1, \ldots, T-1$ both. The auxiliary matrix $\mathbf{A}_{f}^{k,(i)}$ and auxiliary vector $\mathbf{d}_{f}^{k,(i)}$ are defined and derived at the end of Appendix D along with the Lagrangian coefficient. Finally the Lagrangian coefficient can be written as

$$\bar{\Gamma}_{k}^{(i)} = \frac{\sum_{f=0}^{T-1}\mathbf{A}_{f}^{k,(i)}(k_{\mathcal{S}},:)\mathbf{d}_{f}^{k,(i)}}{\sum_{f=0}^{T-1}\mathbf{A}_{f}^{k,(i)}(k_{\mathcal{S}},k_{\mathcal{S}})}. \tag{4.38}$$

Note that $k_{\mathcal{S}}$ is the index of UE k in the set $\mathcal{S}_k$ and the matrices $\mathbf{P}_{1,\mathfrak{s}}^{k,(i)}$ and $\mathbf{P}_{2,\mathfrak{s}}^{k,(i)}$ are reliability matrices derived in a similar fashion as (4.17), containing the entries for the UEs that are in the set $\mathcal{S}_k$. Finally, $\bar{\mathbf{\Gamma}}_{k}^{(i)}$ in (4.37) is a $\bar{\mathcal{S}} \times 1$ column vector with only one non-zero entry. The $k_{\mathcal{S}}^{th}$ entry is the non-zero entry with the value $\bar{\Gamma}_{k}^{(i)}$.

CHAPTER 5

PERFORMANCE METRICS AND RELIABILITY MATRIX CALCULATIONS

5.1 Introduction

This Chapter is about comparing different detectors. As mentioned in Chapter 1, it is not possible to write closed-form expressions for SE and SINR values. However, using the Bussgang Decomposition [17], an SINR can be defined for a given iteration with the condition of fixed and given filters, soft decisions, and transmitted symbols. Therefore, defining an SINR metric working with a Monte Carlo simulation is possible. Since the detectors do not know the true channels, the SINR expression is derived for two different cases. The first is the SINR value that the detector can calculate with the limited information it has. This SINR value is used for reliability matrix calculations by the detectors. The second is the true SINR experienced by the UEs.

Another performance metric that can be defined is the AIR (Chapter 1). AIR allows one to find a lower bound to the mismatch decoding capacity under finite constellations. Since QAM-type modulation is assumed on the transmitted symbols, the AIR metric provides a good insight into the network capacity. Finally, the AIR metric indicates the necessary level of coding scheme strength for achieving satisfactory performance.

The calculation of the soft decisions and reliability matrices are also given in this chapter. A standard analytical BER expression for QAM transmission, which is calculated using the SINR value found by Bussgang Decomposition, is also provided.

Finally, at the end of the chapter, a detailed CCP analysis is given for CFI-D, UCIS-D, and NW-MMSE detectors.

5.2 Bussgang Decomposition, SINR

The Bussgang Decomposition is done separately for CFI-D and UCIS-D.

5.2.1 CFI-D

First, the SINR value that the detector can calculate is derived. Bussgang Decomposition [17] of DFE output at i^{th} iteration for the symbol transmitted by UE k at time t given in (4.11) can be written as

$$\hat{\tilde{x}}_{kt}^{(i)} = \mu_k^{(i)} \tilde{x}_{kt} + \eta_k^{(i)} \quad \text{for} \quad t = 0, 1, \ldots, T-1 \tag{5.1}$$

where $\mu_k^{(i)}$ and $\eta_k^{(i)}$ are the complex amplitude and residual interference, respectively, of the transmitted symbol of UE k at time t. Note that, the transmitted symbol $\tilde{x}_{kt}$ and the residual interference term $\eta_k^{(i)}$ are uncorrelated. The $\mu_k^{(i)}$ term in (5.1) can be calculated by using (4.2), (4.10) and (4.11) as follows

$$\mu_k^{(i)} = \frac{\mathbb{E}\left\{\hat{\tilde{x}}_{kt}^{(i)} (\tilde{x}_{kt})^*\right\}}{\mathbb{E}\left\{|\tilde{x}_{kt}^{(i)}|^2\right\}} = \frac{1}{T} \sum_{f=0}^{T-1} \left[\mathbf{W}_f^{(i)}(:,k)\right]^H \hat{\mathbf{H}}^f(:,k) \tag{5.2}$$

The residual interference power in (5.1) can be calculated as $\mathbb{E}\{|\eta_k^{(i)}|^2\} = \mathbb{E}\{|\hat{\tilde{x}}_{kt}^{(i)}|^2\} - |\mu_k^{(i)}|^2$ where

$$\begin{aligned}
\mathbb{E}\{|\hat{\tilde{x}}_{kt}^{(i)}|^2\} &= \frac{1}{T} \sum_{f=0}^{T-1} \left[\mathbf{W}_f^{(i)}(:,k)\right]^H \mathbf{R}_{\mathbf{y}_f} \mathbf{W}_f^{(i)}(:,k) \\
&+ \frac{1}{T} \sum_{f=0}^{T-1} \left[\mathbf{C}_f^{(i)}(:,k)\right]^H \mathbf{P}_2^{(i)} \mathbf{C}_f^{(i)}(:,k) \\
&- \frac{2}{T} \sum_{f=0}^{T-1} \mathrm{Re}\left\{\left[\mathbf{W}_f^{(i)}(:,k)\right]^H \hat{\mathbf{H}}^f \mathbf{P}_1^{(i)} \mathbf{C}_f^{(i)}(:,k)\right\}
\end{aligned} \tag{5.3}$$

which can be obtained by using Parseval's relation between (4.10) and (4.11). Note that the terms $\mu_k^{(i)}$ and $\mathbb{E}\{|\eta_k^{(i)}|^2\}$ are independent of the time index, so they are calculated once for a given channel realization. Then the output SINR of UE k at iteration

i can be written as

$$SINR_i^k = |\mu_k^{(i)}|^2 / \mathbb{E}\left\{|\eta_k^{(i)}|^2\right\}. \tag{5.4}$$

Note that this SINR value is used by the detector and is not the true SINR experienced by the UEs. The true SINR written as $\overline{SINR_i^k}$ and it can be written as

$$\overline{SINR_i^k} = |\mu_k^{(i)}|^2 / \mathbb{E}\left\{|\bar{\eta}_k^{(i)}|^2\right\}. \tag{5.5}$$

Note that the numerator term does not change for the true SINR. Even if the true signal power term differs from the expression in (5.2) due to the disparity between the true and estimated channels, it does not matter. Since the detector does not know the true channels, it can not exploit this potential "extra" signal term. Therefore the additional interference due to mentioned disparity is added to the denominator, but the additional signal term is not added to the numerator. A new residual interference term $\bar{\eta}_k^{(i)}$ is introduced. This term contains the true interference experienced by UE k. To write down this term, the true CM of the received signal $\mathbf{y}_f$, written as $\bar{\mathbf{R}}_{\mathbf{y}_f}$, is defined as

$$\bar{\mathbf{R}}_{\mathbf{y}_f} = \mathbf{H}^f (\mathbf{H}^f)^H + N_0 \mathbf{I}_{DN}. \tag{5.6}$$

Then the true residual interference power can be written as

$$\begin{aligned}
\mathbb{E}\left\{|\bar{\eta}_k^{(i)}|^2\right\} &= \frac{1}{T}\sum_{f=0}^{T-1}\left[\mathbf{W}_f^{(i)}(:,k)\right]^H \bar{\mathbf{R}}_{\mathbf{y}_f}\mathbf{W}_f^{(i)}(:,k) \\
&+ \frac{1}{T}\sum_{f=0}^{T-1}\left[\mathbf{C}_f^{(i)}(:,k)\right]^H \mathbf{P}_2^{(i)}\mathbf{C}_f^{(i)}(:,k) \\
&- \frac{2}{T}\sum_{f=0}^{T-1}\mathrm{Re}\left\{\left[\mathbf{W}_f^{(i)}(:,k)\right]^H \mathbf{H}^f\mathbf{P}_1^{(i)}\mathbf{C}_f^{(i)}(:,k)\right\} - |\mu_k^{(i)}|^2
\end{aligned} \tag{5.7}$$

The SINR in (5.4) is used by the detector to calculate the soft decisions and the reliability matrix entries; however, in the simulation results, the true SINR given in (5.5) and the entities calculated with the true SINR values are presented for objectivity.

5.2.2 UCIS-D

The Bussgang decomposition and the capacity calculations are similar for UCIS-D. However, there are still distinctions. The same symbols as in CFI-D are used here as

well. These entities are about the transmitted symbols by the UEs, and they are not tied to any detector type for simplicity. Bussgang Decomposition [17] of DFE output at i^{th} iteration for the symbol transmitted by UE k at time t given in (4.31) is written in the exact same way as

$$\hat{\tilde{x}}_{kt}^{(i)} = \mu_k^{(i)} \tilde{x}_{kt} + \eta_k^{(i)} \tag{5.8}$$

The $\mu_k^{(i)}$ term in (5.8) can be calculated by using (4.29), (4.30) and (4.31) as follows

$$\mu_k^{(i)} = \frac{\mathbb{E}\left\{\hat{\tilde{x}}_{kt}^{(i)} (\tilde{x}_{kt})^*\right\}}{\mathbb{E}\left\{|\tilde{x}_{kt}^{(i)}|^2\right\}} = \frac{1}{T}\sum_{f=0}^{T-1} (\mathbf{w}_{kf}^{(i)})^H \hat{\mathbf{H}}_k^{f,\mathfrak{s}}(:, k_{\mathcal{S}}). \tag{5.9}$$

The residual interference power in (5.8) can be calculated as $\mathbb{E}\{|\eta_k^{(i)}|^2\} = \mathbb{E}\{|\hat{\tilde{x}}_{kt}^{(i)}|^2\} - |\mu_k^{(i)}|^2$ where

$$\begin{aligned}\mathbb{E}\{|\hat{\tilde{x}}_{kt}^{(i)}|^2\} &= \frac{1}{T}\sum_{f=0}^{T-1} (\mathbf{w}_{kf}^{(i)})^H \mathbf{R}_{\mathbf{y}_{kf}^{(i)}} \mathbf{w}_{kf}^{(i)} + \frac{1}{T}\sum_{f=0}^{T-1} (\mathbf{c}_{kf}^{(i)})^H \mathbf{P}_{2,\mathfrak{s}}^{k,(i)} \mathbf{c}_{kf}^{(i)} \\ &- \frac{2}{T}\sum_{f=0}^{T-1} \mathrm{Re}\left\{(\mathbf{w}_{kf}^{(i)})^H \hat{\mathbf{H}}_k^{f,\mathfrak{s}} \mathbf{P}_{1,\mathfrak{s}}^{k,(i)} \mathbf{c}_{kf}^{(i)}\right\}\end{aligned} \tag{5.10}$$

which can be obtained by using Parseval's relation between (4.30) and (4.31). Again note that the terms $\mu_k^{(i)}$ and $\mathbb{E}\{|\eta_k^{(i)}|^2\}$ are still independent of the time index, so they are calculated once for a given channel realization. Then the output SINR of UE k can be written the same way in (5.4). Again note that this SINR value is used by the detector and is not the true SINR of the system. For UCIS-D, the true SINR of the system is again written the exact same way as in (5.5). The term $\mathbb{E}\left\{|\bar{\eta}_k^{(i)}|^2\right\}$ for UCIS-D can be written as

$$\begin{aligned}\mathbb{E}\left\{|\bar{\eta}_k^{(i)}|^2\right\} &= \frac{1}{T}\sum_{f=0}^{T-1} (\mathbf{w}_{kf}^{(i)})^H \bar{\mathbf{R}}_{\mathbf{y}_{kf}} \mathbf{w}_{kf}^{(i)} \\ &+ \frac{1}{T}\sum_{f=0}^{T-1} (\mathbf{c}_{kf}^{(i)})^H \mathbf{P}_{2,\mathfrak{s}}^{k,(i)} \mathbf{c}_{kf}^{(i)} + \frac{1}{T}\sum_{f=0}^{T-1} (\bar{\mathbf{c}}_{kf}^{(i)})^H \mathbf{P}_{2,\mathfrak{s}'}^{k,(i)} \bar{\mathbf{c}}_{kf}^{(i)} \\ &- \frac{2}{T}\sum_{f=0}^{T-1} \mathrm{Re}\left\{(\mathbf{w}_{kf}^{(i)})^H \mathbf{H}_k^{f,\mathfrak{s}} \mathbf{P}_{1,\mathfrak{s}}^{k,(i)} \mathbf{c}_{kf}^{(i)}\right\} \\ &- \frac{2}{T}\sum_{f=0}^{T-1} \mathrm{Re}\left\{(\mathbf{w}_{kf}^{(i)})^H \mathbf{H}_k^{f,\mathfrak{s}'} \mathbf{P}_{1,\mathfrak{s}'}^{k,(i)} \bar{\mathbf{c}}_{kf}^{(i)}\right\} - |\mu_k^{(i)}|^2\end{aligned} \tag{5.11}$$

where $\bar{\mathbf{R}}_{\mathbf{y}_{kf}} = \mathbf{H}_k^f (\mathbf{H}_k^f)^H + N_0 \mathbf{I}_{DN}$. Also, $\bar{\mathbf{c}}_{kf}^{(i)} = (\mathbf{w}_{kf}^{(i)})^H \hat{\mathbf{H}}_k^{f,\mathfrak{s}'}$ and the matrices $\mathbf{P}_{1,\mathfrak{s}'}^{k,(i)}$ and $\mathbf{P}_{2,\mathfrak{s}'}^{k,(i)}$ are reliability matrices derived in a similar fashion as (4.17), containing

the entries for the UEs that are in the set $\mathcal{S}'_k$. Lastly, the matrices $\mathbf{H}_k^{f,\mathcal{S}}$ and $\mathbf{H}_k^{f,\mathcal{S}'}$ are the partitions of the matrix $\mathbf{H}_k^f$. Matrix $\mathbf{H}_k^{f,\mathcal{S}}$ contains the columns belonging to UEs in the set $\mathcal{S}_k$ and the matrix $\mathbf{H}_k^{f,\mathcal{S}'}$ contains the columns belonging to UEs in the set $\mathcal{S}'_k$. The relation in (5.11) can be derived in a similar way to (5.10) with using (4.27), (4.29), (4.30) and (4.31). The difference is that the true channels are assumed to be known, and expectations are taken with that in consideration.

5.3 Reliability Matrix Calculations

The reliability matrices depend only on soft decisions. The soft decisions used in CFI-D are calculated from (5.1),(5.2) and (5.3). The soft decisions used in UCIS-D are calculated from (5.8),(5.9) and (5.10). The residual interference term $\eta_k^{(i)}$ is assumed to be a Gaussian random variable with variance $\mathbb{E}\{|\eta_k^{(i)}|^2\}$. Since the IB-DFE operation is non-linear, this assumption is not exactly true. However, under light loads, the assumption is very accurate [46]. Simulation results in Chapter 6 will also show that the assumption holds under practical scenarios.

The distortion term $\eta_k^{(i)}$ is assumed to be uncorrelated with the transmitted symbol $\tilde{x}_{kt}$. Soft decisions are then taken as the expected value i.e. $\tilde{\hat{x}}_{kt}^{(i)} \triangleq \mathbb{E}\{\tilde{x}_{kt}|\hat{\tilde{x}}_{kt}^{(i)}\}$ with the Gaussianity assumption. Note that soft decisions are calculated first in the time domain ($\tilde{\hat{x}}_{kt}^{(i)}$) and then their normalized DFTs ($\bar{x}_{ft}^{(i)}$) are used in the filters at every iteration.

5.4 AIR and Analytical BER

Two types of BER are defined. The first type of BER is the simulation BER which is calculated with Monte Carlo simulations. The second type is the theoretical BER which is calculated with the true SINR value. Then for a Z-QAM modulation the theoretical BER of the network at i^{th} iteration is written as

$$BER = \sum_{k=1}^{K} \frac{4(1-1/\sqrt{Z})}{K\log_2 Z}\mathbb{E}\left\{Q\left(\sqrt{\frac{3}{Z-1}\overline{SINR_i^k}}\right)\right\}. \tag{5.12}$$

The second performance metric is AIR. In [18], a lower bound on the AIR is defined using the generalized mutual information concept. We can write the lower bound on AIR for UE k at i^{th} iteration as

$$AIR_k^{(i)} = \log_2 Z - \mathbb{E}_{\hat{\tilde{x}}_{kt}^{(i)},\mathfrak{u}} \left\{ \log_2 \left(\frac{\sum_{\mathfrak{u}' \in \mathfrak{U}} \tilde{p}(\hat{\tilde{x}}_{kt}^{(i)} | \mathfrak{u}')}{\tilde{p}(\hat{\tilde{x}}_{kt}^{(i)} | \mathfrak{u})} \right) \right\} \tag{5.13}$$

where $\tilde{p}(\hat{\tilde{x}}_{kt}^{(i)} | \mathfrak{u})$ is the mismatched PDF. The actual transmitted symbol is $\mathfrak{u}$, and $\mathfrak{U}$ is the QAM symbol alphabet. The mismatched PDF, with the Gaussian assumption, can be written as

$$\tilde{p}(\hat{\tilde{x}}_{kt}^{(i)} | \mathfrak{u}) = \frac{1}{\pi \, \mathbb{E}\{|\eta_k^{(i)}|^2\}} \exp\left(- \frac{|\hat{\tilde{x}}_{kt}^{(i)} - \mu_k^{(i)} \mathfrak{u}|^2}{\mathbb{E}\{|\eta_k^{(i)}|^2\}} \right). \tag{5.14}$$

Using (5.14), the AIR lower bound in (5.13) can be calculated.

5.5 Computational Complexity and Scalability

CCP and scalability were mentioned in the previous chapters to explain the motivation behind UCIS-D without going into detail. This section presents a detailed CCP analysis. Table 5.1 provides the CCP of various parts of given methods in terms of the number of MA operations. Note that operations that are done once for many transmission blocks are not added to the table, such as subset grouping and analog beamformer calculation, since they depend on slowly changing parameters. Also, inherently scalable operations like calculating soft decisions, FFT, IFFT, and demodulation are not included since they always have finite CCP per UE. Multiplying matrices of sizes $m \times n$ and $n \times p$ needs mnp MA. Inverting an $m \times m$ matrix needs m^3 MA. Table 5.1 includes UCIS-D, CFI-D, and NW-MMSE detectors. Also, remember that Table 5.1 shows the CCP needed per UE. It can be seen that CFI-D is unscalable since, per UE, CCP depends on K^2 and N^2. NW-MMSE is also unscalable since the CCP per UE depends on N^2. UCIS-D has a lot of extra terms, but it can be seen that it is overall scalable.

Also note that, while calculating the inverse of (4.32), a matrix with size $\bar{\mathcal{N}}D \times \bar{\mathcal{N}}D$ is inverted at every iteration for every UE. However, if $\bar{\mathcal{S}}$ is chosen to be less than

$\bar{\mathcal{N}}D$, only a matrix of size $\bar{\mathcal{S}} \times \bar{\mathcal{S}}$ needs to be inverted if Woodbury matrix identity is used.

The actual meaning of scalability can be thought of as the network not having to consider all the other UEs or all APs while decoding a single UE. As the number of UEs or APs increases, this creates an exponential increase in CCP.

Due to simulation limitations, in Chapter 6, the employed network has $N = 36$, $K = 144$, $\bar{\mathcal{N}} = 9$ and $\bar{\mathcal{S}} = 4$ as typical values. These numbers do not result in a significant CCP difference between CFI-D and UCIS-D. However, with large networks such as the one in [8], where $N = 5000$ and $\bar{\mathcal{N}}$ is around 50, the reduction in CCP becomes astronomical. The simulation results in Chapter 6 show that even in a small network, UCIS-D is a valid method in terms of BER and AIR.

Finally, note that for $\bar{\mathcal{S}} = \bar{\mathcal{N}}D$, the matrix inversion sizes for feedforward and feedback filters are equal.

Table 5.1: Computational complexity of different detectors per UE.

	UCIS-D	**CFI-D**	**NW-MMSE**
Applying the Filters	$iT(\bar{\mathcal{N}}D + \bar{\mathcal{S}})$	$iT(ND + K)$	TND
CM/Inverse (4.18) and (4.32)	$i(\bar{\mathcal{N}}^2D^2\bar{\mathcal{S}} + \bar{\mathcal{N}}^3D^3) + \bar{\mathcal{N}}D$	$N^2D^2 + N^3D^3/K$	$N^2D^2 + N^3D^3/K$
Feedforward Filter	$iT(\bar{\mathcal{N}}^2D^2\bar{\mathcal{S}} + \bar{\mathcal{N}}D\bar{\mathcal{S}} + \bar{\mathcal{S}})$	$T(N^2D^2 + i(NDK + K))$	TN^2D^2
Feedback Filter	$iT(\bar{\mathcal{N}}D\bar{\mathcal{S}}^2 + \bar{\mathcal{S}}^3 + 2\bar{\mathcal{S}}^2 + \bar{\mathcal{S}})$	$iT(NDK + 2K^2 + 2K + 1)$	-
Reliability Matrix Calculation	$iT(\bar{\mathcal{N}}^2D^2 + 2\bar{\mathcal{N}}D + \bar{\mathcal{N}}D\bar{\mathcal{S}} + 4\bar{\mathcal{S}})$	$iT(N^2D^2 + 2ND + NDK + 4K)$	-
$\mathcal{S}_k$ grouping and PIC	$T[(2\bar{\mathcal{N}}D + \lvert\mathcal{M}_k\rvert) + i\bar{\mathcal{N}}D\lvert\mathcal{S}'_k\rvert]$	-	-
per UE Complexity	$\mathcal{O}(iT(\bar{\mathcal{N}}^2D^2\bar{\mathcal{S}} + \bar{\mathcal{N}}D\bar{\mathcal{S}}^2 + \bar{\mathcal{N}}D\lvert\mathcal{S}'_k\rvert + \bar{\mathcal{S}}^3) + i\bar{\mathcal{N}}^3D^3 + T\lvert\mathcal{M}_k\rvert)$	$\mathcal{O}(N^3D^3/K + TN^2D^2 + iT(NDK + K^2))$	$\mathcal{O}(N^3D^3/K + TN^2D^2)$

CHAPTER 6

SIMULATION RESULTS

6.1 Introduction

In this chapter, the performance of the proposed methods will be presented via simulation results. All of the simulations are done in the MATLAB 2022a environment. The Monte Carlo method is used for every network. More than 10^7 bits are transmitted by UEs for every plot across several network realizations and channel realizations (transmission blocks). The performance of the proposed MEB and the proposed CFI-D and UCIS-D methods are presented and compared with the current trends in the literature.

6.2 Simulation Setup

Some parameters used in the simulations are given in Table 6.1. Unless stated otherwise for a specific parameter, values in Table 6.1 are used. A dual-slope model for ω parameter like in [8] and the break-point distance is $d_{bp} = 100$ meters. In Table 6.1, path loss exponent values are given as $\omega = 2$ and $\omega = 4$ for distances smaller and greater than the break-point distance, respectively. This means that the large scale gain α_{kn} depends on the path loss exponent ω in the following way

$$\alpha_{kn}[\text{dB}] = \begin{cases} \text{P}_x - 61.4 - 20\log_{10}(d_{kn}) & \text{if } d_{kn} \leq d_{bp}. \\ \text{P}_x - 61.4 + 20\log_{10}(d_{bp}) - 40\log_{10}(d_{kn}) & \text{if } d_{kn} > d_{bp}. \end{cases} \tag{6.1}$$

The APs are put in a grid layout like in Fig. 2.1 with wrap-around [4] topology, and UEs are dropped uniformly and randomly in the area. After the number of MPCs is decided for every channel according to Table 6.1, the MPCs are scaled according

Table 6.1: Parameters Chosen for the Simulations

Description	Value
Network Area	500m×500m
Number of APs	$N = 36$
AP Height	2m
AP Receiver Noise Figure	7 dB
Path-loss Exponent	$\omega = 2$ (0-100m), $\omega = 4$ (100+m)
Angular Spread Density	$\sigma_\phi = 1^\circ$, $\sigma_\theta = 0^\circ$
Antenna and RF chain per AP	M =64 and D =4
Number of MPCs per Channel	Chosen randomly from $\{2, 3, 4\}$
Rician K-Factor	10dB(LoS MPC), 0dB(NLoS MPC)
Bandwidth and Noise Power	100MHz, -174dBm/Hz, N_0 =-94dBm
Block Length(FFT size)	T =64
Loading Percentage	$100K/(ND)$
QAM order	Z =4 uncoded

to Chapter 2.1.2.2. For each MPC, the parameter U_{knl} is drawn from the uniform distribution $U[0, 1]$ except one. That one MPC has the parameter $U_{knl} = 1$ fixed, representing the zero-delay line of sight (LOS) MPC with $l = 0$. The rest of the MPCs are assigned random delays between $l = 1$ and $l = 32$ ordered according to their U_{knl} parameters, the lower delay getting the higher parameter. The AoA of the zero-delay MPC is inferred from the location of the UEs and APs; the other MPCs are assumed to be arriving from random directions.

A new parameter called 'Ref SNR' is introduced, representing the transmit power adjustment. Ref SNR refers to the SNR value 50 meters away from a UE, including the noise figure of the receiver. The transmit power P_x is adjusted according to the Ref SNR value and α_{kn} given in Chapter 2.1.2.2. For example, Ref SNR being 15 dB corresponds to a transmit power of $P_x \approx 23.4$ dBm, which is in line with GSM mobile phone uplink transmit powers. All UEs are assumed to have the same transmit power. Finally, unless otherwise stated about E_T, perfect CSI ($E_T = \infty$) is assumed.

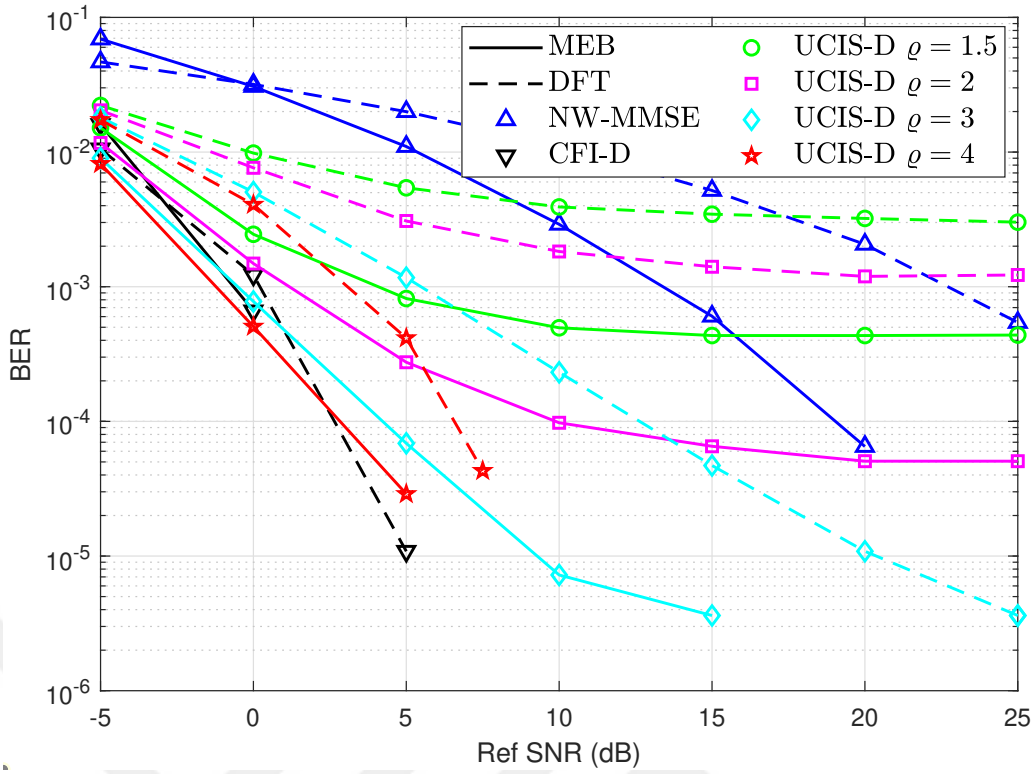

Figure 6.1: BER vs. Ref SNR performance of MEB and DFT analog beamformers with system parameters $\bar{\mathcal{N}} = 9$ and $\bar{\mathcal{S}} = 4$ under 100% loading ($K = 144$). The two methods are compared for NW- MMSE, CFI-D, and UCIS-D detectors with different ϱ values.

6.3 Results

In Figure 6.1, a comparison between MEB and DFT beamformer can be seen in the form of BER vs. Ref SNR performance for different detectors under 100% loading ($K = 144$). The parameters $\bar{\mathcal{N}} = 9$ and $\bar{\mathcal{S}} = 4$ is chosen along with several ϱ values for the UCIS-D. Note that parameter ϱ directly determines the magnitude of sparsification. Therefore, the CCP of UCIS-D depends greatly on ϱ. The case $\varrho = N/\bar{\mathcal{N}}$, which is 4 in this case, is also of importance since it means no sparsification and all the channels are being estimated. Figure 6.1 shows that MEB has superior performance compared to DFT beamformer in almost all cases. This is due to MEB illuminating all the served UEs while DFT can only illuminate at most D UEs. Since the point of CF/UC networks is boosting the performance of weaker UEs allowing uniform service, the MEB beamformer is conceptually suited for this application.

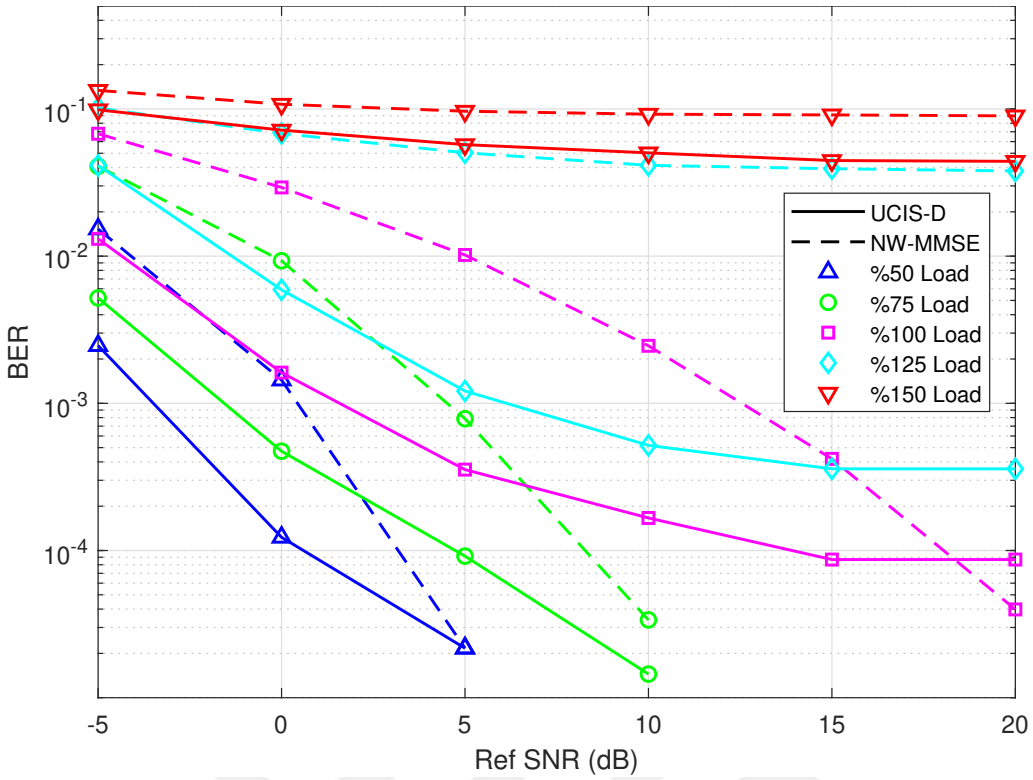

Figure 6.2: BER vs. Ref SNR performance of UCIS-D and CFI-D under different loads. UCIS-D parameters are $\bar{\mathcal{N}} = 9$, $\bar{\mathcal{S}} = 4$ and $\varrho = 2$.

Also, notice that as ϱ decreases, the error floor on the BER for UCIS-D increases. As sparsification increases, APs start to ignore more and more UEs. After a certain point, effective interferers may be ignored, raising the error floor. However, do note that the error floor is lower for MEB compared to the DFT beamformer. This is due to the ability of the detectors to serve UEs that were not illuminated by the DFT beamformer. Finally, even with $\varrho = 1.5$, MEB can achieve acceptable (BER$< 10^{-3}$) performance under $\%100$ loading.

For the rest of the simulation results, MEB is used for all detectors. For NW methods such as CFI-D and NW-MMSE, MEB is calculated assuming every AP serves every UE ($\mathcal{N}_k$ contains every AP for all UEs and $\mathcal{K}_n$ contains all UEs for every AP). Figure 6.2 compares the performance of UCIS-D ($\bar{\mathcal{N}} = 9$, $\bar{\mathcal{S}} = 4$ and $\varrho = 2$) and NW-MMSE under different loads. It can be seen that UCIS-D is much more robust in the face of increased load, especially at lower transmit power values (SNR). This is expected since, above 100% load, the NW-MMSE starts to have dimensionality

problems and cannot differentiate different UEs in the digital signal domain. One can see that UCIS-D can even handle 125% loading, even with low $\bar{\mathcal{S}}$ and ϱ values. Also, the limits of UCIS-D under given parameters can also be seen as the performance drops sharply at 150% loading. Figure 6.1 and Figure 6.2 together show that UCIS-D can offer great performance only if the parameters are chosen appropriately. The sparsification parameters ($\bar{\mathcal{N}}$ and ϱ) must be chosen with the loading percentage in mind to have acceptable performance with feasible CCP.

Also note that, due to simulation limitations, the given network is relatively small. However, even in a small and highly loaded network, UCIS-D offers a scalable operation with better performance compared to NW-MMSE. Figure 6.3 aims to show the effect of $\bar{\mathcal{S}}$ parameter on the UCIS-D BER vs. Ref SNR performance. For both Figure 6.3(a) and Figure 6.3(b), $\bar{\mathcal{N}} = 9$. In Figure 6.3(a), the other parameters are $\varrho = 2$ and 125% loading ($K = 180$). In Figure 6.3(b), the parameters are $\varrho = 3$ and 150% loading($K = 216$). Both figures show that the performance converges at very low $\bar{\mathcal{S}}$ values compared to K. In Figure 6.3(a), one can see that only $\bar{\mathcal{S}} = 4$ out of $K = 180$ UEs are needed. Increasing the $\bar{\mathcal{S}}$ further does not affect the performance. Similarly at Figure 6.3(b), only $\bar{\mathcal{S}} = 8$ out of $K = 216$ UEs are needed. This property points to a very important conclusion. Only a few serious interferers need to be processed with the computationally expensive IB-DFE method; the rest can be processed with PIC without causing a performance loss. This highlights the power of UC operation. Also, Figure 6.3(b) shows that, with lower sparsification (increasing ϱ), UCIS-D can even handle 150% loading with only $\bar{\mathcal{S}} = 8$. Since the feedback filter on the IB-DFE operation needs matrix inversions of size $\bar{\mathcal{S}} \times \bar{\mathcal{S}}$, Figure 6.3 shows UCIS-D being able to operate under heavy loads with a configuration which allows severely reduced CCP. Figure 6.4 focuses on the effects of the pilot sequence power E_T. Note that the channel estimation quality depends both on pilot sequence power and the Ref SNR value, as can be seen in (4.8) and (4.9). In Figure 6.4(a), the parameters are $\varrho = 2$, $\bar{\mathcal{S}} = 4$, 100% loading ($K = 144$) and Ref SNR is 15 dB. The BER vs. E_T (dB) is given for different $\bar{\mathcal{N}}$ values for UCIS-D along with the NW-MMSE. One can see that lowering the $\bar{\mathcal{N}}$ value leads to quicker convergence of the BER with respect to E_T. This is expected, since with lower $\bar{\mathcal{N}}$, the $\bar{\mathcal{K}}$ is also lower. This, in turn, means that APs estimate the channels of less number of UEs. Since channel estimation quality

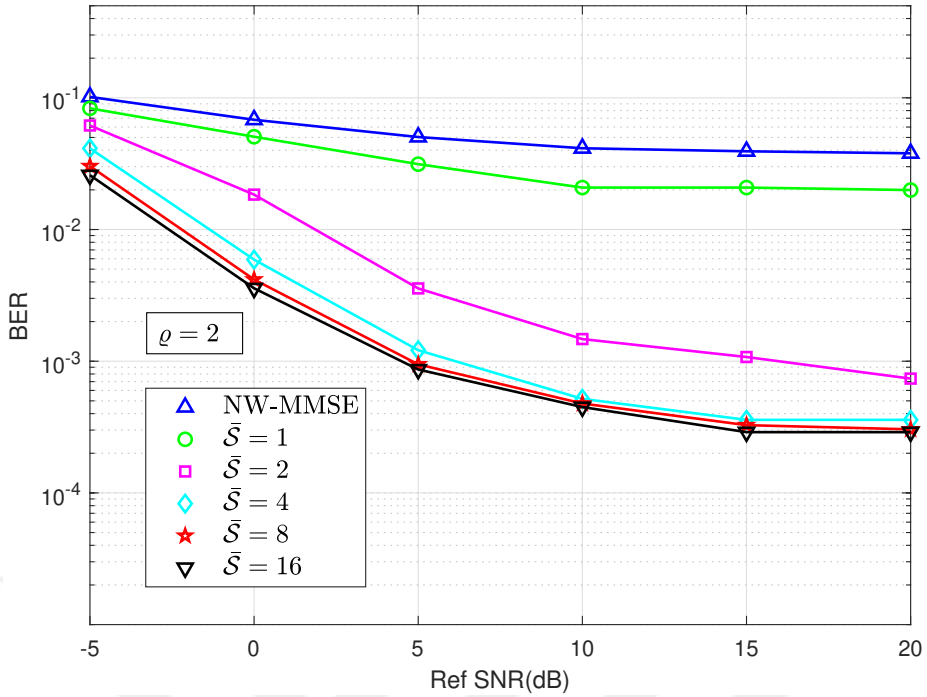

(a) $\bar{\mathcal{N}} = 9$, $\varrho = 2$ under 125% loading ($K = 180$).

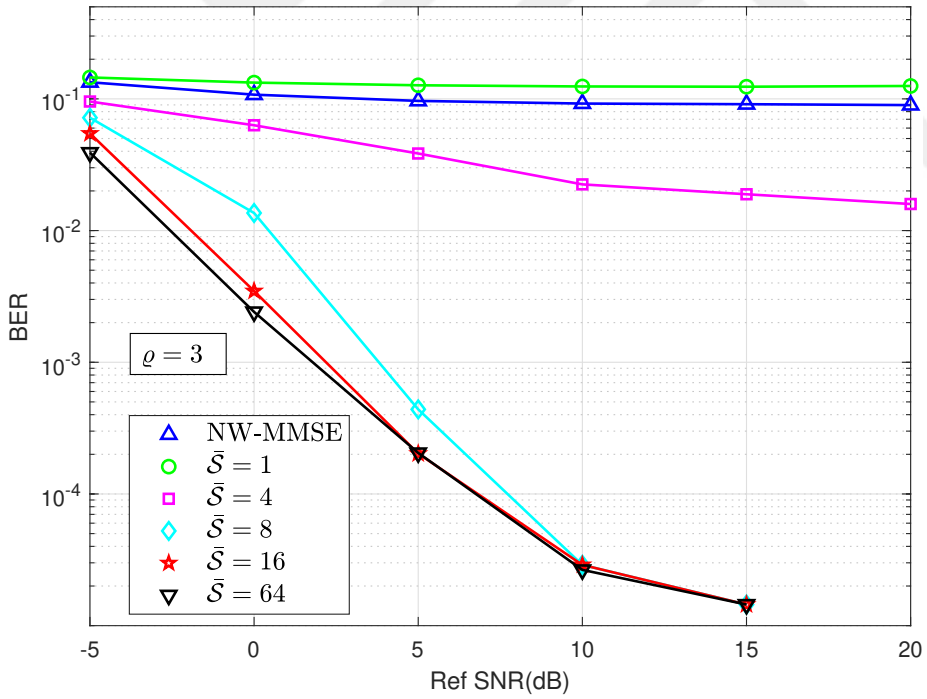

(b) $\bar{\mathcal{N}} = 9$, $\varrho = 3$ under 150% loading ($K = 216$).

Figure 6.3: The BER vs Ref SNR performance of UCIS-D with different $\bar{\mathcal{S}}$ values along with NW-MMSE.

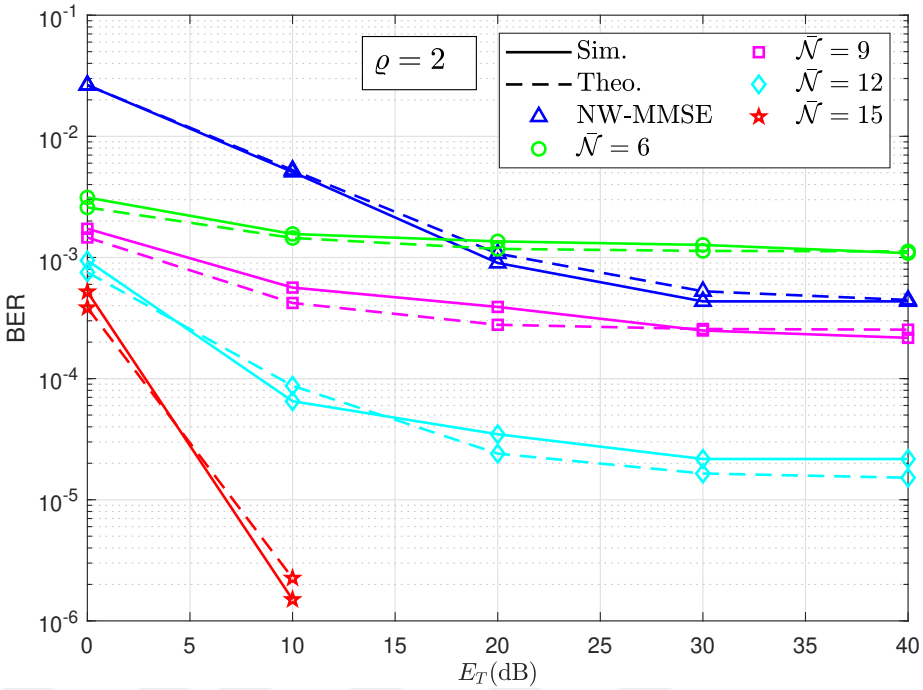

(a) BER vs E_T performance for UCIS-D for different $\bar{\mathcal{N}}$ values. Ref SNR is 15 dB.

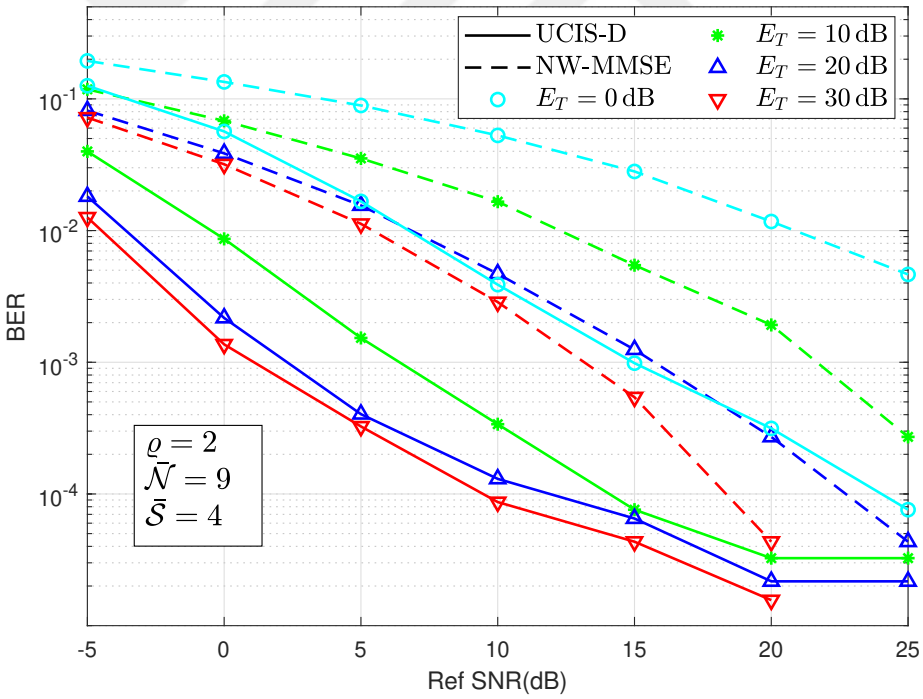

(b) The BER vs Ref SNR performance of UCIS-D for different E_T values with $\bar{\mathcal{N}} = 9$.

Figure 6.4: The effects of the pilot sequence power on the performance of UCIS-D and NW-MMSE. For both plots $\varrho = 2$, $\bar{\mathcal{S}} = 4$ and 100% loading ($K = 144$).

relies on both large-scale gain (α_{kn}) and pilot sequence power (E_T), the UEs with good channels get a good channel estimation even with low E_T values. NW-MMSE, on the other hand, relies greatly on E_T to function properly. Figure 6.4(a) shows that, with low $\bar{\mathcal{N}}$, the UC configuration will automatically lower the need for long pilot sequences. In Figure 6.4(b), the parameters are $\varrho = 2$, $\bar{\mathcal{S}} = 4$, 100% loading ($K = 144$) and $\bar{\mathcal{N}} = 9$. Figure 6.4(b) shows the BER vs. Ref SNR performance of UCIS-D and the NW-MMSE under different pilot sequence powers. Just like in Figure 6.4(a), UCIS-D performance relies less on the pilot sequence power. Even at high Ref SNR, NW-MMSE has very poor BER performance with low pilot sequence power, while UCIS-D almost converges at $E_T = 10$ dB for almost all Ref SNR values. Seeing the robustness of UCIS-D for different pilot sequence lengths for all Ref SNR values is an important aspect of Figure 6.4(b).

In some of the following plots, the BER of the same method is shown for two cases. One is the actual simulation BER performance given as "Sim.". The other one is the theoretical BER performance given as "Theo." which is calculated using (5.12) with the true SINR value given in (5.5). Details between these two BER metrics are explained in Chapter 5 in detail. This approach of showing both BER values allows us to see the reliability of the Gaussianity assumption on the interference term $\eta_k^{(i)}$, which was in (5.1) and (5.8). Two values being close to each other means that this assumption is valid, and the SINR value the detector uses in (5.10) to calculate the soft decisions and reliability matrices is acceptable. The following results will show that the two values are indeed close for almost all cases, proving the validity of the Gaussianity assumption.

Figure 6.6 and Figure 6.5 show the overall BER performance of the UCIS-D compared to the NW-MMSE and CFI-D. The performance is given for different $\bar{\mathcal{N}}$ values. For all subplots, $\varrho = 2$ is chosen to present a heavily sparsified and low-CCP implementation. For all subplots of Figure 6.6 and Figure 6.5, we have $\bar{\mathcal{S}} = 4$ except for Figure 6.6(b) where we have $\bar{\mathcal{S}} = 36$ instead. The loading percentages are 75% ($K = 108$), 100% ($K = 144$), 125% ($K = 180$), and 150% ($K = 216$) for Figure 6.5(a), Figure 6.5(b), Figure 6.6(a) and Figure 6.6(b) respectively. Assuming a BER value of 10^{-3} for un-coded transmission provides adequate performance, Figure 6.6 and Figure 6.5 show that UCIS-D can handle ultra-high loads with comparatively

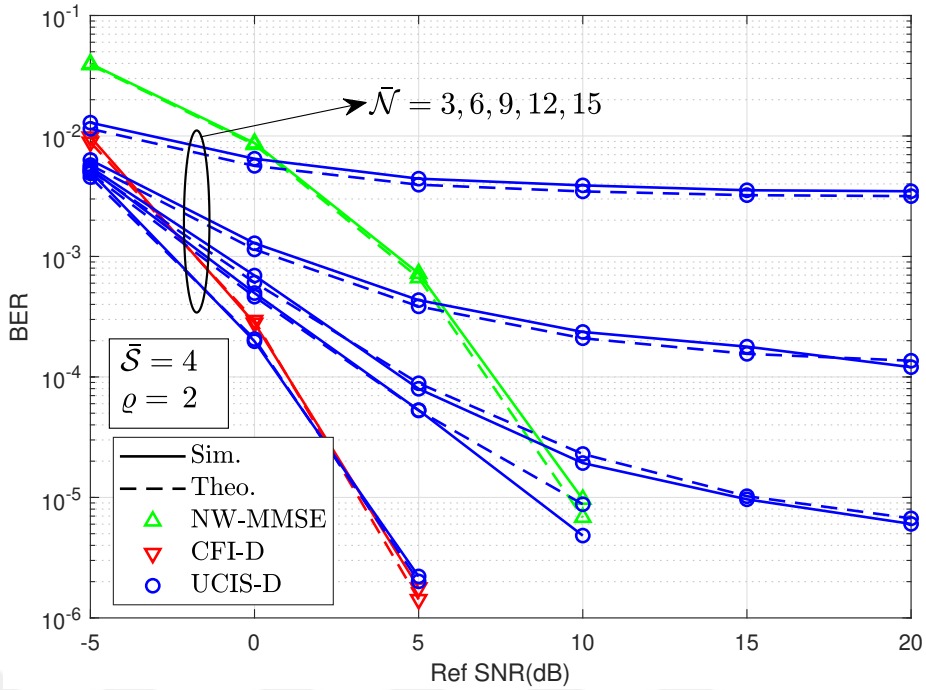

(a) $\bar{\mathcal{S}} = 4$ and 75% ($K = 108$).

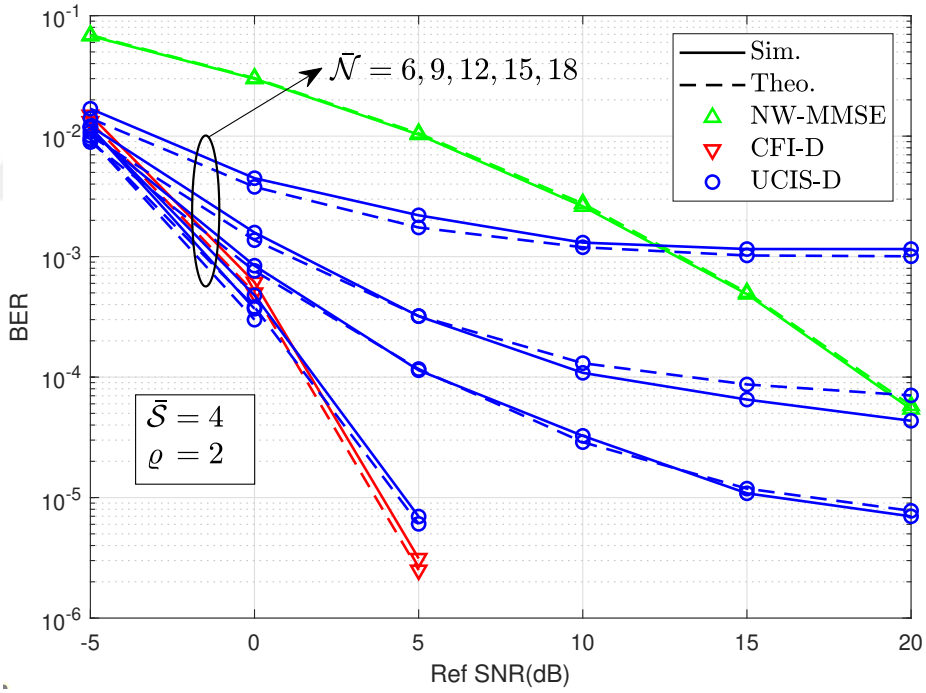

(b) $\bar{\mathcal{S}} = 4$ and 100% ($K = 144$).

Figure 6.5: The BER vs. Ref SNR performance of NW-MMSE, CFI-D, and the UCIS-D different $\bar{\mathcal{N}}$. For both plots $\varrho = 2$.

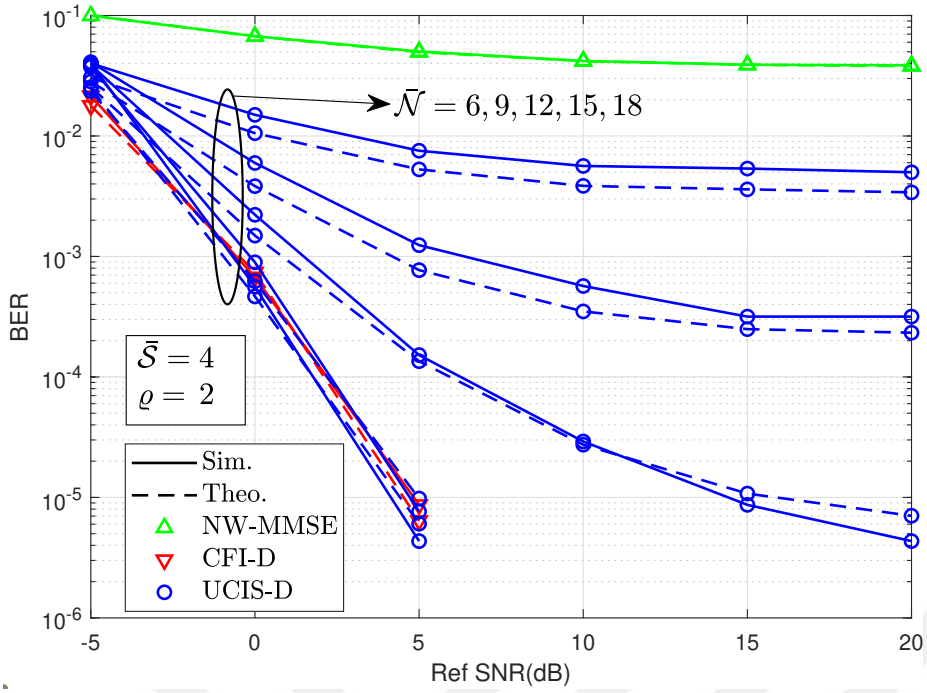

(a) $\bar{\mathcal{S}} = 4$ and 125% ($K = 180$).

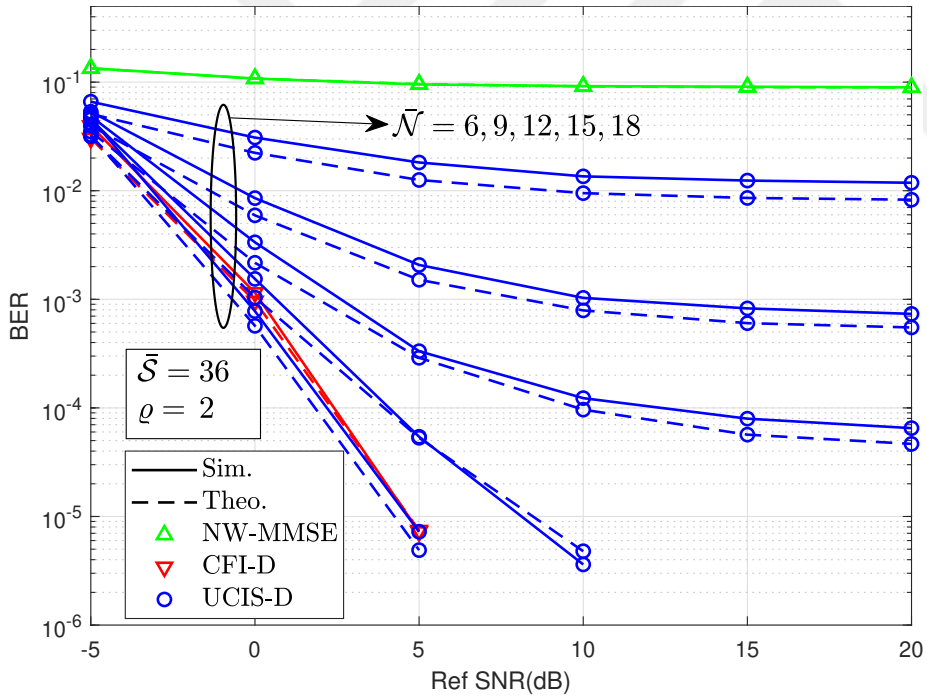

(b) $\bar{\mathcal{S}} = 36$ and 150% ($K = 216$).

Figure 6.6: The BER vs. Ref SNR performance of NW-MMSE, CFI-D, and the UCIS-D different $\bar{\mathcal{N}}$. For both plots $\varrho = 2$.

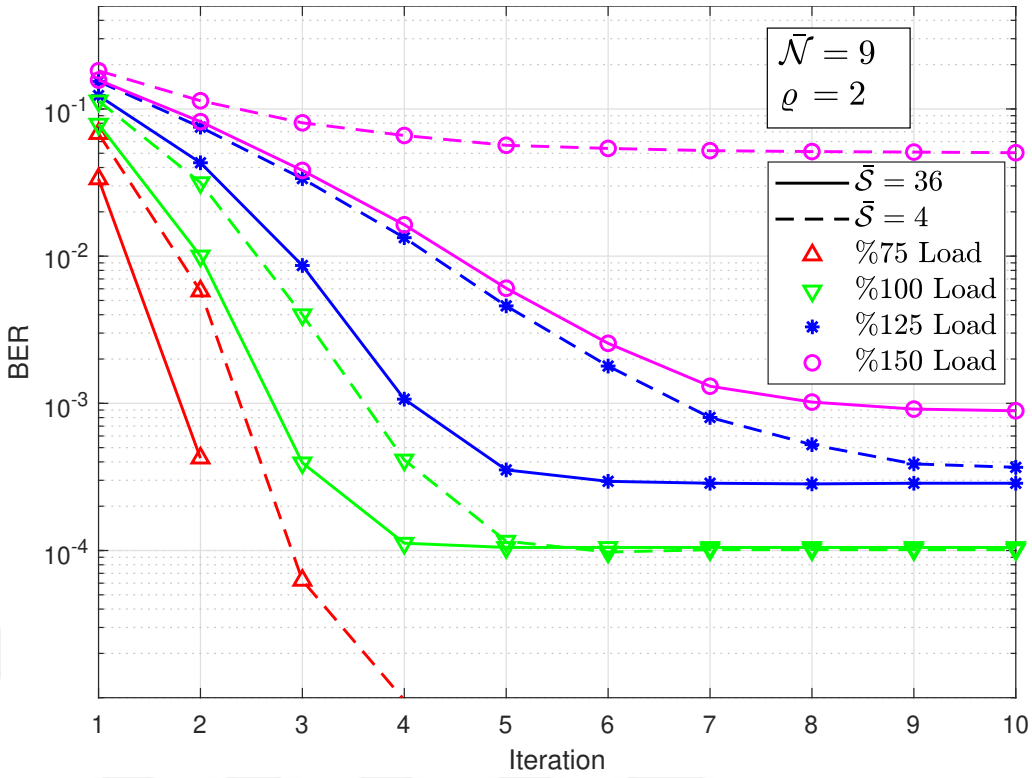

Figure 6.7: BER of UCIS-D for number of iterations for different $\bar{\mathcal{S}}$ values. $\bar{\mathcal{N}} = 9$ and $\varrho = 2$.

low $\bar{\mathcal{N}}$ values. It can be seen that CFI-D is a benchmark, and it can handle these ultra-high loads with relative ease even at low transmit powers. One can see that to reach the performance of CFI-D, almost half of the APs must be deployed for a single UE. At very low Ref SNRs, sometimes UCIS-D outperforms CFI-D. This is expected since CFI-D minimizes the MSE and does not employ a maximum likelihood method. Since at very low transmit powers, a higher number of UEs that are far from an AP will be below the noise power. They, in turn, will decrease performance instead of increasing it. The NW-MMSE method, on the other hand, can not handle these high loads. It needs a very high Ref SNR to operate properly as the load increases, and anything above 100% loading breaks the method completely due to mentioned dimensionality problems. Figure 6.6 and Figure 6.5 show that ultra-high loads can be handled in a UC mMIMO network in a scalable manner. Figure 6.7 focuses on the number of iterations needed for convergence in the UCIS-D. A number of iterations directly affects the CCP of any iterative method since most of the actions are repeated at every iteration. BER vs. the number of iterations is given with the parameters

$\varrho = 2, \bar{\mathcal{N}} = 9$. The performance is given for both $\bar{\mathcal{S}} = 4$ and $\bar{\mathcal{S}} = 9$ under different loading percentages. It is obvious that more iterations are needed for convergence as the number of UEs in the network increase. Also, more iterations are also needed for convergence when UCIS-D operates under a lower $\bar{\mathcal{S}}$ value. However, the number of iterations needed for convergence does not exceed 10 in any case; this means that the UCIS-D does not need many iterations under any scenario, which guarantees a low CCP implementation. Also note that, for ultra-high loads (150% for example), $\bar{\mathcal{S}}$ needed for acceptable performance (BER lower than 10^{-3}) also increases; however, the increased $\bar{\mathcal{S}}$ is still much smaller than the number of UEs K.

All the figures up to now show the BER performance of the mentioned detectors. However, these BER values are given for un-coded transmissions. To see the actual capacity of the system is also important to not get misleading results and discard some practical configurations as a consequence. To this end, Figure 6.8 and Figure 6.9 focus on the AIR vs. Ref SNR performance for different scenarios where the AIR metric has a unit of bits per symbol per Hertz (bps/Hz). The results are given under both perfect CSI and for pilot sequence power of $E_T = 10$ dB. The UCIS-D performance is also given for both $\bar{\mathcal{S}} = 4$ and $\bar{\mathcal{S}} = 36$. In Figure 6.8(a), the parameters are $\varrho = 2$, $\bar{\mathcal{N}} = 9$ the QAM order is $Z = 4$ and loading is 150% ($K = 216$). In Figure 6.8(b), the parameters are $\varrho = 2$, $\bar{\mathcal{N}} = 9$ the QAM order is $Z = 16$ and loading is 100% ($K = 144$). In Figure 6.9(a), the parameters are $\varrho = 3$, $\bar{\mathcal{N}} = 9$ the QAM order is $Z = 64$ and loading is 75% ($K = 108$). In Figure 6.9(b), the parameters are $\varrho = 3$, $\bar{\mathcal{N}} = 9$ the QAM order is $Z = 256$ and loading is 50% ($K = 72$). In addition to CFI-D and NW-MMSE Detector, the performance of the Subset MMSE method present in [8] is also given; note that it is adapted to the frequency domain implementation. The Subset MMSE method can be thought of as the first iteration of UCIS-D, and it is also scalable. It can be seen that UCIS-D can reach the maximum possible rate (due to finite constellations) in all scenarios. UCIS-D also outperforms NW-MMSE under smaller constellations and heavier loads. The Subset MMSE method [8], on the other hand, performs poorly in all scenarios due to suffering from both dimensionality and no iterative interference cancellation. CFI-D also reaches the maximum rate in every scenario. However, it needs higher ref SNR as the constellation grows in size as expected. Finally, one can see that NW-MMSE with coding can perform adequately

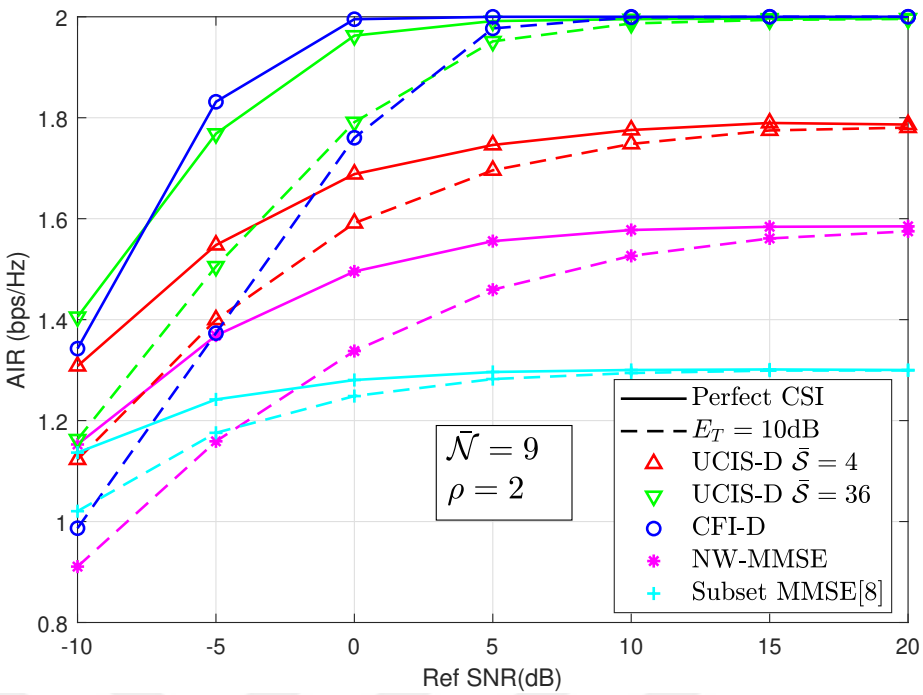

(a) 4-QAM, $\varrho = 2$ and loading 150% ($K = 216$).

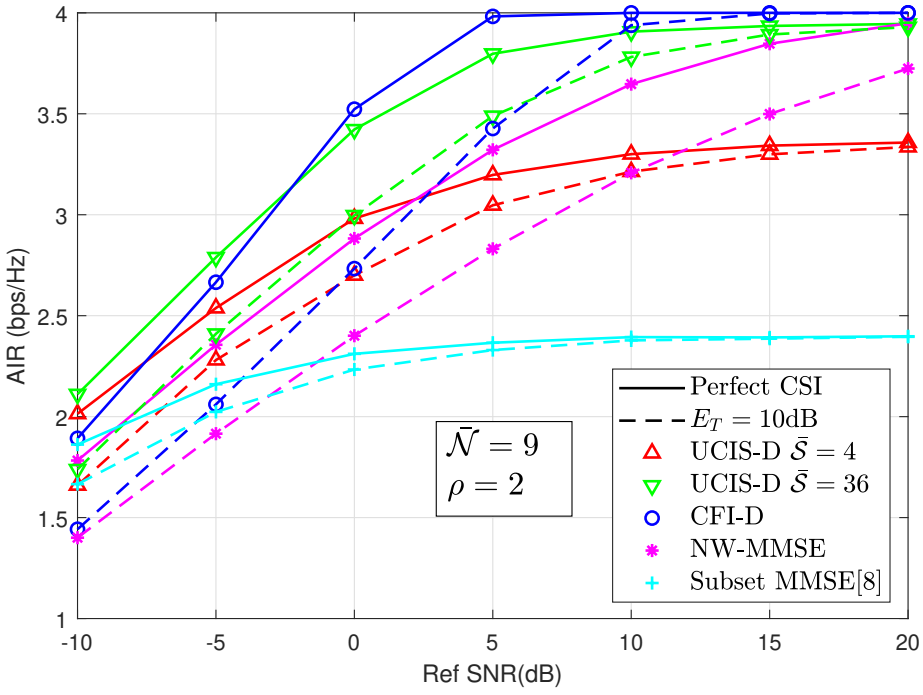

(b) 16-QAM, $\varrho = 2$ and loading 100% ($K = 144$).

Figure 6.8: AIR vs. Ref SNR for NW-MMSE, CFI-D, Subset MMSE Detector [8] and the UCIS-D for perfect and imperfect CSI. UCIS-D is plotted with $\bar{\mathcal{S}} = 4$ and $\bar{\mathcal{S}} = 36$. $\bar{\mathcal{N}} = 9$ for all plots.

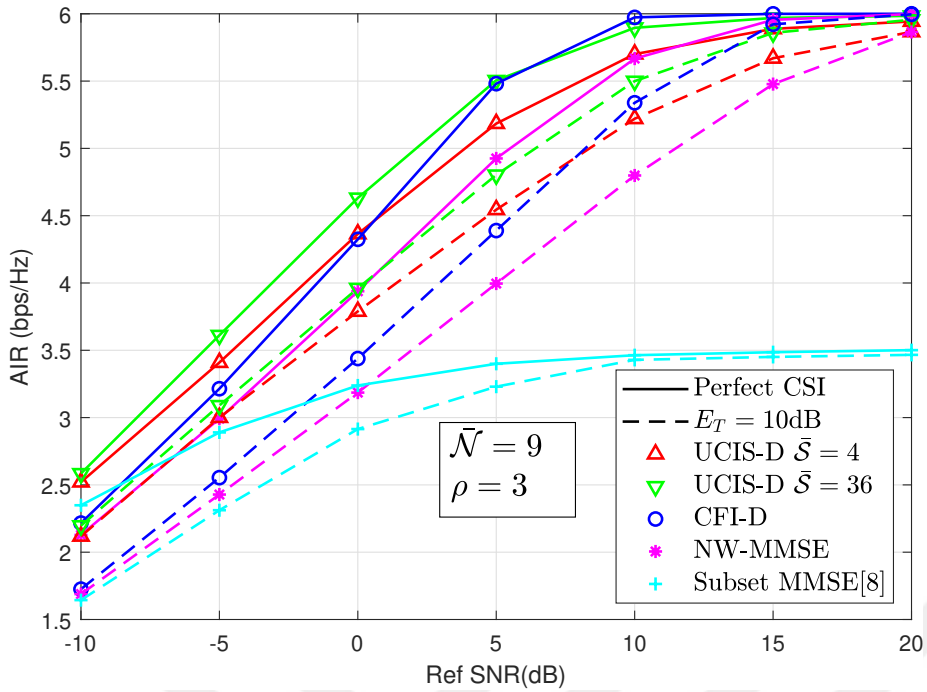

(a) 64-QAM, $\varrho = 3$ and loading 75% ($K = 108$).

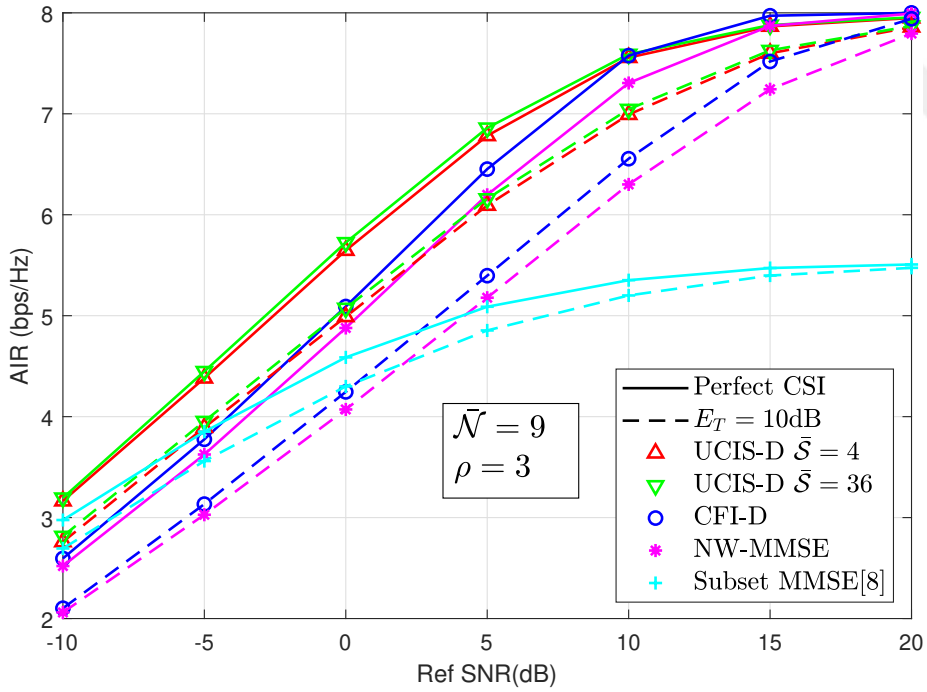

(b) 256-QAM, $\varrho = 3$ and loading 50% ($K = 72$).

Figure 6.9: AIR vs. Ref SNR for NW-MMSE Detector, NW Detector, Subset MMSE Detector [8] and the UCIS-D for perfect and imperfect CSI. UCIS-D is plotted with $\bar{\mathcal{S}} = 4$ and $\bar{\mathcal{S}} = 36$. $\bar{\mathcal{N}} = 9$ for all plots.

with higher constellations. Though, note that it is still an unscalable method and less robust against channel estimation errors. An important result that can be inferred from Figure 6.8 and Figure 6.9 is that the performance of UCIS-D is affected by the constellation size greatly. Sparsification parameters ϱ and $\bar{\mathcal{N}}$, and also the UE interference group parameter $\bar{\mathcal{S}}$ has strict constrictions on them to provide adequate performance under large constellation sizes.

CHAPTER 7

CONCLUSIONS AND FUTURE WORKS

7.1 Conclusions

This thesis proposes a novel uplink hybrid beamforming receiver structure for a UC mMIMO network operating under mmWave frequencies. First, in Chapter 2, a system model and a Rician channel model is introduced. The model incorporates the frequency selective, sparse (both in temporal and spatial domains) nature of mmWave channels. An SC-FDE structure is used instead of an OFDM-type modulation for the modulation scheme due to SC-FDE structures having more desirable properties in the uplink, such as peak-to-average-power-ratio, quantization and robustness against carrier-frequency offset.

The first stage of a hybrid beamformer is the AB stage, which is given in Chapter 3 within this thesis. The AB stage can be implemented using phase shifters and attenuators (only phase shifters in some systems). AB is performed before the ADC operation, so it does not need any digital signal processing. Since mmWave systems can fit a very high number of antennas in an antenna array, the AB stage is important to reduce the dimension of the received signal. This, in turn, allows the system to operate with a lower number of RF chains, decreasing the infrastructure cost greatly. Four AB methods were introduced and explained. Three of them, namely the DFT beamformer, EB, and GEB are already present in the literature and are widely known. The fourth one is the MEB, and it is the proposed AB method in this thesis. Every method has its advantages and disadvantages. However, it is explained that MEB is a very suitable AB method for CF/UC mMIMO networks due to its nature. MEB provides a trend of fairness among the served UEs, which in turn aligns with the

uniform service goal of CF/UC networks. Promoting uniform service and being able to accommodate many UEs, MEB has shown to be a very fitting method for a given network topology.

Following the analog stage, in Chapter 4, the details of the digital stage are given. First, the novel CFI-D detector is given. CFI-D is the implementation of the IB-DFE structure for CF mMIMO systems. IB-DFE structure relies on an iterative interference cancellation structure, utilizing frequency domain decision feedback via soft decisions made by the detector. Although CFI-D offers great performance, it has very high CCP, and it is unscalable due to every AP in the network serving every UE. This property is the main motivation behind the UCIS-D.

UCIS-D is the main contribution of this thesis. It is an alternative detector to CFI-D, offering lower but acceptable performance with a lower CCP, and it is scalable. First, the algorithm for deciding which AP serves which UEs is given (under the name of Subset Grouping) as a start, and new UC entities are defined for every UE. The row decimation and column sparsification procedures are introduced to define these UC entities to enable the desired operation. Next, the structure of UCIS-D is introduced. UCIS-D relies on a PIC-aided IB-DFE structure. In a large network, a UE has good channels to only a group of APs. In addition, most of the other UEs (interferers) have bad channels to the mentioned group of APs. Therefore, performing interference cancellation to all interferers with the costly IB-DFE operation is not feasible. UCIS-D groups the interfering UEs into three groups. Only the strongest interferers are canceled with the IB-DFE, while the weaker interferers are canceled with PIC. The weakest interferers are ignored since they are likely to be below the noise level. This partitioning lowers the CCP greatly while still offering acceptable performance.

In Chapter 5, the performance metrics are introduced. Using Bussgang Decomposition, an SINR value that depends on digital filters and soft decisions is introduced. How the system uses this SINR value and how the soft decisions are calculated are also provided. Finally, the AIR metric is defined as an SE alternative providing a lower bound on the mismatch decoding capacity under finite QAM constellations.

The simulation results are given in Chapter 6. Through simulations done in MATLAB environment, the BER and AIR performance of UCIS-D, CFI-D, and NW-MMSE

methods are illustrated. The results show that UCIS-D can actually offer practical performance under very heavy loads in a scalable manner. It has been shown that the idea of only processing the strongest interferers with CCP-heavy methods is indeed practical and feasible. It has also been shown that UCIS-D does not require long piloting sequences due to its UC nature. Finally, for both UCIS-D and CFI-D, one can see that not many iterations are needed to achieve convergence in the performance.

Most of the literature on CF/UC mMIMO generally assumes $N >> K$, and some assume $N > K$. This leads to usually investigating lightly loaded systems. However, simulation results show that UCIS-D proposed in this work can handle ultra-high loads with adequate performance. UCIS-D also outperforms the unscalable NW-MMSE as a scalable alternative which is the prime method for CF networks in the current literature.

7.2 Future Works

Although this work introduces a large framework with a lot of components, there are still many gaps that need to be considered and explored in a practical implementation. The author aims to expand the work done on this thesis in several aspects in the future. These issues can be listed as follows:

- The CCMs of the channels are assumed to be known by the detector. An estimation process for these matrices is planned to be integrated.
- The fronthaul link between the APs and the CPU is assumed to be ideal. The network is planned to be investigated under a finite capacity and a delayed fronthaul link.
- The uplink signals from the UEs are assumed to be synchronized. A synchronization structure and the related error mechanism are planned to be introduced.
- Shadowing and mobility effects on the channels are ignored. They are planned to be integrated into the channel model.
- Hardware impairments are ignored. Only the noise figure of the receivers of APs is considered. Other hardware impairments are planned to be integrated.

- Quantization procedures for the digital filtering operations are planned to be integrated.

REFERENCES

[1] N. Bhushan, J. Li, D. Malladi, R. Gilmore, D. Brenner, A. Damnjanovic, R. T. Sukhavasi, C. P. and S. Geirhofer, "Network densification: The dominant theme for wireless evolution into 5G," *IEEE Commun. Mag.*, vol. 52, no. 2, pp. 82–89, Feb. 2014.

[2] H. Q. Ngo, A. Ashikhmin, H. Yang, E. G. Larsson, and T. L. Marzetta, "Cell-free massive MIMO versus small cells," *IEEE Trans.Wireless Commun.*, vol. 16, no. 3, pp. 1834–1850, Mar. 2017.

[3] H. Q. Ngo, A. Ashikhmin, H. Yang, E. G. Larsson and T. L. Marzetta, "Cell-Free Massive MIMO: Uniformly great service for everyone," in *Proc. IEEE 16th Int. Workshop Signal Process. Adv. Wireless Commun. (SPAWC)*, 2015, pp. 201-205.

[4] Ö. T. Demir, E. Björnson, L. Sanguinetti, "Foundations of User-Centric Cell-Free Massive MIMO," *Found. Trends Signal Proces.*, vol. 14, nos. 3-4, pp. 162-472, 2021.

[5] E. Björnson and L. Sanguinetti, "Making cell-free massive MIMO competitive with MMSE processing and centralized implementation," *IEEE Trans. Wireless Commun.*, vol. 19, no. 1, pp. 77–90, Jan. 2020.

[6] S. Buzzi and C. D'Andrea, "User-centric communications versus cell-free massive MIMO for 5G cellular networks," in *Proc. 21st International ITG Workshop on Smart Antennas*, 2017.

[7] E. Björnson and L. Sanguinetti, "Scalable cell-free massive MIMO systems," *IEEE Trans. Commun.*, vol. 68, no. 7, pp. 4247–4261, Jul. 2020

[8] M. Attarifar, A. Abbasfar, and A. Lozano, "Subset MMSE receivers for cell-free networks," *IEEE Trans. Wireless Commun.*, vol. 19, no. 6, pp. 4183–4194, June 20

[9] T. S. Rappaport, S. Sun, R. Mayzus, H. Zhao, Y. Azar, K. Wang, G. N. Wong, J. K. Schulz, M. Samimi and F. Guiterrez, "Millimeter wave mobile communications for 5G cellular: It will work!" *IEEE Access*, vol. 1, pp. 335–349, 2013.

[10] J. Li, D.-W. Yue, and Y. Sun, "Performance analysis of millimeter wave massive MIMO systems in centralized and distributed schemes," *IEEE Access*, vol. 6, pp. 75482–75494, 2018.

[11] M. Alonzo and S. Buzzi, "Cell-free and user-centric massive MIMO at millimeter wave frequencies," in *Proc. IEEE Annu. Int. Symp. Personal, Indoor, Mobile Radio Commun.*, 2017, pp. 1–5.

[12] G. Femenias and F. Riera-Palou, "Cell-free millimeter-wave massive MIMO systems with limited fronthaul capacity," *IEEE Access*, vol. 7, no. 1, pp. 44596-44612, Apr. 2019.

[13] N. T. Nguyen, K. Lee, and H. Dai, "Hybrid beamforming and adaptive RF chain activation for uplink cell-free millimeter-wave massive MIMO systems," *IEEE Trans. Veh. Technol.*, vol. 71, no. 8, pp. 8739–8755, Aug. 2022.

[14] A. A. Avidh, Y. Sambo, S. Ansari, and M. A. Imran, "Hybrid beamforming with fixed phase shifters for uplink cell-free millimetrewave massive MIMO systems," in *Proc. Joint Eur. Conf. Netw. Commun. & 6G Summit (EuCNC/6G Summit)*, pp. 19-24, Jun. 2021.

[15] C. Feng, W. Shen, J. An and L. Hanzo, "Weighted sum rate maximization of the mmWave cell-free MIMO downlink relying on hybrid precoding," *IEEE Trans. Wirel. Commun.* vol. 21, no. 4, pp. 2547-25-60, Apr. 2021.

[16] A. Pitarokoilis, S. K. Mohammed, and E. G. Larsson, "On the optimality of single-carrier transmission in large-scale antenna systems," *IEEEWireless Commun. Lett.*, vol. 1, no. 4, pp. 276-279, Aug. 2012.

[17] X. Song, S. Haghighatshoar, and G. Caire, "Efficient beam alignment for millimeter wave single-carrier systems with hybrid MIMO transceivers," *IEEE Trans. Wireless Commun.*, vol. 18, no. 3, pp. 1518-1533, Mar. 2019.

[18] G. M. Guvensen and E. Ayanoglu, “A generalized framework on beamformer design and CSI acquisition for single-carrier massive MIMO systems in millimeter wave channels,” in *Proc. IEEE Globecom Workshops (GC Wkshps)*, Dec. 2016, pp. 1-7.

[19] N. J. Myers and R. W. Heath, Jr., “Message passing-based joint CFO and channel estimation in mmWave systems with one-bit ADCs,” *IEEE Trans. Wireless Commun.*, vol. 18, no. 6, pp. 3064-3077, Jun. 2019.

[20] H. G. Myung, J. Lim, and D. J. Goodman, “Peak-to-average power ratio of single carrier FDMA signals with pulse shaping,” in *Proc. IEEE 17th Int. Symp. Pers., Indoor Mobile Radio Commun.*, Oct. 2006, pp. 1-5.

[21] F. Pancaldi, G. M. Vitetta, R. Kalbasi, N. Al-Dhahir, M. Uysal, and H. Mheidat, “Single-carrier frequency domain equalization,” *IEEE Signal Process. Mag.*, vol. 25, no. 5, pp. 37-56, Sep. 2008.

[22] R. Mosayebi, M. M. Mojahedian, and A. Lozano, “Linear Interference Cancellation for the Cell-Free C-RAN Uplink,” *IEEE Trans. Commun.*, vol. 20, no. 3, pp. 1544–1556, 2021.

[23] Kassam J., Castanheira D., Silva A., Dinis R., Gameiro A. “Distributed hybrid equalization for cooperative millimeter-wave cell-free massive MIMO,” *IEEE Trans. Commun.*, vol. 70, no. 8, pp. 5300-5316, Aug. 2022.

[24] T. K. Nguyen, H. H. Nguyen, and H. D. Tuan, “Adaptive successive interference cancellation in cell-free massive MIMO-NOMA,” in *Proc. IEEE 92nd Veh. Technol. Conf.*, pp. 1-5, Dec. 2020.

[25] Z. Wang, M. Li, R. Liu and Q. Liu, "Joint User Association and Hybrid Beamforming Designs for Cell-Free mmWave MIMO Communications," *IEEE Trans. Commun.*, vol. 70, no. 11, pp. 7307-7321, Nov. 2022.

[26] M. Alonzo, S. Buzzi, A. Zappone and C. D’Elia, "Energy-Efficient Power Control in Cell-Free and User-Centric Massive MIMO at Millimeter Wave," *IEEE Trans. Green Commun. Netw.*, vol. 3, no. 3, pp. 651-663, Sept. 2019.

[27] Y. Zhang, L. Xiao and T. Jiang, "Cloud-Based Cell-Free Massive MIMO Systems: Uplink Error Probability Analysis and Near-Optimal Detector Design," *IEEE Trans. Commun.*, vol. 70, no. 2, pp. 797-809, Feb. 2022.

[28] M. Guenach, A. A. Gorji and A. Bourdoux, "Joint Power Control and Access Point Scheduling in Fronthaul-Constrained Uplink Cell-Free Massive MIMO Systems," *IEEE Trans. Commun.*, vol. 69, no. 4, pp. 2709-2722, April 2021.

[29] A. Liu and V. K. N. Lau, "Joint BS-User Association, Power Allocation, and User-Side Interference Cancellation in Cell-free Heterogeneous Networks," *IEEE Trans. Signal Process.*, vol. 65, no. 2, pp. 335-345, 15 Jan.15, 2017.

[30] P. Liu, K. Luo, D. Chen and T. Jiang, "Spectral Efficiency Analysis of Cell-Free Massive MIMO Systems With Zero-Forcing Detector," *IEEE Trans. Commun.*, vol. 19, no. 2, pp. 795-807, Feb. 2020.

[31] H. Q. Ngo, L. -N. Tran, T. Q. Duong, M. Matthaiou and E. G. Larsson, "On the Total Energy Efficiency of Cell-Free Massive MIMO," *IEEE Trans. Green Commun. Netw.*, vol. 2, no. 1, pp. 25-39, March 2018.

[32] M. Bashar, K. Cumanan, A. G. Burr, H. Q. Ngo, E. G. Larsson, and P. Xiao, “Energy efficiency of the cell-free massive MIMO uplink with optimal uniform quantization,” *IEEE Trans. Green Commun. Netw.*, vol. 3, no. 4, pp. 971–987, Dec. 2019.

[33] T. Van Chien, E. Bjornson, and E. G. Larsson, “Joint power allocation and load balancing optimization for energy-efficient cell-free massive MIMO networks,” *IEEE Trans. Wireless Commun.*, vol. 19, no. 10, pp. 6798–6812, Oct. 2020.

[34] M. Bashar, K. Cumanan, A. G. Burr, M. Debbah, and H. Q. Ngo, “On the uplink max-min SINR of cell-free massive MIMO systems,” *IEEE Trans. Wireless Commun.*, vol. 18, no. 4, pp. 2021–2036, Apr. 2019.

[35] J. Kassam, D. Castanheira, A. Silva, R. Dinis and A. Gameiro, "Centralized Hybrid Equalization for Cell Free mMIMO mmWave based Systems," *13th Int. Symp. on Commun. Systems Netw. and Digital Signal Process. (CSNDSP)*, Porto, Portugal, 2022, pp. 727-731.

[36] J. Brun, V. Palhares, G. Marti and C. Studer, "Beam Alignment for the Cell-Free mmWave Massive MU-MIMO Uplink," *IEEE Workshop on Signal Process. Systems (SiPS)*, 2022, pp. 1-6

[37] B. Zhong, X. Zhu and E. G. Lim, "Clustering-based Pilot Assignment for User-Centric Cell-Free mmWave Massive MIMO Systems," *IEEE 96th Veh. Technol. Conf. (VTC-Fall)*, 2022, pp. 1-5

[38] S.-E. Hong, "Comparison study of RF beamforming schemes in hybrid precoding for cell-free mmWave massive MIMO UDN system," *Proc. IEEE 92nd Veh. Technol. Conf. (VTC-Fall)*, Nov. 2020, pp. 1–5.

[39] I. Kanno, M. Ito, T. Ohseki, K. Yamazaki, Y. Kishi, T. Choi, W. Chen and A. F. Molisch, "Fronthaul Load-Reduced Scalable Cell-Free massive MIMO by Uplink Hybrid Signal Processing," *IEEE 95th Veh. Technol. Conf. (VTC-Spring)*, 2022, pp. 1-5.

[40] Z. Wang, R. Liu, H. Li, M. Li, and Q. Liu, "Hybrid beamforming design for C-RAN based mm Wave cell-free systems," *Proc. IEEE Veh. Technol. Conf. (VTC)*, pp. 1-5, Nov. 2020.

[41] Y. Zhong, Y. Cao and T. Lv, "Low-Complexity Distributed Precoding in User-Centric Cell-Free mmWave MIMO Systems," *Wirel. Telecommun. Symp.*, 2022, pp. 1-5.

[42] A. Al Ayidh, Y. Sambo, S. Ansari and M. A. Imran, "Low-Complexity RF Chains Activation Based on Hungarian Algorithm for Uplink Cell-Free Millimetre-Wave Massive MIMO Systems," in *Proc. 33rd Annu. Int. Symp. Pers., Indoor and Mobile Radio Communications (PIMRC)*,Sep. 2022, pp. 529-534.

[43] Y. Al-Eryani and E. Hossain, "Self-organizing mmWave MIMO cell-free networks with hybrid beamforming: A hierarchical DRL-based design," *IEEE Trans. Commun.*, vol. 70, no. 5, pp. 3169–3185, May 2022.

[44] W. Jiang, B. Han, M. A. Habibi, and H. D. Schotten, "The road towards 6G: A comprehensive survey," *IEEE Open J. Commun. Soc.*, vol. 2, pp. 334–366, Feb. 2021.

[45] W. Jiang and H. D. Schotten, "Cell-free massive MIMO-OFDM transmission over frequency-selective fading channels", *IEEE Commun. Lett.*, vol. 25, no. 8, pp. 2718-2722, Aug. 2021.

[46] G. M. Guvensen and A. O. Yilmaz, "A general framework for optimum iterative blockwise equalization of single carrier MIMO systems and asymptotic performance analysis," *IEEE Trans. Commun.*, vol. 61, no. 2, pp. 609-619, Feb. 2013.

[47] N. Ghiasi, S. Mashhadi, S. Farahmand, S. M. Razavizadeh, and I. Lee, "Energy efficient AP selection for cell-free massive MIMO systems: Deep reinforcement learning approach," *IEEE Trans. Green Commun. Netw.*, early access, Aug. 3, 2022.

[48] P. Wang, M. Pajovic, P. V. Orlik, T. Koike-Akino, K. J. Kim, and J. Fang, "Sparse channel estimation in millimeter wave communications: Exploiting joint AoD-AoA angular spread," in *Proc. IEEE Int. Conf. Commun.* (ICC), May 2017, pp. 1–6.

[49] M. Bayraktar and G. M. Guvensen, "An Efficient Interference-Aware Constrained Massive MIMO Beamforming for mm-Wave JSDM," *IEEE Access*, vol. 9, pp. 87877-87897, 2021.

[50] A. Liu and V. Lau, "Phase only RF precoding for massive MIMO systems with limited RF chains," *IEEE Trans. Signal Process.*, vol. 62, no. 17, pp. 4505-4515, Sep. 2014.

[51] J. Choi, G. Lee, and B. L. Evans, "Two-stage analog combining in hybrid beamforming systems with low-resolution ADCs," *IEEE Trans. Signal Process.*, vol. 67, no. 9, pp. 2410-2425, May 2019.

[52] M. R. Akdeniz, Y. Liu, M. K. Samimi MK, S. Sun, S. Rangan, T.S. Rappaport, and E. Erkip "Millimeter wave channel modeling and cellular capacity evaluation," *IEEE J. Sel. Areas in Commun.*, vol. 32, no. 6, pp. 1164-1179, Jun. 2014.

[53] Van Trees, Harry L. Optimum array processing: Part IV of detection, estimation, and modulation theory. John Wiley & Sons, 2002.

[54] D. Neumann, M. Joham, and W. Utschick, “Covariance matrix estimation in massive MIMO,” IEEE Signal Process. Lett., vol. 25, no. 6, pp. 863–867, Jun. 2018.

[55] A. O. Kalayci and G. M. Guvensen, “An efficient spatial channel covariance estimation via joint angle-delay power profile in hybrid massive MIMO systems,” in Proc. IEEE Int. Conf. Commun. Workshops (ICC Workshops), Jun. 2020, pp. 1–7.

APPENDIX A

CHANNEL ESTIMATION AND THE PILOTING SCHEME

Remember that channel estimation is done in the frequency domain. A pilot-based channel estimation procedure is considered. All the UEs transmit a pilot sequence of T_p symbols at frequency f for $f = 0, 1, \ldots, T-1$. UE k transmits the pilot sequence $\boldsymbol{\psi}_{kf} = [\psi_{kf}^{(1)}\ \psi_{kf}^{(2)}\ \ldots\ \psi_{kf}^{(T_p)}]^T \in \mathbb{C}^{T_p}$ in frequency bin f. Notice that there are different, more detailed methods for conducting pilot-based estimations [37] for CF networks. This thesis only considers a simple piloting convention to observe the effects of channel estimation since channel estimation is not the focus of this work. It is assumed that no pilot contamination occurs, i.e., every UE has a sequence that is orthogonal to each other. Due to this orthogonality, the relation $(\boldsymbol{\psi}_{kf})^H \boldsymbol{\psi}_{k'f} = E_T \delta_{kk'}$ for $\forall f, \forall k$ holds. Note that as mentioned in Chapter 4.2, E_T is the pilot sequence power. The received piloting signal at the n^{th} AP, at j^{th} piloting instance at frequency f is

$$\mathbf{r}_{fn}^{(j)} = \sum_{k=1}^{K} \sqrt{\alpha_{kn}} \mathbf{h}_{kn}^{f} \psi_{kf}^{(j)} + \mathbf{n}_n^f \in \mathbb{C}^{D \times 1} \tag{A.1}$$

for $j = 0, 1, \ldots, T_p$ and $f = 0, 1, \ldots, T-1$. Also, $\mathbf{n}_n^f$ is the ZMCSCG noise with the same properties as the noise vector in (4.2), just with a lower number of rows since this entity is defined for a single AP. The matrix $\mathbf{X}_f \in \mathbb{C}^{K \times T_p}$ is defined as

$$\mathbf{X}_f = [\sqrt{\alpha_{1n}}\boldsymbol{\psi}_{1f}\ \sqrt{\alpha_{2n}}\boldsymbol{\psi}_{2f} \ldots \sqrt{\alpha_{Kn}}\boldsymbol{\psi}_{Kf}]^T. \tag{A.2}$$

Note that due to the orthogonality of pilot sequences, the relation

$$\mathbf{X}_f \mathbf{X}_f^H = \mathrm{diag}\{\alpha_{1n}E_T, \alpha_{2n}E_T, \ldots, \alpha_{Kn}E_T\} \tag{A.3}$$

holds, and it is the same for every frequency bin. Also matrix $\mathbf{Y}_{fn} \in \mathbb{C}^{D \times T_p}$ is defined as $\mathbf{Y}_{fn} = [\mathbf{r}_{fn}^{(1)}\ \mathbf{r}_{fn}^{(2)} \ldots \mathbf{r}_{fn}^{(Tp)}]$. Then using the properties of the Kronecker product, we

can write

$$\text{vec}(\mathbf{Y}_{fn}) = (\mathbf{X}_f^T \otimes \mathbf{I}_D)\text{vec}(\mathbf{H}_{nf}) + \text{vec}(\mathbf{N}_f) \tag{A.4}$$

where $\mathbf{H}_{nf} = [\mathbf{h}_{1n}^f \ \mathbf{h}_{2n}^f \dots \mathbf{h}_{Kn}^f] \in \mathbb{C}^{D\times K}$ and $\mathbf{N}_f$ is the concatenated noise matrix derived in a similar fashion to $\mathbf{Y}_{fn}$. The entities in (A.4) are redefined for simplicity. They are redefined as; $\mathbf{r}_{fn}^\tau = \text{vec}(\mathbf{Y}_{fn}) \in \mathbb{C}^{DK\times 1}$, $\mathbf{u}_{fn} = \text{vec}(\mathbf{H}_{nf}) \in \mathbb{C}^{DK\times 1}$ and $\mathbf{F}_f = (\mathbf{X}_f^T \otimes \mathbf{I}_D) \in \mathbb{C}^{DT_p\times DK}$. Note that,

$$(\mathbf{F}_f)^H\mathbf{F}_f = \text{blkdiag}\{\alpha_{1n}E_T\mathbf{I}_D, \alpha_{2n}E_T\mathbf{I}_D, \dots, \alpha_{Kn}E_T\mathbf{I}_D\}. \tag{A.5}$$

Also $\mathbf{R}_{\mathbf{u}_{fn}} = \text{blkdiag}\{\mathbf{R}_{\mathbf{h}_{1n}}, \mathbf{R}_{\mathbf{h}_{2n}}, \dots, \mathbf{R}_{\mathbf{h}_{Kn}}\}$ due to independence of channels across different UEs. Note that $\mathbf{u}_{fn}$ contains the normalized channels of all UEs to AP n at frequency f, and it is the entity that is being estimated for all APs. The MMSE estimate of $\mathbf{u}_{fn}$ from the observation $\mathbf{r}_{fn}^\tau$ is $\hat{\mathbf{u}}_{fn}$ with estimation error $\tilde{\mathbf{u}}_{fn}$, which is written as (performing a standard MMSE estimation)

$$\mathbf{u}_{fn} = \hat{\mathbf{u}}_{fn} + \tilde{\mathbf{u}}_{fn} \tag{A.6}$$

$$\hat{\mathbf{u}}_{fn} = \mathbf{R}_{\mathbf{u}_{fn}\mathbf{r}_{fn}^\tau}\mathbf{R}_{\mathbf{r}_{fn}^\tau}^{-1}\mathbf{r}_{fn}^\tau. \tag{A.7}$$

Also, note that,

$$\mathbf{R}_{\mathbf{u}_{fn}\mathbf{r}_{fn}^\tau} = \mathbf{R}_{\mathbf{u}_{fn}}(\mathbf{F}_f)^H \tag{A.8}$$

$$\mathbf{R}_{\mathbf{r}_{fn}^\tau} = \mathbf{F}_f\mathbf{R}_{\mathbf{u}_{fn}}(\mathbf{F}_f)^H + N_0\mathbf{I}_{DT_p}. \tag{A.9}$$

Due to nature of MMSE operation, $\hat{\mathbf{u}}_{fn}$ and $\tilde{\mathbf{u}}_{fn}$ are uncorrelated (or orthogonal), which means $\mathbf{R}_{\mathbf{u}_{fn}} = \mathbf{R}_{\hat{\mathbf{u}}_{fn}} + \mathbf{R}_{\tilde{\mathbf{u}}_{fn}}$. From (A.6)-(A.9), the following equation can be written

$$\mathbf{R}_{\tilde{\mathbf{u}}_{fn}} = \mathbf{R}_{\mathbf{u}_{fn}} - \mathbf{R}_{\mathbf{u}_{fn}}(\mathbf{F}_f)^H[\mathbf{F}_f\mathbf{R}_{\mathbf{u}_{fn}}(\mathbf{F}_f)^H + N_0\mathbf{I}_{DT_p}]^{-1}\mathbf{F}_f\mathbf{R}_{\mathbf{u}_{fn}} \ \forall \ f \tag{A.10}$$

which is simplified by using Woodbury matrix identity into

$$\mathbf{R}_{\tilde{\mathbf{u}}_{fn}} = [\mathbf{R}_{\mathbf{u}_{fn}}^{-1} + (\mathbf{F}_f)^H\mathbf{F}_f\frac{1}{N_0}]^{-1}. \tag{A.11}$$

Note that, due to practical uncorrelated assumption of UE channels and lack of pilot contamination makes the matrices in (A.8),(A.9) and (A.11) block diagonal. Therefore the channel estimation for AP n to all UEs can be done separately for every UE in

this work. However, any future work featuring pilot contamination and/or correlated channels should continue from this form and derive the following results accordingly.

Using the block diagonal structure in (A.11), equations (4.8), (4.9) can be derived for every UE k and AP n by considering the corresponding block of the block diagonal matrices. The derivation of (4.7) follows a similar approach done in [49].

$$\begin{aligned}
\mathbf{R}_{\mathbf{h}_{kn}^f} &= \mathbb{E}\{\mathbf{h}_{kn}^f(\mathbf{h}_{kn}^f)^H\} \\
&= \mathbb{E}\left\{\sum_{l=0}^{L-1}\sqrt{\gamma_{kn}^l}\frac{1}{\sqrt{T}}\tilde{\mathbf{h}}_{kn}^l e^{-j\frac{2\pi}{T}fl}\sum_{l'=0}^{L-1}\sqrt{\gamma_{kn}^{l'}}\frac{1}{\sqrt{T}}(\tilde{\mathbf{h}}_{kn}^{l'})^H e^{j\frac{2\pi}{T}fl'}\right\} \\
&= \frac{1}{T}\sum_{l=0}^{L-1}\sum_{l'=0}^{L-1}\sqrt{\gamma_{kn}^l}\sqrt{\gamma_{kn}^{l'}}\mathbb{E}\{\tilde{\mathbf{h}}_{kn}^l\tilde{\mathbf{h}}_{kn}^{l'}\}e^{-j\frac{2\pi}{T}f(l'-l)} \\
&= \frac{1}{T}\sum_{l=0}^{L-1}\sum_{l'=0}^{L-1}\sqrt{\gamma_{kn}^l}\sqrt{\gamma_{kn}^{l'}}(\mathbf{A}_n)^H\mathfrak{R}_{kn}^l\mathbf{A}_n\delta_{ll'}e^{-j\frac{2\pi}{T}f(l'-l)} \\
&= \sum_{l=0}^{L-1}\gamma_{kn}^l(\mathbf{A}_n)^H\mathfrak{R}_{kn}^l\mathbf{A}_n. \qquad \text{(A.12)}
\end{aligned}$$

Finally, note that the relation in (A.12) is independent of frequency bin f. This independence can be derived in the same way for $\mathbf{R}_{\hat{\mathbf{h}}_{kn}}$ and $\mathbf{R}_{\mathbf{e}_{kn}}$.

APPENDIX B

DERIVATION OF CFI-D FILTER MATRICES

The cost function given in (4.21) must be minimized using the Lagrangian coefficients in (4.22). According to the Lagrangian multipliers rule, the following equations must be satisfied to find the optimal filters.

$$\frac{\partial J^{(i)}}{\partial [\mathbf{W}_f^{(i)}]^H} = \mathbf{0}_{ND\times K} \quad \text{for } f = 0, 1, \ldots, T-1. \tag{B.1}$$

$$\frac{\partial J^{(i)}}{\partial [\mathbf{C}_f^{(i)}]^H} = \mathbf{0}_{K\times K} \quad \text{for } f = 0, 1, \ldots, T-1. \tag{B.2}$$

$$\frac{\partial J^{(i)}}{\partial \Gamma_k^{(i)}} = 0 \quad \text{for } k = 1, 2, \ldots, K. \tag{B.3}$$

Note that (B.3) is just a different representation of the constraint given in (4.12). First, the MSE term needs to be expanded to solve these equations. Insert (4.10) into (4.13) using (4.2) to get

$$\begin{aligned}\mathrm{MSE}_i = \sum_{f=0}^{T-1} \mathbb{E}\Bigg\{ \Bigg[& \mathbf{y}_f^H \mathbf{W}_f^{(i)} [\mathbf{W}_f^{(i)}]^H \mathbf{y}_f - \mathbf{y}_f^H \mathbf{W}_f^{(i)} [\mathbf{C}_f^{(i)}]^H \bar{\mathbf{x}}_f^{(i-1)} - \\ & (\bar{\mathbf{x}}_f^{(i-1)})^H \mathbf{C}_f^{(i)} [\mathbf{W}_f^{(i)}]^H \mathbf{y}_f + (\bar{\mathbf{x}}_f^{(i-1)})^H \mathbf{C}_f^{(i)} [\mathbf{C}_f^{(i)}]^H \bar{\mathbf{x}}_f^{(i-1)} - \mathbf{y}_f^H \mathbf{W}_f^{(i)} \mathbf{x}_f + \\ & (\bar{\mathbf{x}}_f^{(i-1)})^H \mathbf{C}_f^{(i)} \mathbf{x}_f - \mathbf{x}_f^H [\mathbf{W}_f^{(i)}]^H \mathbf{y}_f + \mathbf{x}_f^H [\mathbf{C}_f^{(i)}]^H \bar{\mathbf{x}}_f^{(i-1)} + \mathbf{x}_f^H \mathbf{x}_f \Bigg] \Bigg\}. \end{aligned} \tag{B.4}$$

Before moving forward, it is helpful to define and derive some important CM entities to use in further calculations. Remember that the detector only knows the estimations of the channels ($\hat{\mathbf{H}}^f$), and the channel estimation errors ($\mathbf{E}^f$) are unknown with zero mean. Also, remember that these equations are written for every frequency bin separately, creating T parallel equations and solutions for each path. From (4.2) and (4.19), following relation can be written

$$\mathbf{R}_{\mathbf{y}_f \mathbf{x}_f} = \mathbb{E}\{(\hat{\mathbf{H}}^f \mathbf{x}_f + \mathbf{E}^f \mathbf{x}_f + \mathbf{n}_f)\mathbf{x}_f^H\} = \hat{\mathbf{H}}^f. \tag{B.5}$$

Similarly, from (4.2) and (4.14), we can write

$$\mathbf{R}_{\mathbf{y}_f\bar{\mathbf{x}}_f^{(i-1)}} = \mathbb{E}\{(\hat{\mathbf{H}}^f\mathbf{x}_f + \mathbf{E}^f\mathbf{x}_f + \mathbf{n}_f)(\bar{\mathbf{x}}_f^{(i-1)})^H\} = \hat{\mathbf{H}}^f\mathbf{P}_1^{(i)}. \tag{B.6}$$

Finally, from the definition of reliability matrices given in (4.14), remember that

$$\mathbf{R}_{\bar{\mathbf{x}}_f^{(i-1)}\mathbf{x}_f} = \mathbf{P}_1^{(i)}, \quad \mathbf{R}_{\bar{\mathbf{x}}_f^{(i-1)}} = \mathbf{P}_2^{(i)}. \tag{B.7}$$

Now, equations (B.1)-(B.3) can be solved for the filters. At (B.1), taking the partial derivative

$$\begin{aligned}
&\frac{\partial J^{(i)}}{\partial[\mathbf{W}_f^{(i)}]^H} = \mathbb{E}\{\mathbf{y}_f\mathbf{y}_f^H\mathbf{W}_f^{(i)} - \mathbf{y}_f(\bar{\mathbf{x}}_f^{(i-1)})^H\mathbf{C}_f^{(i)} - \mathbf{y}_f\mathbf{x}_f^H\} = \\
&\mathbf{R}_{\mathbf{y}_f}\mathbf{W}_f^{(i)} - \mathbf{R}_{\mathbf{y}_f\bar{\mathbf{x}}_f^{(i-1)}}\mathbf{C}_f^{(i)} - \mathbf{R}_{\mathbf{y}_f\mathbf{x}_f} = \mathbf{R}_{\mathbf{y}_f}\mathbf{W}_f^{(i)} - \hat{\mathbf{H}}^f\mathbf{P}_1^{(i)}\mathbf{C}_f^{(i)} - \hat{\mathbf{H}}^f = \mathbf{0}_{ND\times K}.
\end{aligned} \tag{B.8}$$

Now, the partial derivative at (B.2) can be taken as

$$\begin{aligned}
\frac{\partial J^{(i)}}{\partial[\mathbf{C}_f^{(i)}]^H} &= \mathbb{E}\{-\bar{\mathbf{x}}_f^{(i-1)}\mathbf{y}_f^H\mathbf{W}_f^{(i)} + \bar{\mathbf{x}}_f^{(i-1)}(\bar{\mathbf{x}}_f^{(i-1)})^H\mathbf{C}_f^{(i)} + \bar{\mathbf{x}}_f^{(i-1)}\mathbf{x}_f^H + \mathbf{\Gamma}^{(i)}\} \\
&= -\mathbf{R}_{\bar{\mathbf{x}}_f^{(i-1)}\mathbf{y}_f}\mathbf{W}_f^{(i)} + \mathbf{R}_{\bar{\mathbf{x}}_f^{(i-1)}}\mathbf{C}_f^{(i)} + \mathbf{R}_{\bar{\mathbf{x}}_f^{(i-1)}\mathbf{x}_f} + \mathbf{\Gamma}^{(i)}\} \\
&= -\mathbf{P}_1^{(i)}[\hat{\mathbf{H}}^f]^H\mathbf{W}_f^{(i)} + \mathbf{P}_2^{(i)}\mathbf{C}_f^{(i)} + \mathbf{P}_1^{(i)} + \mathbf{\Gamma}^{(i)} = \mathbf{0}_{K\times K}.
\end{aligned} \tag{B.9}$$

Rearrange (B.8) and (B.9) to get

$$\mathbf{R}_{\mathbf{y}_f}\mathbf{W}_f^{(i)} = \hat{\mathbf{H}}^f(\mathbf{I}_K + \mathbf{P}_1^{(i)}\mathbf{C}_f^{(i)}), \tag{B.10}$$

$$\mathbf{P}_2^{(i)}\mathbf{C}_f^{(i)} = \mathbf{P}_1^{(i)}[(\hat{\mathbf{H}}^f)^H\mathbf{W}_f^{(i)} - \mathbf{I}_K] - \mathbf{\Gamma}^{(i)} \tag{B.11}$$

for $f = 0, 1, \ldots, T-1$ both. Now define the auxiliary matrices $\mathbf{A}_f^{(i)}$ and $\mathbf{D}_f^{(i)}$ as

$$\mathbf{A}_f^{(i)} = [\mathbf{P}_2^{(i)} - (\mathbf{P}_1^{(i)})^H(\hat{\mathbf{H}}^f)^H\mathbf{R}_{\mathbf{y}_f}^{-1}\hat{\mathbf{H}}^f\mathbf{P}_1^{(i)}]^{-1}, \tag{B.12}$$

$$\mathbf{D}_f^{(i)} = (\mathbf{P}_1^{(i)})^H(\hat{\mathbf{H}}^f)^H\mathbf{R}_{\mathbf{y}_f}^{-1}\hat{\mathbf{H}}^f - (\mathbf{P}_1^{(i)})^H. \tag{B.13}$$

Inserting $\mathbf{W}_f^{(i)}$ from (B.10) into (B.11), using the constraint in (4.12) and using (B.12), (B.13) the equality for Lagrangian coefficients in (4.25) can be derived. Using (4.25), (B.10), (B.11), (B.12) and (B.13) the equations for the filters $\mathbf{W}_f^{(i)}$ and $\mathbf{C}_f^{(i)}$ given in (4.23) and (4.24) holds true.

APPENDIX C

CALCULATION OF SPECIAL BLOCK DIAGONAL MATRICES

All four parts of the matrix $\mathbf{R}_{\mathbf{y}_{kf}^{(i)}}$ given in (4.32) corresponds to a different part of the CM matrix of the received signal $\mathbf{y}_{kf}^{(i)}$. The $\hat{\mathbf{H}}_k^{f,\mathfrak{s}}(\hat{\mathbf{H}}_k^{f,\mathfrak{s}})^H$ term comes from instantaneous channel estimates of UEs in the set $\mathcal{S}_k$. Note that these channels are sparsified and used directly in the IB-DFE operation for UE k. The matrix $N_0\mathbf{I}_{DN}$ corresponds to the noise terms. The matrix $\mathbf{R}_{\mathfrak{s}'}^{k,(i)}$ corresponds to the residual interference that is left over from the PIC operation. It can be written as

$$\mathbf{R}_{\mathfrak{s}'}^{k,(i)} = \mathrm{blkdiag}\{\mathbf{R}_{\mathfrak{s}'}^{kn_1,(i)}, \mathbf{R}_{\mathfrak{s}'}^{kn_2,(i)}, \ldots, \mathbf{R}_{\mathfrak{s}'}^{kn_{\bar{\mathcal{N}}},(i)}\}, \tag{C.1}$$

$$\mathbf{R}_{\mathfrak{s}'}^{kn_q,(i)} = \sum_{k' \in \mathcal{S}'_k \cap \mathcal{K}_{n_q}} \alpha_{k'n_q}(1 + \beta_{k'}^{(i)} - 2\mathrm{Re}\{\rho_{k'}^{(i)}\})\mathbf{R}_{\hat{\mathbf{h}}_{k'n_q}} \tag{C.2}$$

for $q = 1, 2, \ldots, \bar{\mathcal{N}}$ and $n_q \in \mathcal{N}_k \ \forall q$ using (4.9) and (4.16). Note that this matrix is independent of the frequency bin f. This independence is due to not using the instantaneous channels for the residual interference calculation. This way, this matrix can be calculated once for all APs and used by just adding the necessary scaling coefficients for several transmission blocks. Since the matrices $\mathbf{R}_{\hat{\mathbf{h}}_{k'n_q}}$ are already known and $\mathbf{R}_{\mathfrak{s}'}^{k,(i)}$ has a block diagonal structure the CCP of the operation is reduced significantly.

While calculating $\mathbb{E}\{\mathbf{y}_{kf}^{(i)}(\mathbf{y}_{kf}^{(i)})^H\}$, the self multiplication terms present in (4.29) results in the $1+\beta_{k'}^{(i)}$ part in (C.2), and cross multiplication parts result in the $-2\mathrm{Re}\{\rho_{k'}^{(i)}\}$ part in (C.2). Since the channels are uncorrelated among different UEs and at different APs, this relation can be achieved in every block of the block diagonal matrix $\mathbf{R}_{\mathfrak{s}'}^{k,(i)}$ in (C.1).

Note that the channel estimation error is not present in $\mathbf{R}_{\mathfrak{s}'}^{k,(i)}$. The channel estimation error is accounted for in the matrix $\mathbf{R}_{\mathfrak{e}}^{k}$ for all UEs in the set $\mathcal{M}_k$. This matrix is not

calculated separately for the sets $\mathcal{S}_k$ and $\mathcal{S}'_k$. This is possible because the channel estimates are used in the PIC operation, meaning the non-estimated parts of the channels are untouched before the IB-DFE operation, and they can be accounted for together and once for all iterations. The matrix $\mathbf{R}_{\mathfrak{e}}^{k}$ can be derived as

$$\mathbf{R}_{\mathfrak{e}}^{k} = \text{blkdiag}\{\mathbf{R}_{\mathfrak{e}}^{kn_1}, \mathbf{R}_{\mathfrak{e}}^{kn_2}, \ldots, \mathbf{R}_{\mathfrak{e}}^{kn_{\bar{\mathcal{N}}}}\}, \tag{C.3}$$

$$\mathbf{R}_{\mathfrak{e}}^{kn_q} = \sum_{k' \in \mathcal{K}_{n_q}} \alpha_{k'n_q} \mathbf{R}_{\mathbf{e}_{k'n_q}} \tag{C.4}$$

for $q = 1, 2, \ldots, \bar{\mathcal{N}}$ and $n_q \in \mathcal{N}_k \ \forall q$ using (4.8) and (4.16). The matrix $\mathbf{R}_{\mathfrak{e}}^{k}$ is also block diagonal due to uncorrelated channels for different UEs and different APs. Note that only UEs in the sets $\mathcal{K}_{n_q}$ for different n_q indexes are included since the channels of the UEs outside those sets are not estimated, hence no estimation error.

To better understand the residual interference term from PIC, the relation in (C.2) can actually be derived from (4.29). Writing down the CM definition for $\mathbf{y}_{kf}^{(i)}$ as

$$\begin{aligned}
&\mathbb{E}\{\mathbf{y}_{kf}^{(i)}(\mathbf{y}_{kf}^{(i)})^H\} = \mathbb{E}\Big\{\Big(\mathbf{y}_{kf} - \hat{\mathbf{H}}_k^{f,\mathfrak{s}'}\bar{\mathbf{x}}_{f,s'}^{k,(i-1)}\Big)\Big((\mathbf{y}_{kf})^H - (\bar{\mathbf{x}}_{f,s'}^{k,(i-1)})^H(\hat{\mathbf{H}}_k^{f,\mathfrak{s}'})^H\Big)\Big\} = \\
&\mathbb{E}\Big\{\mathbf{y}_{kf}(\mathbf{y}_{kf})^H - \hat{\mathbf{H}}_k^{f,\mathfrak{s}'}\bar{\mathbf{x}}_{f,s'}^{k,(i-1)}(\mathbf{y}_{kf})^H - \mathbf{y}_{kf}(\bar{\mathbf{x}}_{f,s'}^{k,(i-1)})^H(\hat{\mathbf{H}}_k^{f,\mathfrak{s}'})^H + \\
&\hat{\mathbf{H}}_k^{f,\mathfrak{s}'}\bar{\mathbf{x}}_{f,s'}^{k,(i-1)}(\bar{\mathbf{x}}_{f,s'}^{k,(i-1)})^H(\hat{\mathbf{H}}_k^{f,\mathfrak{s}'})^H\Big\}.
\end{aligned} \tag{C.5}$$

The first term in (C.5) is $\mathbf{R}_{\mathbf{y}_{kf}}$. The last three terms are related to the residual interference. Notice the following

$$\mathbf{y}_{kf} = \mathbf{H}_k^f\mathbf{x}_f + \mathbf{n}_f^k = \hat{\mathbf{H}}_k^{f,\mathfrak{s}}\mathbf{x}_f^{k,\mathfrak{s}} + \hat{\mathbf{H}}_k^{f,\mathfrak{s}'}\mathbf{x}_f^{k,\mathfrak{s}'} + \mathbf{E}_k^f\mathbf{x}_f + \mathbf{n}_f^k \tag{C.6}$$

where $\mathbf{x}_f^{k,\mathfrak{s}}$ and $\mathbf{x}_f^{k,\mathfrak{s}'}$ are partitions of $\mathbf{x}_f$ containing entries belonging to UEs in the sets $\mathcal{S}_k$ and $\mathcal{S}'_k$ respectively. Use the relation above to deduct the relation

$$\mathbb{E}\{\mathbf{y}_{kf}(\bar{\mathbf{x}}_{f,s'}^{k,(i-1)})^H(\hat{\mathbf{H}}_k^{f,\mathfrak{s}'})^H\} = \hat{\mathbf{H}}_k^{f,\mathfrak{s}'}\mathbf{P}_{1,\mathfrak{s}'}^{k,(i)}(\hat{\mathbf{H}}_k^{f,\mathfrak{s}'})^H \tag{C.7}$$

where $\mathbf{P}_{1,\mathfrak{s}'}^{k,(i)}$ is a diagonal matrix whose diagonal entries contain the diagonal entries of $\mathbf{P}_1^{(i)}$ which corresponds to the UEs in the set $\mathcal{S}'_k$. Due to $\mathbf{P}_{1,\mathfrak{s}'}^{k,(i)}$ being block diagonal (C.7) becomes

$$\hat{\mathbf{H}}_k^{f,\mathfrak{s}'}\mathbf{P}_{1,\mathfrak{s}'}^{k,(i)}(\hat{\mathbf{H}}_k^{f,\mathfrak{s}'})^H = \sum_{k' \in \mathcal{S}'_k} \hat{\mathbf{H}}_k^{f,\mathfrak{s}'}(:,k')[\hat{\mathbf{H}}_k^{f,\mathfrak{s}'}(:,k')]^H\rho_{k'}^{(i)}. \tag{C.8}$$

Finally, note that the multiplication of vectors in (C.8) results in a block diagonal matrix when it is inside an expectation operation. This is due to different channels being uncorrelated. The parts in the multiplier $(1 + \beta_{k'}^{(i)} - 2\mathrm{Re}\{\rho_{k'}^{(i)}\})$ in (C.2) can be explained by the four term expression at the end of (C.5). The first term creates the 1 in the multiplier. The second and third terms are Hermitians of each other, and when added, they create the $-2\mathrm{Re}\{\rho_{k'}^{(i)}\}$ part of the multiplier. The fourth term creates the $\beta_{k'}^{(i)}$ part of the multiplier. The block diagonal nature present in (C.1) is due to (C.8) resulting in a diagonal matrix.

APPENDIX D

DERIVATION OF UCIS-D FILTER MATRICES

The derivation of the filters for UCIS-D is extremely similar to Appendix B. The cost function given in (4.35) must be minimized using the Lagrangian coefficient $\bar{\Gamma}_k^{(i)}$. Following equations must be satisfied.

$$\frac{\partial J^{(i)}}{\partial (\mathbf{w}_{kf}^{(i)})^H} = \mathbf{0}_{\mathcal{N}D} \quad \text{for } f = 0, 1, \ldots, T-1. \tag{D.1}$$

$$\frac{\partial J^{(i)}}{\partial (\mathbf{c}_{kf}^{(i)})^H} = \mathbf{0}_{\bar{\mathcal{S}}} \quad \text{for } f = 0, 1, \ldots, T-1. \tag{D.2}$$

$$\frac{\partial J^{(i)}}{\partial \bar{\Gamma}_k^{(i)}} = 0. \tag{D.3}$$

Note that (D.3) is just a different representation of the constraint given in (4.34). First, the MSE term needs to be expanded to solve these equations. Insert (4.31) into (4.33) using (4.27) and (4.29) to get

$$\begin{aligned}
\mathrm{MSE}_i = \sum_{f=0}^{T-1} \mathbb{E}\Bigg\{ \Bigg[& (\mathbf{y}_{kf}^{(i)})^H \mathbf{w}_{kf}^{(i)} [\mathbf{w}_{kf}^{(i)}]^H \mathbf{y}_{kf}^{(i)} - (\mathbf{y}_{kf}^{(i)})^H \mathbf{w}_{kf}^{(i)} [\mathbf{c}_{kf}^{(i)}]^H \bar{\mathbf{x}}_{f,\mathfrak{s}}^{k,(i-1)} - \\
& (\bar{\mathbf{x}}_{f,\mathfrak{s}}^{k,(i-1)})^H \mathbf{c}_{kf}^{(i)}] [\mathbf{w}_{kf}^{(i)}]^H \mathbf{y}_{kf}^{(i)} + (\bar{\mathbf{x}}_{f,\mathfrak{s}}^{k,(i-1)})^H \mathbf{c}_{kf}^{(i)} [\mathbf{c}_{kf}^{(i)}]^H \bar{\mathbf{x}}_{f,\mathfrak{s}}^{k,(i-1)} - (\mathbf{y}_{kf}^{(i)})^H \mathbf{w}_{kf}^{(i)} x_{kf} \\
& + (\bar{\mathbf{x}}_{f,\mathfrak{s}}^{k,(i-1)})^H \mathbf{c}_{kf}^{(i)} x_{kf} - x_{kf}^* [\mathbf{w}_{kf}^{(i)}]^H \mathbf{y}_{kf}^{(i)} + x_{kf}^* [\mathbf{c}_{kf}^{(i)}]^H \bar{\mathbf{x}}_{f,\mathfrak{s}}^{k,(i-1)} + x_{kf}^* x_{kf} \Bigg] \Bigg\}.
\end{aligned} \tag{D.4}$$

Using (C.6), one can see that $\mathbf{R}_{\mathbf{y}_{kf}^{(i)} x_{kf}} = \hat{\mathbf{H}}_k^{f,\mathfrak{s}}(:, k_{\mathcal{S}})$ where $k_{\mathcal{S}}$ is the index of UE k in the set $\mathcal{S}_k$. Similarly, from (4.14) and (C.6), we can infer the relation $\mathbf{R}_{\mathbf{y}_{kf}^{(i)} \bar{\mathbf{x}}_{f,\mathfrak{s}}^{k,(i-1)}} = \hat{\mathbf{H}}_k^{f,\mathfrak{s}} \mathbf{P}_{1,\mathfrak{s}}^{k,(i)}$. Finally, using the definition of reliability matrices given in (4.14), one can infer the relations $\mathbf{R}_{\bar{\mathbf{x}}_{f,\mathfrak{s}}^{k,(i-1)} x_{kf}} = \mathbf{P}_{1,\mathfrak{s}}^{k,(i)}(:, k_{\mathcal{S}})$ and $\mathbf{R}_{\bar{\mathbf{x}}_{f,\mathfrak{s}}^{k,(i-1)}} = \mathbf{P}_{2,\mathfrak{s}}^{k,(i)}$. Now, equations

(D.1)-(D.3) can be solved for the filters. At (D.1), taking the partial derivative

$$\frac{\partial J^{(i)}}{\partial [\mathbf{w}_{kf}^{(i)}]^H} = \mathbb{E}\{\mathbf{y}_{kf}^{(i)}(\mathbf{y}_{kf}^{(i)})^H \mathbf{w}_{kf}^{(i)} - \mathbf{y}_{kf}^{(i)}(\bar{\mathbf{x}}_{f,\mathfrak{s}}^{k,(i-1)})^H \mathbf{c}_{kf}^{(i)} - \mathbf{y}_{kf}^{(i)} x_{kf}^*\}$$
$$= \mathbf{R}_{\mathbf{y}_{kf}^{(i)}} \mathbf{w}_{kf}^{(i)} - \mathbf{R}_{\mathbf{y}_{kf}^{(i)} \bar{\mathbf{x}}_{f,\mathfrak{s}}^{k,(i-1)}} \mathbf{c}_{kf}^{(i)} - \mathbf{R}_{\mathbf{y}_{kf}^{(i)} x_{kf}}$$
$$= \mathbf{R}_{\mathbf{y}_{kf}^{(i)}} \mathbf{w}_{kf}^{(i)} - \hat{\mathbf{H}}_k^{f,\mathfrak{s}} \mathbf{P}_{1,\mathfrak{s}}^{k,(i)} \mathbf{c}_{kf}^{(i)} - \hat{\mathbf{H}}_k^{f,\mathfrak{s}}(:, k_{\mathcal{S}}) = \mathbf{0}_{\mathcal{N}D}. \tag{D.5}$$

Now, the partial derivative at (D.2) can be taken as

$$\frac{\partial J^{(i)}}{\partial [\mathbf{c}_{kf}^{(i)}]^H} = \mathbb{E}\{-\bar{\mathbf{x}}_{f,\mathfrak{s}}^{k,(i-1)}(\mathbf{y}_{kf}^{(i)})^H \mathbf{w}_{kf}^{(i)} + \bar{\mathbf{x}}_{f,\mathfrak{s}}^{k,(i-1)}(\bar{\mathbf{x}}_{f,\mathfrak{s}}^{k,(i-1)})^H \mathbf{c}_{kf}^{(i)} + \bar{\mathbf{x}}_{f,\mathfrak{s}}^{k,(i-1)} x_{kf}^* + \bar{\mathbf{\Gamma}}_k^{(i)}\}$$
$$= -\mathbf{R}_{\bar{\mathbf{x}}_{f,\mathfrak{s}}^{k,(i-1)} \mathbf{y}_{kf}^{(i)}} \mathbf{w}_{kf}^{(i)} + \mathbf{R}_{\bar{\mathbf{x}}_{f,\mathfrak{s}}^{k,(i-1)}} \mathbf{c}_{kf}^{(i)} + \mathbf{R}_{\bar{\mathbf{x}}_{f,\mathfrak{s}}^{k,(i-1)} x_{kf}} + \bar{\mathbf{\Gamma}}_k^{(i)}\}$$
$$= -\mathbf{P}_{1,\mathfrak{s}}^{k,(i)} [\hat{\mathbf{H}}_k^{f,\mathfrak{s}}]^H \mathbf{w}_{kf}^{(i)} + \mathbf{P}_{2,\mathfrak{s}}^{k,(i)} \mathbf{c}_{kf}^{(i)} + \mathbf{P}_{1,\mathfrak{s}}^{k,(i)}(:, k_{\mathcal{S}}) + \bar{\mathbf{\Gamma}}_k^{(i)} = \mathbf{0}_{\bar{\mathcal{S}}}. \tag{D.6}$$

Rearrange (D.5) and (D.6) to get

$$\mathbf{R}_{\mathbf{y}_{kf}^{(i)}} \mathbf{w}_{kf}^{(i)} = [\hat{\mathbf{H}}_k^{f,\mathfrak{s}} \mathbf{P}_{1,\mathfrak{s}}^{k,(i)} \mathbf{c}_{kf}^{(i)} + \hat{\mathbf{H}}_k^{f,\mathfrak{s}}(:, k_{\mathcal{S}})], \tag{D.7}$$

$$\mathbf{P}_{2,\mathfrak{s}}^{k,(i)} \mathbf{c}_{kf}^{(i)} = \mathbf{P}_{1,\mathfrak{s}}^{k,(i)} (\hat{\mathbf{H}}_k^{f,\mathfrak{s}})^H \mathbf{w}_{kf}^{(i)} - \mathbf{P}_{1,\mathfrak{s}}^{k,(i)}(:, k_{\mathcal{S}}) - \bar{\mathbf{\Gamma}}_k^{(i)} \tag{D.8}$$

for $f = 0, 1, \ldots, T-1$ both. Now define the auxiliary matrix $\mathbf{A}_f^{k,(i)}$ and auxiliary vector $\mathbf{d}_f^{k,(i)}$ as

$$\mathbf{A}_f^{k,(i)} = [\mathbf{P}_{2,\mathfrak{s}}^{k,(i)} - (\mathbf{P}_{1,\mathfrak{s}}^{k,(i)})^H (\hat{\mathbf{H}}_k^{f,\mathfrak{s}})^H \mathbf{R}_{\mathbf{y}_{kf}^{(i)}}^{-1} \hat{\mathbf{H}}_k^{f,\mathfrak{s}} \mathbf{P}_{1,\mathfrak{s}}^{k,(i)}]^{-1}, \tag{D.9}$$

$$\mathbf{d}_f^{k,(i)} = (\mathbf{P}_{1,\mathfrak{s}}^{k,(i)})^H (\hat{\mathbf{H}}_k^{f,\mathfrak{s}})^H \mathbf{R}_{\mathbf{y}_{kf}^{(i)}}^{-1} \hat{\mathbf{H}}_k^{f,\mathfrak{s}}(:, k_{\mathcal{S}}) - \mathbf{P}_{1,\mathfrak{s}}^{k,(i)}(:, k_{\mathcal{S}}). \tag{D.10}$$

Inserting $\mathbf{w}_{kf}^{(i)}$ from (D.7) into (D.8), using the constraint in (4.34) and using (D.9), (D.10); the equality for Lagrangian coefficient in (4.38) can be derived. Using (4.38), (D.7), (D.8), (D.9) and (D.10) the equations for the filters $\mathbf{w}_{kf}^{(i)}$ and $\mathbf{c}_{kf}^{(i)}$ given in (4.36) and (4.37) hold true.